

Real-time retinal blood flow imaging with Fourier Domain Optical Coherence Tomography

by

Jing Xu

M.A.Sc., Simon Fraser University, 2009
B.Eng., Yangzhou University, 2005

Dissertation Submitted in Partial Fulfillment of the
Requirements for the Degree of
Doctor of Philosophy

in the
School Engineering Science
Faculty of Applied Sciences

© Jing Xu 2014

SIMON FRASER UNIVERSITY

Fall 2014

All rights reserved.

However, in accordance with the *Copyright Act of Canada*, this work may be reproduced, without authorization, under the conditions for "Fair Dealing." Therefore, limited reproduction of this work for the purposes of private study, research, criticism, review and news reporting is likely to be in accordance with the law, particularly if cited appropriately.

Approval

Name: Jing Xu
Degree: Doctor of Philosophy
Title: *Real time retinal blood flow imaging with Fourier Domain Optical Coherence Tomography*
Examining Committee: Chair: Dr. Yifan Jian
Research Associate

Dr. Marinko V. Sarunic, P. Eng.
Senior Supervisor
Associate Professor

Dr. Glenn H. Chapman, P. Eng.
Supervisor
Professor

Dr. Mirza Faisal Beg, P. Eng.
Supervisor
Professor

Dr. Ash Parameswaran, P. Eng.
Internal Examiner
Professor

Dr. Sherif Sherif
External Examiner
Associate Professor
Electrical & Computer Engineering
University of Manitoba

Date Defended/Approved: December 1st, 2014

Partial Copyright Licence



The author, whose copyright is declared on the title page of this work, has granted to Simon Fraser University the non-exclusive, royalty-free right to include a digital copy of this thesis, project or extended essay[s] and associated supplemental files ("Work") (title[s] below) in Summit, the Institutional Research Repository at SFU. SFU may also make copies of the Work for purposes of a scholarly or research nature; for users of the SFU Library; or in response to a request from another library, or educational institution, on SFU's own behalf or for one of its users. Distribution may be in any form.

The author has further agreed that SFU may keep more than one copy of the Work for purposes of back-up and security; and that SFU may, without changing the content, translate, if technically possible, the Work to any medium or format for the purpose of preserving the Work and facilitating the exercise of SFU's rights under this licence.

It is understood that copying, publication, or public performance of the Work for commercial purposes shall not be allowed without the author's written permission.

While granting the above uses to SFU, the author retains copyright ownership and moral rights in the Work, and may deal with the copyright in the Work in any way consistent with the terms of this licence, including the right to change the Work for subsequent purposes, including editing and publishing the Work in whole or in part, and licensing the content to other parties as the author may desire.

The author represents and warrants that he/she has the right to grant the rights contained in this licence and that the Work does not, to the best of the author's knowledge, infringe upon anyone's copyright. The author has obtained written copyright permission, where required, for the use of any third-party copyrighted material contained in the Work. The author represents and warrants that the Work is his/her own original work and that he/she has not previously assigned or relinquished the rights conferred in this licence.

Simon Fraser University Library
Burnaby, British Columbia, Canada

revised Fall 2013

Ethics Statement



The author, whose name appears on the title page of this work, has obtained, for the research described in this work, either:

- a. human research ethics approval from the Simon Fraser University Office of Research Ethics,

or

- b. advance approval of the animal care protocol from the University Animal Care Committee of Simon Fraser University;

or has conducted the research

- c. as a co-investigator, collaborator or research assistant in a research project approved in advance,

or

- d. as a member of a course approved in advance for minimal risk human research, by the Office of Research Ethics.

A copy of the approval letter has been filed at the Theses Office of the University Library at the time of submission of this thesis or project.

The original application for approval and letter of approval are filed with the relevant offices. Inquiries may be directed to those authorities.

Simon Fraser University Library
Burnaby, British Columbia, Canada

update Spring 2010

Abstract

Optical Coherence Tomography (OCT) is a non-invasive micrometer-resolution depth resolved medical imaging tool for diagnostic visualization of the retinal structures *in vivo*. In this thesis, we first describe the capability of OCT for providing structural information by quantitative retinal thickness measurements in animal models of diseases causing vision loss.

In the rest of the work described in this thesis, we focus on the development of an extension of OCT called speckle variance (sv) OCT, which provides functional information such as detecting capillaries within in the retina. Retinal capillary networks are critically linked to retinal neuronal health and disease. The ability to perform accurate *in vivo* examination of human retinal capillary networks is therefore valuable for studying mechanisms that govern retinal homeostasis and retinal vascular diseases. A real-time implementation of the svOCT provided by the GPU acceleration was described to provide visualization of *en-face* vasculature networks during acquisition.

A qualitative comparison study was described in this thesis by comparing the retinal vasculature images acquired from svOCT and Florescence Angiography (FA) for both healthy and diseased patients. The capability of svOCT with respect to quantifying capillary network information has been also validated in this thesis. The results of these studies suggest that this GPU accelerated svOCT has the potential to non-invasively provide useful quantitative information about human retinal capillary networks, and may have clinical and research applications for the management of retinal microvascular diseases, a major cause of vision loss worldwide.

To further adapt the svOCT to be more clinical friendly, preliminary work on enhancing the real-time visualization of vascular information from distinct retinal capillary beds during acquisition was proposed and implemented in this thesis.

Keywords: Flow contrast imaging, Optical Coherence Tomography, Speckle Variance, Graphics Processing Unit, Capillary networks, segmentation

Dedicated to my family

Acknowledgements

It has been an exciting journey for me to complete this thesis. I have so many people to acknowledge, and I would not have been able to finish this without their support!

First, I would like to express my gratitude to my advisor, Dr. Marinko Sarunic. He was always supportive of my research work and contributed many insightful ideas for my thesis work. It was an honor being able to work with him. I have known him when I started my Master program back in 2007. Since then, he has always been a mentor, a supervisor, a teacher, and also a friend to me. I give infinite thanks to his support, patience, and encouragement throughout all these years!

Second, I would like to thank Dr. Faisal Beg and Dr. Glenn Chapman for being in my supervisory committee and their guidance, insightful comments, and technical expertise. Their help and knowledge in image processing and optics respectively was invaluable.

Third, I would like to thank all my examining committee for their time reading my thesis, attending my defence, and providing valuable feedbacks.

Next, I would like to thank all my friends at Simon Fraser University, especially from the Biomedical Optics Research Group (BORG).

Finally, special thanks to my family for their unconditional love and continued support. No matter what I do, I know you will always be proud.

Table of Contents

Approval.....	ii
Partial Copyright Licence	iii
Ethics Statement.....	iv
Abstract.....	v
Dedication.....	vi
Acknowledgements.....	vii
Table of Contents.....	viii
List of Tables.....	x
List of Figures.....	xi
List of Acronyms.....	xvi
Chapter 1. Introduction	1
1.1. The retina and retinal diseases.....	3
1.1.1. Retina.....	4
1.1.2. Blood supply to the retina	5
1.1.3. AMD and DR	8
1.2. Optical Imaging modalities used for AMD and DR	8
1.2.1. OCT.....	9
1.2.2. Fluorescein Angiography	9
1.3. Outline of thesis.....	10
1.4. Contributions	10
Chapter 2. Background	12
2.1. OCT.....	12
2.2. Processing steps for FD OCT.....	16
2.3. Quantitative analysis in animal models with FDOCT.....	18
2.4. Function extensions for flow detection	21
2.4.1. Doppler OCT	21
2.4.2. OMAG	22
2.4.3. pvOCT and svOCT	23
2.4.4. SSADA	23
2.5. Summary.....	24
Chapter 3. Graphics processing unit accelerated speckle variance OCT processing and display in real time	25
3.1. Acquisition and Processing components	25
3.1.1. Processing.....	27
3.2. Mouse svOCT Imaging.....	33
3.3. Additional processing for human clinical imaging.....	35
3.4. Conclusion.....	40

Chapter 4. Comparison of svOCT and Fluorescence Angiography	41
4.1. Introduction.....	41
4.2. Methods	42
4.3. Results	44
4.4. Discussion and conclusion	50
Chapter 5. Quantitative in vivo study of human retinal capillary networks using svOCT	52
5.1. Experiment #1	53
5.1.1. Materials and Methods	53
Human Donor Eye.....	53
In vivo svOCT imaging of Human Subjects	53
Segmentation of Capillary Networks.....	54
5.1.2. Results	55
Capillary Network Topography in svOCT and Confocal Images	55
Quantitative Analysis.....	58
5.2. Experiment #2:	60
5.2.1. Materials and Methods	60
Confocal images from human donor eyes	60
svOCT images from live subjects	60
5.2.2. Results	61
5.3. Discussion	62
Chapter 6. GPU implementation with Segmentation in real time	64
6.1. Introduction.....	64
6.2. Methods	65
6.3. Results	68
6.4. Summary.....	74
Chapter 7. Discussion/Future Works.....	76
7.1. Conclusion.....	76
7.2. Future work	77
7.2.1. Double buffered system.....	77
7.2.2. Customized GC segmentation utilizing multiple GPUs.....	78
7.2.3. Quantitative analysis of svOCT and Fluorescence Angiography	79
References	81

List of Tables

Table 5.1.	Demographic Details: Age, Sex, Eye, Date of Imaging of Patients for svOCT imaging.	54
------------	--	----

List of Figures

Figure 1.1.	Simulation of vision loss from AMD (A), Glaucoma (B), and DR (C).....	2
Figure 1.2.	(A) Schematic of the human eye. (B) Retina as seen through an ophthalmoscope. Image from webvision [6]. Modified from National Eye Institute, National Institutes of Health Ref#: NEA09.....	3
Figure 1.3.	Schematic drawing of the layers of the retina (reproduced based on webvision [6].	5
Figure 1.4.	Fundus photograph showing fluorescein imaging of the major arteries and veins in a normal human right eye retina.	6
Figure 1.5.	Confocal image from the macula region of a 66-year-old donor. The area imaged measured 3180 by 3180 μm . This image was pseudocolored to show the microvasculature at the different depth. Dashed concentric circles: foveola, fovea, and parafovea. Figure obtained from[9].	7
Figure 2.1.	Basic schematic of different types of OCT system. (A) Time Domain OCT. (B) Swept Source OCT. (C) Spectral Domain OCT.....	13
Figure 2.2.	Graphical illustration of the technical terms used in OCT.	15
Figure 2.3.	Target retinal layers of a representative cross-sectional OCT image centered at the macula.	16
Figure 2.4.	Processing pipeline for SDOCT (green) and SSOCT (blue).	17
Figure 2.5.	Histopathological validation of the EVC model. A: Measurements of intraocular pressure (IOP). B: Quantification of Fluoro-Gold labelled RGCs. C: Representative pictures of Fluoro-Gold labelled RGCs. D: Hemotoxylin-eosin staining of sections. E: Representative sections of in vivo FDOCT B-scan images. F: Quantification of the thickness of intact and glaucomatous retinas from FDOCT measurements. (Image from[15])	20
Figure 3.1.	Diagram of speckle variance OCT data acquired and processing from (A) a human eye. Speckle variance is calculated with (B) multiple B-scans acquired from the same location of the eye and generate (C) one svOCT B-scan. (D) The intensity and svOCT B-scans are compared to show enhanced flow signals.....	27
Figure 3.2.	CUDA processing pipeline captured using the NVIDIA Visual Profiler.	29
Figure 3.3.	Comparison of (A) an intensity B-scan and (B) a svOCT B-scan. Comparison of (C) the intensity <i>en-face</i> view and (D) svOCT <i>en-face</i> projection.....	29

Figure 3.4.	A representative volume view (A) with three user-selected depth layers indicated. The corresponding <i>en-face</i> views of each selected region in red (B), green (C), blue (D). A super-imposed image of all three regions into a single colour-mapped image (E).	31
Figure 3.5.	The images in A), D) and G) illustrate representative B-scans at the equivalent position of the red lines in the <i>en-face</i> images B), E) and H), respectively. The combined colour-coded svOCT <i>en-face</i> images corresponding to A), D) and G) are presented in C), F) and I), respectively. Imaging areas from the 1st, 2nd, and 3rd rows are: 1.5x1.5 mm ² , 2x2 mm ² , and 1x1 mm ² , respectively.....	32
Figure 3.6.	The svOCT B-scan images in (A, D, G) illustrate the selected depths of interest for an area of 1x1 mm ² ; the intensity <i>en-face</i> images are presented in (B, E, H); and the svOCT images are presented in (C, F, I). The B-scan (J) presents a colour-coded combination of (A, D, G), where each colour represents: NFL/GCL—blue, IPL—green, and OPL—red. The combined intensity <i>en-face</i> image of all depth regions of interest is presented in (K), and the superimposed colour-coded svOCT <i>en-face</i> image is presented in (L).	34
Figure 3.7.	Functions implemented to minimize motion artifacts and improve image quality. (A) Intensity <i>en face</i> image; (B) svOCT <i>en face</i> image; (C) svOCT <i>en face</i> after motion registration and (D) svOCT <i>en face</i> after notch filter.....	36
Figure 3.8.	The intensity <i>en-face</i> views of different depth region inside the ONH (A-D) and the corresponding svOCT <i>en-face</i> views (E-H), respectively.	37
Figure 3.9.	A representative B-scan acquired at ONH (A) with three user-selected depth layers indicated. The intensity <i>en-face</i> view generated by the entire selected depth layers (B). The super-imposed svOCT <i>en-face</i> view of all three regions (C).....	38
Figure 3.10.	Representative colour-mapped sv <i>en-face</i> at foveal region with the field of view of (A) 2x2 mm ² , and (B) 1x1 mm ² . Flow contrast <i>en-face</i> projection at the optic nerve head acquired from a healthy volunteer (C), and a glaucoma patient (D).....	38
Figure 3.11.	A representative <i>en-face</i> view (A) and a B-scan (B) acquired at the front of the eye (A). The intensity <i>en-face</i> view (C) and the svOCT <i>en-face</i> view (D).....	39
Figure 4.1.	Human macula vasculature. Comparison between fluorescein angiography (A) and speckle variance OCT (B) images captured from a healthy subject demonstrates an observable increase in the density of capillary detail in the svOCT image (scale bar = 200 μm). The FA image was acquired with 40° field of view and cropped to correspond to the region acquired with the svOCT	45

Figure 4.2.	Isolation of distinct human capillary networks with speckle variance OCT. (A) Representative B-scan image of the human retina (A) demonstrates various inner retinal layers including NFL, GCL, IPL, INL, OPL and ONL. Semi-automated segmentation of B-scan images (red, green and blue lines) allows generation of <i>en-face</i> OCT images of different capillary networks within, and between, these retinal layers. The morphology of capillary networks within the NFL (B) and networks located between GCL and INL (C) and INL and ONL (D) bear close morphological correlations to previous histologic studies of these networks. Superimposing <i>en-face</i> images (E) also allows study of spatial relationships between various networks (scale bar = 200 μ m).....	46
Figure 4.3.	Application of speckle variance OCT to investigate diabetic retinopathy. Fluorescein angiography (A) of a diabetic patient demonstrates proliferative disease with marked retinal non-perfusion. <i>En-face</i> images of the optic disk (Inset I) acquired with svOCT clearly illustrates neovascularization of the optic disk (arrows). Speckle variance OCT images of the peri-macular (Inset II) and macular (Inset III) eccentricities also demonstrate marked capillary dropout (arrows) within these regions. (scale bar = 500 μ m).	47
Figure 4.4.	Comparison of FA (A-D) and corresponding svOCT (E-F) acquired from DR patients. (scale bar: 200 μ m).....	49
Figure 4.5.	(A) Representative segmented Bscan; Comparison of FA (B) and svOCT (C) acquired from AMD patient. (scale bar: 400 μ m).....	50
Figure 5.1.	Regions of the retina in the capillary study. Transverse retinal section (A) and B-scan image (B) from healthy subjects demonstrate the histological and svOCT features respectively, at the studied region 3mm superior to the optic disc. Layers are colour coded: Layer 1 (orange) = Nerve Fibre Layer (NFL), Layer 2 (red) = Retinal Ganglion Cell layer (RGC), Layer 3 (yellow) = border of Inner Plexiform Layer and superficial Inner Nuclear Layer (IPL/sINL), Layer 4 (green) = border of deep Inner Nuclear Layer and Outer Plexiform Layer (dINL/OPL). ONL, outer nuclear layer; IS, inner-segment of photoreceptors; OS outer-segment of photoreceptors; RPE, retinal pigment epithelium. Scale bar = 50 μ m.....	55
Figure 5.2.	Comparison of the capillary network in histology and svOCT eyes at 3mm superior to the optic disc. (A) to (D) = Whole-mount histological confocal images of the normal human retinal vasculature in histology control eyes. (E) to (H) = svOCT images of the capillary networks in living patients. (A) and (E) represent the NFL, (B) and (F) the RGC layer, (C) and (G) the IPL/sINL layer, and (D) and (H) the dINL/OPL layer. Scale bar = 100 μ m.....	57

Figure 5.3.	Quantification of capillary diameter and density in histology and svOCT eyes. (A) Captured histological retinal layer (dINL/OPL) with confocal microscopy in an unaltered state. (B) The svOCT image shown has been captured with the svOCT machine. A region of $636.5\mu\text{m}^2$ area is marked out and inverted to allow the same area quantified as the histology control images. Scale bar = $200\mu\text{m}$	59
Figure 5.4.	Graphs showing individual retinal layers against three different density indices – (A) the number of vessel intersections, (B) the number of vessels per $100\mu\text{m}$, and (C) the intercapillary distance. Comparison between the individual layers in the histological control eyes versus the svOCT eyes, revealed only the RGC layer was similar in all density indices ($P > 0.050$). All other comparisons differed significantly ($P < 0.050$), and are indicated by the asterisk (*). (Figure generated by collaborators)	59
Figure 5.5.	A representative FA image a healthy volunteer showing the six corresponding study regions acquired using svOCT.	61
Figure 5.6.	svOCT and histology images for each location.....	62
Figure 6.1.	An example of B-scans of a healthy retina (A) and diseased retina (B) with two red lines to select retinal layers of interest.	65
Figure 6.2.	Flow chart for the GPU based GC of a representative B-scan of a healthy retina (A), and then after Bilateral Filtering (B), Graph Cut segmentation (C), erosion and dilation (D), Connected Component Labeling (E) and layer boundary detection (F). ILM (red) / BM (green).....	66
Figure 6.3.	CUDA processing pipeline captured using the NVIDIA Visual Profiler	68
Figure 6.4.	Representative B-scans with different region selection by straight lines (a-c) and GC segmented ILM (red) and BM (green) (d), and the corresponding <i>en-face</i> images (A-D). The arrows indicate the motion artifacts that decrease the image quality.....	70
Figure 6.5.	Representative B-scans and <i>en-face</i> images of a DR patient before and after GC segmentation.	71
Figure 6.6.	<i>En-face</i> images generated from different selected region by the naïve approach (A-D) and GC segmentation (E-H).	71
Figure 6.7.	Segmentation results on retinas with pathological changes.....	72
Figure 6.8.	Representative B-scans A (healthy) and B (diseased) taken from locations indicated by the black vertical lines in the thickness maps C and D, respectively. The overall retinal thickness is thinning in D compared with C due to the retinal degeneration. The circled area indicates the retinal layer thickness thickening possibly due to the newly deposits and vessels growth. Field of view ($2 \times 2 \text{ mm}^2$).....	73

Figure 6.9. Comparisons of (A-C) B-scans, (D-F) svOCT *en-face* images, and (G-I) thickness maps among three different subjects. Field of view (2X2 mm²) 74

Figure 7.1. A timeline of GC solver from NPP. 79

List of Acronyms

AMD	Age-related Macular Degeneration
BM	Bruch's membrane
CH	Choroid
CRA	Central Retinal Artery
CUDA	Compute Unified Device Architecture
DR	Diabetic Retinopathy
FA	Fluorescein Angiography
FD	Fourier Domain
FDOCT	Fourier Domain Optical Coherence Tomography
FFT	Fast Fourier transform
GCL	Ganglion Cell Layer
GPU	Graphics Processing Unit
ILM	internal limiting membrane
INL	Inner Nuclear Layer
IOP	Intraocular pressure
IPL	Inner Plexiform Layer
IS	Inner Segment
LCI	Low Coherence Interferometry
NA	Numerical Aperture
NFL	Nerve Fiber Layer
OCT	Optical Coherence Tomography
OMAG	Optical Microangiography
ONL	Outer Nuclear Layer
OPL	Outer Plexiform Layer
OS	Outer Segment
pvOCT	phase variance OCT
RNFL	Retinal Nerve Fiber Layer
RPCs	Radial Peripapillary Capillaries
RPE	Retinal Pigment Epithelium
SD	Spectral Domain
SNR	Signal to Noise Ratio

SS Swept Source
SSADA Split-spectrum amplitude-decorrelation angiography
svOCT speckle variance Optical Coherence Tomography

Chapter 1.

Introduction

Dictionaries define vision as “the act or power of sensing with the eyes” [1]. For many, it is considered the most important of the five senses for humans and loss of vision can be extremely costly. Close your eyes, and imagine. This blackness that you see is what the world looks like to the people who have lost their vision. Now, slightly open your eyes. That glance of light is so beautiful and precious, and it is this light that motivates vision scientists and researchers to dedicate their life to find better ways of preventing and treating vision loss. As biomedical engineers, our job is to develop imaging tools that assist the vision researchers and doctors in their fight against blindness.

Currently, the Canadian Institute for the Blind (CNIB) estimates that over one million Canadians are living with significant vision loss or blindness [2]. According to a CNIB online report, one in 11 Canadians aged 65 or older are living with vision loss. That is ~10% chance that somebody’s parent is going to lose the ability to see his or her grandchildren. In terms of the total costs for vision loss, CNIB reported in 2009 that blindness and vision loss costs \$15.8 billion dollars per year, of which the direct health care costs (including surgical procedures, medicines, lenses) costs \$8.6 billion dollars. The reality, unfortunately, is that the cost will likely keep growing. Technologies that can reduce the duration and improve the success of treatments against vision loss will have a significant effect on the costs to the Canadian economy.

Retinal diseases are one of the leading causes to affect the light sensitive tissue at the back of the eye, affecting the ability to detect light. Two of the dominant retinal diseases that cause blindness are macular degeneration and diabetic retinopathy. Simulated examples of the impacts on vision from these diseases are shown in Figure

1.1. Age-related Macular Degeneration (AMD) causes vision loss in the central vision, but peripheral vision often remains, allowing patients to be able to see just enough to move about. However, reading and writing can become difficult. Patients with glaucoma, on the other hand, may experience loss of peripheral vision, called tunnel vision, as depicted in Figure 1.1B. Diabetic Retinopathy (DR) causes a partial blurring or patchy loss of vision as shown in Figure 1.1C. Patients with this disease also have difficulty with reading.

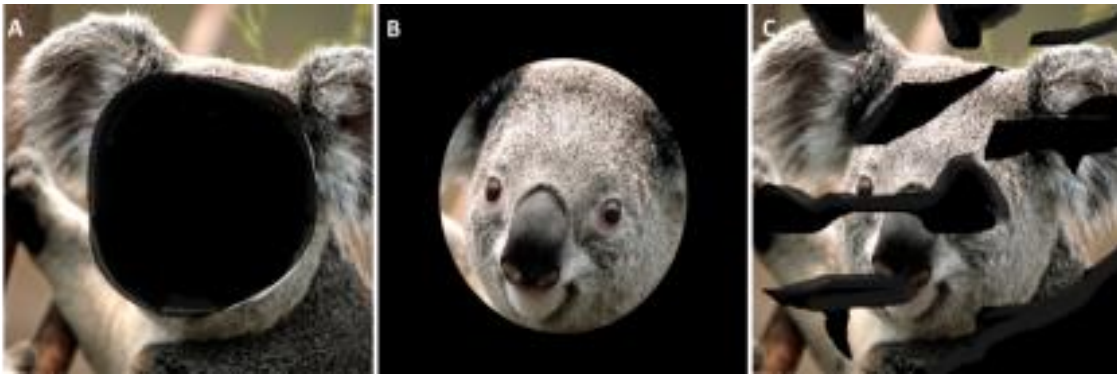


Figure 1.1. Simulation of vision loss from AMD (A), Glaucoma (B), and DR (C).

Over the past decade, the development of visible and near-infrared retinal imaging technology has grown rapidly. One of the dominant imaging modalities is Fourier Domain Optical Coherence Tomography (FDOCT), which has revolutionized clinical diagnostic ophthalmic imaging. FDOCT provides a detailed volumetric view of the retina for clinicians to identify the structural hallmarks of diseases such as AMD and DR. The FDOCT images are used to assess the need for treatments (surgical, intravitreal injection, laser, etc.) and afterwards to evaluate the results and monitor changes. A detailed introduction of this modality is described in Chapter 2.

In the remainder of this chapter, an overview of the eye anatomy, with a focus on the retina, is presented. This is followed by a more detailed description of AMD and DR. The imaging technologies that are specifically used by clinicians are described. The chapter concludes with an overview of the rest of this thesis, and my contributions towards novel technology for clinical imaging of AMD and DR.

1.1. The retina and retinal diseases

The eye is a complex organ. It is a roughly spherical in shape and filled with a water-like fluid, consisting of anterior and posterior segments that contain the focusing and detecting elements, respectively. It can be described to act like a camera, which is able to refract light (lens) and produce a focused image on the retina (detector) that can stimulate neural responses and enable the ability to see (picture).

Figure 1.2A presents a simple schematic of a human eye. A collimated beam incident on the eye is focused by the cornea and lens onto retina into a sharp point. The eye is roughly 25mm in diameter, and the retina located at the back of the eye contains cell layers that detect light, perform some processing on the information, and transmit electrical signals to the brain via the neurons of the optic nerve. When the ophthalmologist looks into the eye using an ophthalmoscope, the view of the retina that is seen is shown as Figure 1.2B. The large circular to oval white area in the center of the retina is the optic nerve, and the diameter is around ~2 mm. From the center of the optic nerve radiates the major blood vessels of the retina. The fovea is located in the center of the macula region of the retina, and it is responsible for sharp central vision. A circular field of approximately 6 mm around the fovea is considered the central retina while beyond this is peripheral retina stretching the ora serrata, 21 mm from the center of the optic disc [3–5].

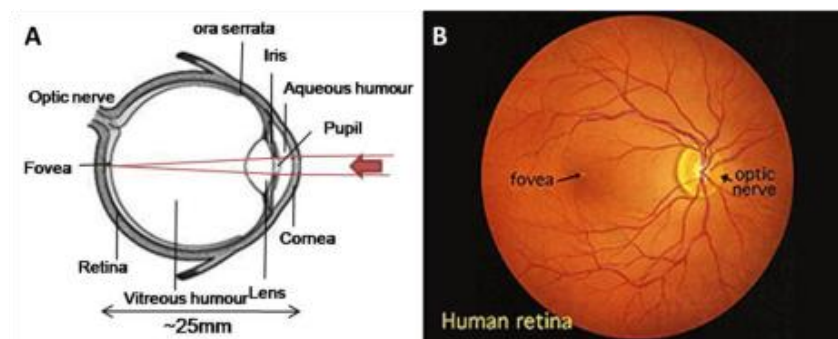


Figure 1.2. (A) Schematic of the human eye. (B) Retina as seen through an ophthalmoscope. Image from webvision [6]. Modified from National Eye Institute, National Institutes of Health Ref#: NEA09.

1.1.1. Retina

The retina is a layer of tissue at the back of the eye that senses light and turns it into neural impulses that are transmitted to the brain. The retina is approximately 0.5 mm thick and lines the back of the eye. A diagram of a portion of human retina is shown in Figure 1.3. The retina is made up of several layers of cells and the light passes through all of them for transduction, which is the conversion of a stimulus from one form (light) to another (electrochemical).

First of all, light needs to travel through multiple retinal layers in order to strike and activate the photoreceptors, which are the rods and cones. Cones are responsible for colour vision and detailed vision, and work well with bright light. They are mainly distributed in the centre of the macula (fovea centralis), and the number of cones decreases dramatically from the centre towards the periphery of the retina. On the other hand, the rods are concentrated outside the fovea, and are responsible for the peripheral vision. Rods are very sensitive and can be activated at low light levels; however, they are not capable of colour vision. The average human retina contains ~92 million rods, which outnumber cones by about ~20 to 1 [7].

After the light hits the rods and cones, they send the information to the second layer of cells which are called bipolar cells. Other types of cells in the retina such as horizontal cells have their own contributions of processing the visual information. Then the bipolar cells transmit the signal information to the next layer of cells which are called the ganglion cells. The ganglion cells are the output cells of the retina, where the axons of these cells make up the optic nerve that transmits the visual information to the brain.

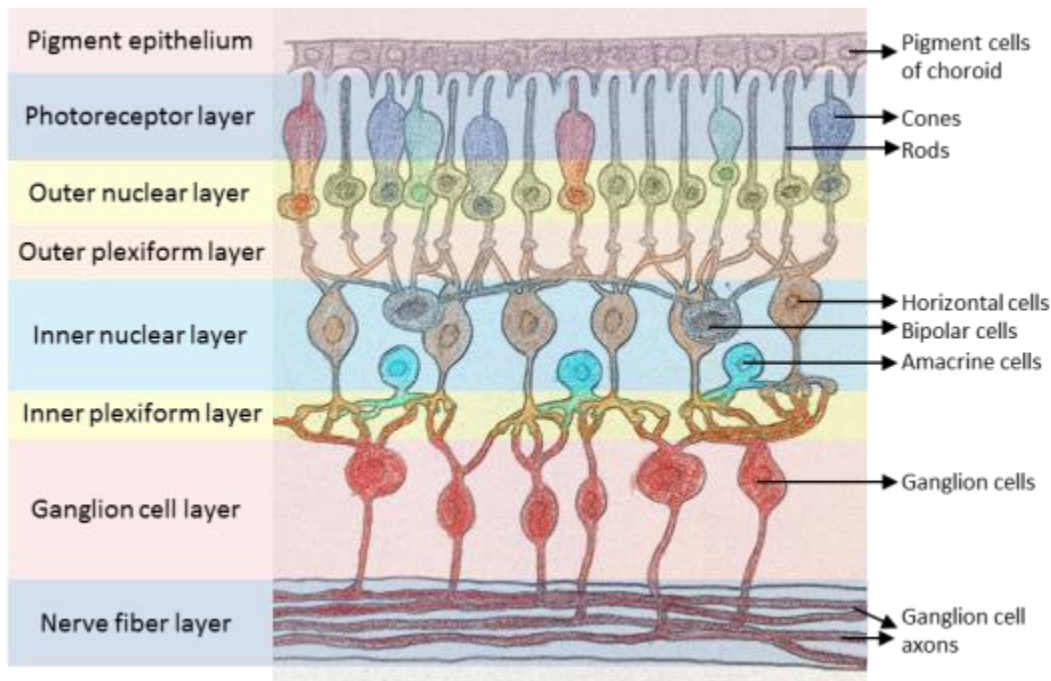


Figure 1.3. Schematic drawing of the layers of the retina (reproduced based on webvision [6].

1.1.2. Blood supply to the retina

There are two sources of blood supply to the human retina: the central retinal artery (CRA) and the choroidal blood vessels. The inner retina is bounded by the nerve fibre layer (NFL) anteriorly and the inner nuclear layer (INL) posteriorly, and it gets nourished by the blood flows that travels through CRA from the optic nerve head (ONH). The choroidal blood vessels feed the outer retina, particularly the photoreceptors. Understanding the retinal blood supply is especially important for diabetic retinopathy.

The CRA follows the patterns as shown in Figure 1.4, that the vessels come out from the ONH and run in a radial fashion curving towards and around the fovea. These vessels supply three layers of capillary networks which are the radial peripapillary capillaries (RPCs), the inner and outer layer of capillaries. The RPCs are the most superficial layer of capillaries lying in the inner part of NFL, and its functionality is to feed the superficial nerve fibres surrounding the ONH. The inner capillaries lie in the GCLs under and parallel to the RPCs. The outer capillary network runs from the inner plexiform layer (IPL) to the outer plexiform layer (OPL) through the inner nuclear layer (INL) [8].

Figure 1.5 shows a confocal projection from the macula region made by Yu et al [9]. This image covered the foveola (central capillary-free zone), fovea, and parafoveal regions, indicated by three concentric circles superimposed on the vascular network, with diameters 350, 1850, 2850 μm , respectively. The macular vessels arise from branches of the superior temporal and inferior temporal arteries, and the capillaries become two layered and finally join as a single layered ring to form an avascular zone.

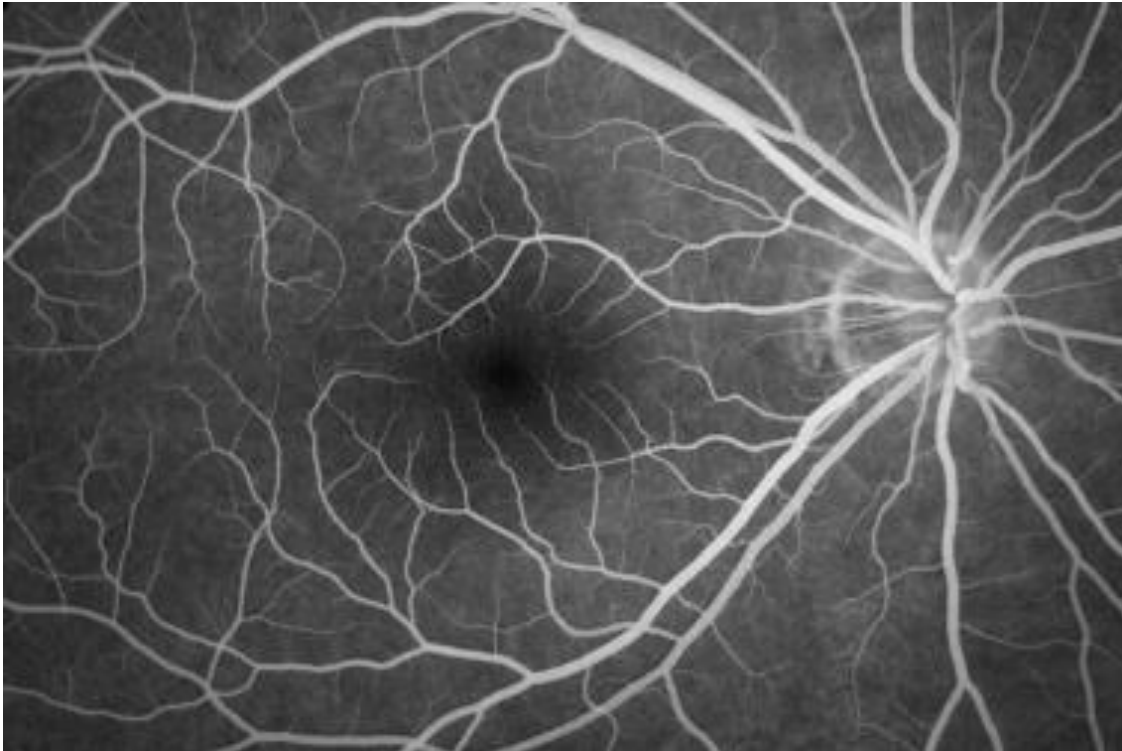


Figure 1.4. Fundus photograph showing fluorescein imaging of the major arteries and veins in a normal human right eye retina.

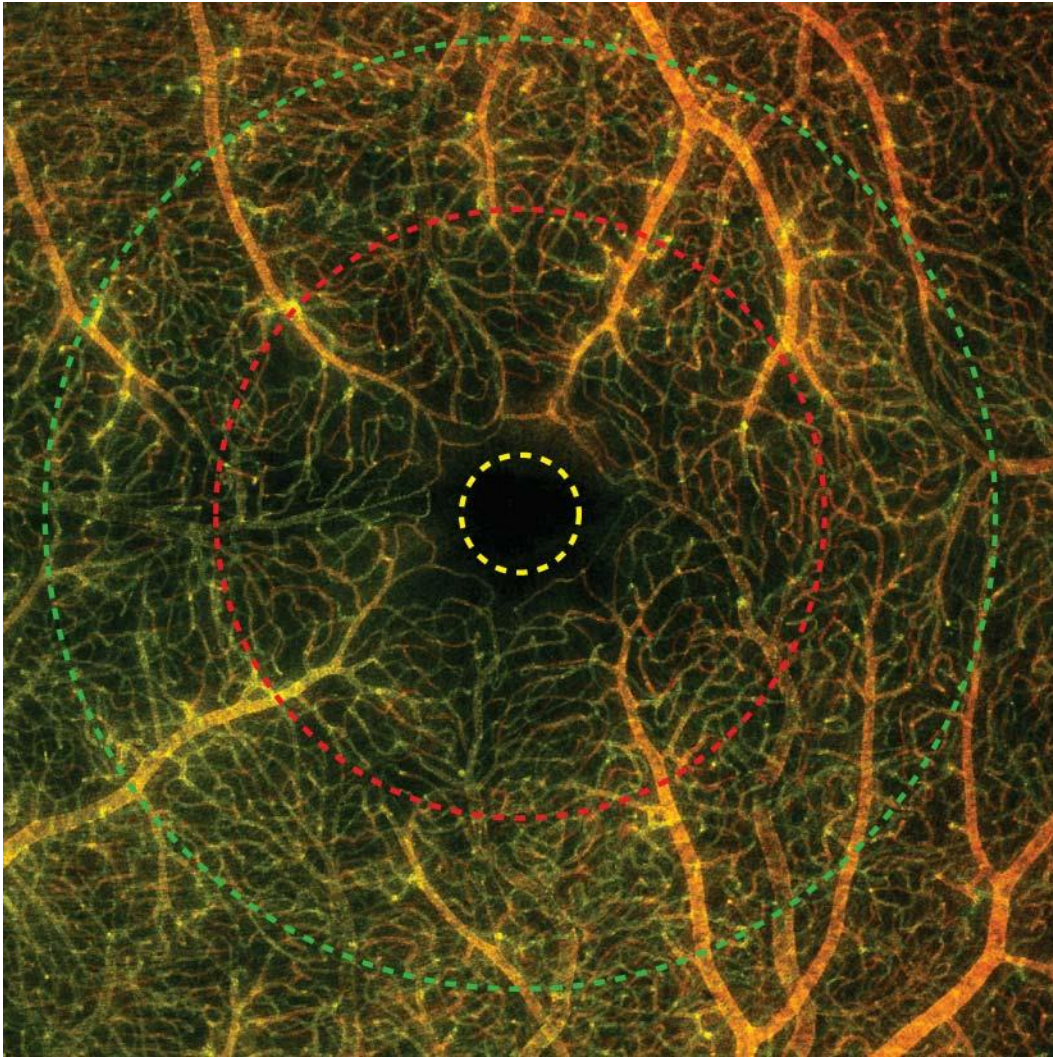


Figure 1.5. Confocal image from the macula region of a 66-year-old donor. The area imaged measured 3180 by 3180 μm . This image was pseudocolored to show the microvasculature at the different depth. Dashed concentric circles: foveola, fovea, and parafovea. Figure obtained from[9].

The choroidal vessels come from the central retinal artery and have a different blood supply than the retinal vessels described above. The choroid layer feeds the outer retina. The choroid consists of four layers, which are Haller's layer, Sattler's layer, Choriocapillaris and Bruch's membrane. In this thesis, the work focuses on the retinal vessels only.

1.1.3. AMD and DR

Age related Macular Degeneration (AMD) is a progressive and irreversible disease and one of the leading causes of vision loss for people over the age of 50 worldwide. There are two basic types of AMD, dry and wet. In dry AMD, lipids get accumulated in the Bruch's membrane (BM). The blockage results in a decreased oxygen supply from the choroidal blood vessels for the photoreceptors that lead to central vision deterioration. Wet AMD is much more risky for severe central vision loss. The problem with wet AMD is that new blood vessels are developed to supply more oxygen to feed the retina, and these new vessels would break through Bruch's membrane from the choroid. However, these new vessels are not welcomed because they are fragile and easy to break. These abnormal blood vessels cause leakage and bleed into the subretinal space, forming blisters and cysts of fluid that damage the retina and affect vision.

Diabetic retinopathy is a side effect of diabetes that affects the retina and can cause blindness. Too much sugar in the blood can damage the small blood vessels that nourish the retina, and there is a high chance to even block the vessels completely. When there is less blood supply to nourish the retina, new blood vessels start to grow. These new fragile vessels can grow along the retina as well as on the surface of the vitreous, and they leak easily which could result a severe vision loss or blindness.

In order to find a treatment of AMD and DR, we need to better understand the pathogenesis of these diseases utilizing various imaging modalities. In the next section, few imaging techniques that have been well developed and used in the research facilities and hospitals are introduced.

1.2. Optical Imaging modalities used for AMD and DR

The unique properties of the eye make it suitable for non-invasive optical imaging. A thorough review of all imaging technologies for the eye is beyond the scope of this thesis. Instead, here we focus on Optical Coherence Tomography (OCT), and commonly used techniques for imaging the retinal vasculature.

1.2.1. OCT

OCT is a non-contact, non-invasive medical imaging modality for micrometer scale sub-surface imaging of biological tissue over small distances [10–13]. OCT is similar in principle to ultrasound, but the imaging is performed by measuring light instead of sound. OCT is most commonly used to study the morphology of the retina such as shape and thickness, etc. For example, the structure of different retinal layers can be identified, and thickness measurements can be performed to study the pathological behavior or treatment responses for individual layer. It is greatly used in ophthalmic imaging and it is important as a non-invasive retinal imaging tool to accelerate drug development and gene therapy by basic scientists and medical researchers. Over the last 20 years, commercial OCT systems became available in the clinics and hospitals, and this imaging modality has become a regular checkup routine for patients that suffer eye problems. However, for certain diseases (AMD, DR), structural information is not enough, and we need functional (blood flow) information as these diseases affect retinal circulation.

1.2.2. Fluorescein Angiography

Imaging blood flow is very important because abnormal circulation is the leading cause of irreversible blindness in diseases such as DR and AMD. In the clinic, Fluorescein Angiography (FA) is commonly used to visualize retinal blood vessels located at the back of the eye. However, this technique requires the injection of exogenous contrast agents, which is commonly associated with minor side effects and a small but significant risk of allergic reaction and even death [14]. Moreover, these techniques only provide 2D information (*en-face* view of vasculature). Therefore, there is a clinical demand for a non-invasive approach to provide visualization of the microvasculature within the retina layers. OCT can be extended with a functional aspect to detect blood flow. There are many different techniques to do so, such as phase variance, speckle variance, and etc. More details are provided in Chapter 2.

1.3. Outline of thesis

The remainder of this thesis is organized as follows. In chapter 2, a brief theoretical background for OCT is presented. An emphasis is placed on my development of custom imaging systems to extract the structural information of the retina that were developed for small animal imaging. This is followed by an introduction of various extended OCT methods with a functional aspect to detect blood flow that are also applicable to human retinal imaging. Chapter 3 details a real time implementation of speckle variance OCT utilizing a graphic processing unit (GPU) for visualization of retinal vasculature networks in human retina. Chapter 4 demonstrates a follow up comparison study between speckle variance OCT and fluorescence angiography for human retina. Chapter 5 describes two clinical studies utilizing this svOCT system developed in my PhD. Chapter 6 described a GPU implementation of Graph Cut segmentation to enhance the visualization of the svOCT, and to generate retinal colour-coded thickness map. Lastly, the thesis ends with a summary and future work.

1.4. Contributions

At the early stage of my PhD, my work was focused on the quantification of retinal degeneration as well as the response to drug treatments for rat models of vision robbing diseases utilizing the structural information that OCT provides, for example measuring the thickness of the retinal layers. The results contributed to one published paper [15], and one manuscript that has been submitted for publication [16]. Later on, I was involved in a new research direction with the ultimate purpose of using the eye as a window to the brain in order to study Alzheimer's disease (AD) mouse models. The preliminary work required me to learn and collect data from imaging modalities other than OCT, such as scanning laser ophthalmoscopy (SLO), confocal SLO for autofluorescence detection, and magnetic resonance imaging (MRI) for brain data. Furthermore, I found reports in the literature that there may be changes in retinal vasculature due to AD [17]. Combined, this inspired me to focus on the functional aspect of retinal imaging, which is to use OCT for blood flow detection. I implemented a real-time blood flow imaging approach with speckle variance OCT using a GPU, which was published in J. of Biomedical Optics [18]. This real-time approach greatly increased the

efficiency of data acquisition, and provided good image quality for both mouse and human retina. I then validated the svOCT system by comparing the images acquired by svOCT with fluorescence angiography for both healthy and diseased volunteers, and this work was submitted for publication in 2014 [19]. Combined with conference presentations, this work brought interest from vision research groups such as Eye Care Centre at Vancouver General Hospital, and University of Western Australia. By collaborating with them, four research projects were collaboratively designed targeting publication in ophthalmic journals [20–23]. I contributed to this work through an extensive amount of clinical data collection, processing, and analysis of this data, which involved more than 100 volunteers including both healthy and patients with retinal diseases such as diabetic retinopathy, age-related macular degeneration, retina vein occlusion, and glaucoma. Currently, the svOCT human system is being used in the clinic for day-to-day blood flow imaging.

Chapter 2.

Background

In this chapter, the principles behind OCT are presented. This is followed by a quantitative analysis of retinal OCT for a rat model of glaucoma with comparison to histology. Lastly, functional extensions of OCT and several common techniques are introduced.

2.1. OCT

Optical Coherence Tomography (OCT) is a non-contact, non-invasive medical imaging modality for micrometer scale sub-surface imaging of biological tissue over small distances [10–13]. OCT is similar in principle to ultrasound, but the imaging is performed by measuring light instead of sound. The theory of OCT has been well established and discussed [10]. OCT uses the principle of low coherence interferometry (LCI) to provide structural information of the tissues being imaged. In Figure 2.1, three configurations of OCT are shown. The core of these OCT systems is based on a Michelson interferometer-type configuration. Briefly, light from a low coherence source is divided by a 2x2 fiber coupler into two paths: the sample and the reference. The back reflected light from both paths recombine and interfere to produce fringes corresponding to the optical path length mismatch between these two paths, Δz .

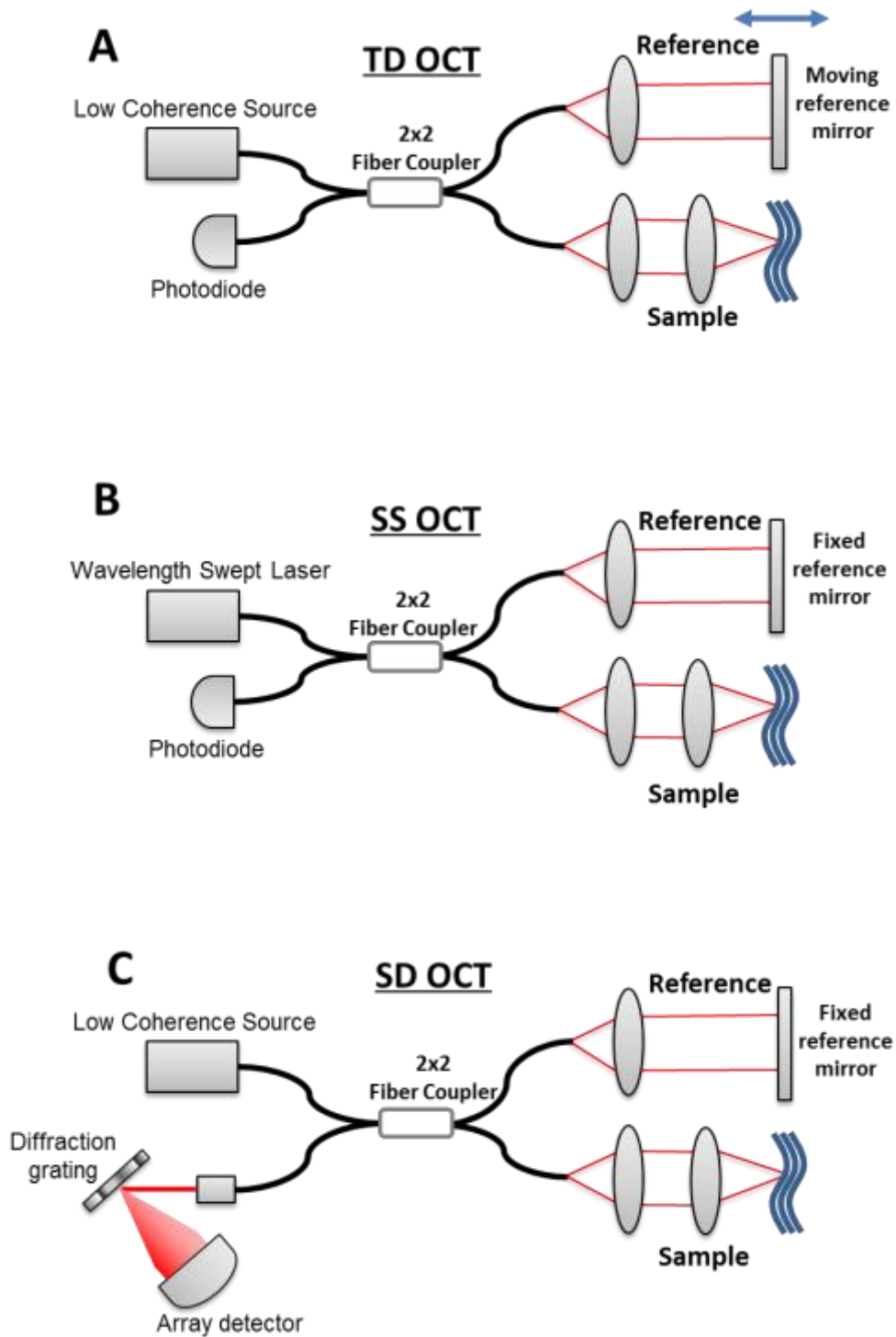


Figure 2.1. Basic schematic of different types of OCT system. (A) Time Domain OCT. (B) Swept Source OCT. (C) Spectral Domain OCT.

The first type of OCT developed was time domain (TD), which utilizes a mechanical moving part to axially scan the reference mirror position as shown in (Figure 2.1A). The information along the axial direction is accumulated over the longitudinal scan time. TDOCT measures the time of flight of the light. However, the line rate of TDOCT is slow and not practical in ophthalmologic imaging due to the limitation of mechanical scanning technologies. Later on in 1995, the Fourier domain (FD) OCT was first described by Fercher et al. [24], and FD OCT was then developed to increase acquisition rate and system sensitivity [25–27]. FDOCT systems have two configurations: Spectral Domain (SD) OCT (Figure 2.1B) and Swept Source (SS) OCT (Figure 2.1C). The SD OCT system uses a broad bandwidth light source and a grating to spatially disperse the spectrum across an array-type detector. The interference between the reference light and the back-reflected light from the sample are measured as a function of wavelengths. The SS OCT uses a narrow band laser which sweeps across a broad spectrum and a photodiode as detector, encoding the spectrum as a function of time.

Focusing on FDOCT, the equation for the spectral interferogram acquired at the detector can be written as,

$$I_D(k) = S(k)[R_S + R_R] + S(k)[2\sqrt{R_S R_R} \cos(2\Delta z k)], \quad \text{Eq 2.1}$$

where k is the wavenumber, and $S(k)$ is the source spectrum in units of k . In FDOCT, the optical path length difference is encoded by the frequency of the interferometric fringes as a function of the low coherence light source spectrum. By using the Fourier transform, the frequency content of the acquired signal can be extracted. The equation after taking Fourier transform of Eq 2.1 is written as,

$$\hat{I}_D(z) = \hat{S}(z)[R_S + R_R]\delta(z) + \hat{S}(z)2\sqrt{R_S R_R}[\delta(z - 2\Delta z) + \delta(z + 2\Delta z)]. \quad \text{Eq 2.2}$$

The Fourier transformed signal in Eq 2.2 is called an Axial Scan (A-scan) and represents the depth information at a single point on the surface sample. An OCT A-scan contains the depth information at one location of the retina. A series of laterally adjacent A-scans are acquired and combined to form a volumetric image as illustrated in Figure 2.2. This is called a 2D B-scan, and is a cross-sectional image. The volumetric

scan is generated by acquiring many of these B-scans along the y direction. The *en-face* view is a 2D projection view which is generated by summing up all the values along the A-scans (z direction).

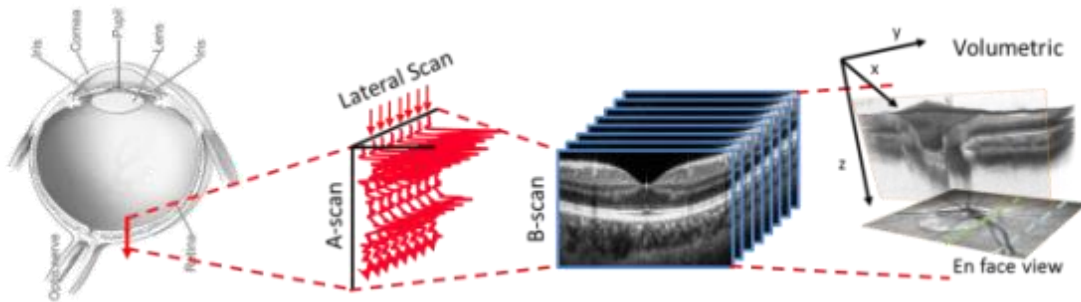


Figure 2.2. Graphical illustration of the technical terms used in OCT.

OCT has become an indispensable tool in ophthalmic practise for the diagnosis of many ocular diseases that involves the macula and ONH[28–36]. It is well known for providing structural information, for example, in retinal imaging the different retinal cell layers can be identified. Thickness measurements can be performed to study the pathological changes or responses to treatment for each individual retinal layer. A representative cross-sectional OCT image is shown in Figure 2.3, which indicates all the retinal layers at the fovea region in a human eye.

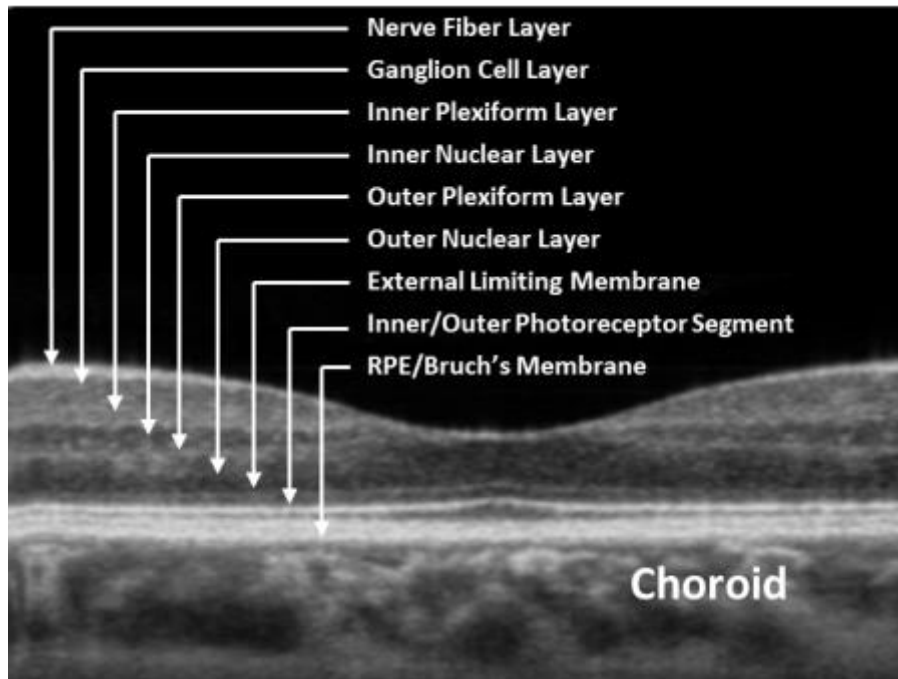


Figure 2.3. Target retinal layers of a representative cross-sectional OCT image centered at the macula.

2.2. Processing steps for FD OCT

The equation presented in Eq 2.1 masks some of the details for practical OCT imaging. When acquiring the interferogram, several processing steps are applied to generate the final retinal OCT images. The method of processing for SDOCT and SSOCT are similar, but differ slightly due to the details of the hardware used for each acquisition system. In SDOCT, the processing pipeline consists of five different stages: Linear Interpolation, DC Subtraction, Dispersion Compensation, Fast Fourier Transform (FFT), and Post FFT. In SSOCT, the data can be acquired uniformly spaced in wavenumber; therefore, no numerical interpolation is required. The dispersion compensation is also omitted because the wavelengths 1060 nm used for our SSOCT system for the retinal imaging is minimally affected by it because the dispersion is very low around 1060nm. Minor numerical dispersion compensation can be applied to perfect the image results; however, it may not worth the effort by adding a computational intensive processing step. Figure 2.4 shows a flowchart that represents the processing

pipeline used for both of our SDOCT and SSOCT systems. Brief description of each processing step will be described in the following paragraph.

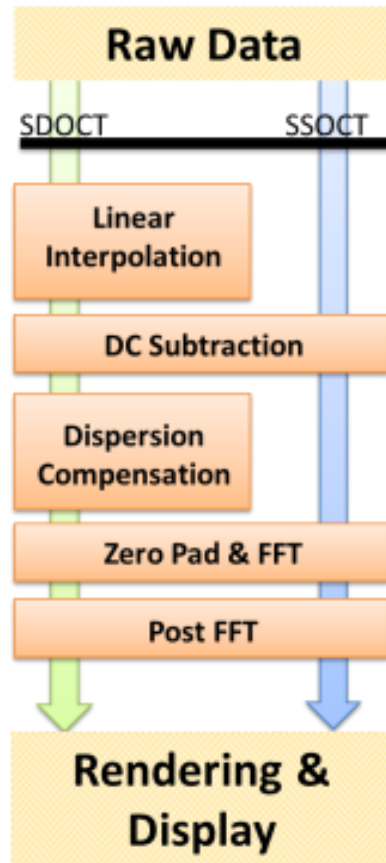


Figure 2.4. Processing pipeline for SDOCT (green) and SSOCT (blue).

Firstly, linear Interpolation is typically only implemented for the SDOCT system. A spectrometer is used for SDOCT system to acquire the spectral information. However, the spectra obtained are evenly spaced in λ -space (wavelength), and the k-space (wavenumber) is required for performing the Fourier transform (wavenumber and distance are Fourier transform pairs, just like time and frequency). Therefore, in order to output the correct image with the signal, the spectra needs to first undergo numerical interpolation to convert the data to be evenly spaced values in wavenumber. A linear interpolation approach is implemented to provide a satisfactory performance in terms of quality as well as the processing speed. Secondly, DC subtraction is implemented to remove the DC components due to the non-interfering components of the reference arm. A representative DC spectrum is acquired by averaging many interferograms; and by

subtracting the DC spectrum from the raw signal, the interferometric fringe-only data can be obtained. Thirdly, Dispersion Compensation is implemented by numerically adding a phase term to the interferograms before performing the Fourier transform [37]. Dispersion is the term used to describe the effect that optical materials have a different optical path length for the range of wavelengths used in the low coherence source. For the light source used in the SDOCT system, which is ~830 nm range, the optical dispersion is significant and degrades the image quality. Physical dispersion using glass blocks can be used, however, it is not sufficient enough due to subject variation in terms of different eye lengths. In order to achieve high image resolution, matching the path length difference of two paths (arms) with numerical dispersion compensation is required. Lastly, Zero-Padding, FFT, and Post FFT are implemented to transform the interferometric fringe information into the final OCT images. FFT is executed to transform the interferogram information into the corresponding frequency information. The output of the FFT is symmetric, which has a positive and a negative frequency. And each of them only has a resolution of half the original number of data points. Therefore, in order to obtain an equal resolution, zero-padding is implemented prior to FFT to increase the number of data points to the twice of the original size to produces an FFT with equal resolution as original. After FFT, the post FFT process could involve three steps. The first step is to apply the modulus function on the entire set of complex numbers to convert into real numbers. The second step is to apply a logarithm function to generate a representation of the intensity levels into their equivalent decibel (dB), which compensate for the large variances in the intensity signals. The final step is to normalize the FFT values for display purposes.

2.3. Quantitative analysis in animal models with FDOCT

Animal models are commonly used in vision research to study pathology of diseases and development of treatments; studies from our research group on this topic include [38–42]. My early work involved quantitative analysis of retinal OCT for rodents that contributed to publication [15]. This study aimed to evaluate glaucoma-like features in the rat episcleral vein cauterization (EVC) model using multiple in vivo and in vitro measurements. Glaucoma is a chronic, progressive, irreversible optic nerve neuropathy,

which is characterized by sustained loss of RGCs, the neuron of the retina, and progressive loss of the vision field [43]. The exact causes of glaucoma still remain unknown, even with many risk factors been identified [44]. One of the most common risk factors is the elevated intraocular pressure (IOP). In this study, the rat models have been undertaken EVC procedure to induce ocular hypertension (high IOP) [45]. In the rat models that have high IOP, a loss of RGCs is expected as time progresses. FDOCT was used to monitor the thickness of the neural retinal layer *in vivo*. The RGCs were labelled with Fluoro-Gold, and the final pictures of the dissected retina were taken with Zeiss fluorescence microscope (Carl Zeiss Meditec., Jena, Germany). The cell counting was performed both manually and automated using imaging software for comparison and validation of the *in vivo* retinal thickness measurements.

The results for this study are shown in Figure 2.5. With the FDOCT images, the thickness of the combined retinal layer including NFL, GCL and IPL was measured from *in vivo* data. The progressive degeneration of the ECV retinas was detected by the thinning of the retina over time in the same animals, as shown in Figure 2.5E. Compared to the normal control group, the combined thickness of NGI was reduced from $\sim 72 \mu\text{m}$ to $\sim 49.1 \mu\text{m}$ 6 weeks after ECV (Figure 2.5F). The ECV retinas had significant thinning compared to the normal control retinas starting from week 2 onwards. The *ex vivo* histology for this project was performed by the co-authors [15]. Quantification of the RGCs counting from the histological cross-sectional image in Figure 2.5C shows that 1 week after ECV, RGCs are reduced to 96% of normal control group, and after 6 weeks of EVC, RGCs were reduced to 75% of normal control group. This indicates an average of 4% RGCs death per week (Figure 2.5B). Figure 2.5D demonstrates the representative *en-face* view of retina sections from three retinal layers (GCL: left; ONL: middle; INL: right). These retina sections were hematoxylin-eosin stained, exposed to a primary (NeuN) and secondary (rhodamine-conjugated) antibody [15], and detected by fluorescence microscopy. Compared to the normal control, there was a noticeable loss of RGCs in the ECV retinas (glaucoma). As result, we showed a 3-5 μm thinning per week in the NGI layer based on the FDOCT measurements, which correlated with the 3-4 % per week RGC loss in histology. After 6 weeks of chronic IOP elevation due to EVC, the nearly 25% of RGC were lost, and the thickness of the NGI also had reduced by 25%-30%. Both the RGC loss and retinal thickness measurement in FDOCT had a

significant difference between the control eye and the treated eye starting from the second week after cauterization.

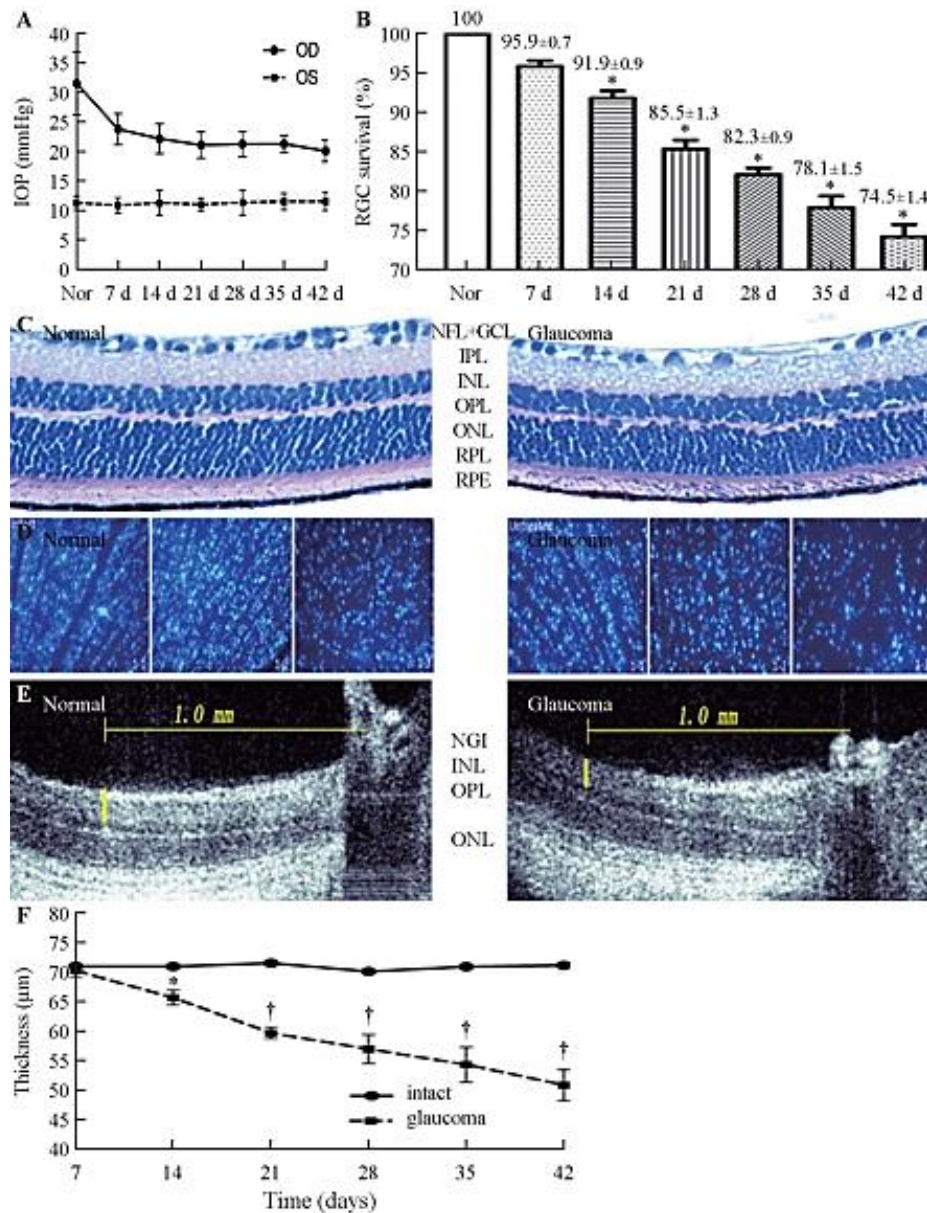


Figure 2.5. Histopathological validation of the EVC model. **A:** Measurements of intraocular pressure (IOP). **B:** Quantification of Fluoro-Gold labelled RGCs. **C:** Representative pictures of Fluoro-Gold labelled RGCs. **D:** Hemotoxylin-eosin staining of sections. **E:** Representative sections of in vivo FDOCT B-scan images. **F:** Quantification of the thickness of intact and glaucomatous retinas from FDOCT measurements. (Image from [15])

This study used the FDOCT as a non-invasive, practical, reliable imaging modality to monitor retinal changes the same rat over time. From this study, the good correlation of FDOCT and RGC counting makes us believe the rat model prepared by this EVC method can be used to detect the structural change of the retina. Also, it validates FDOCT's capability of monitoring pathological retinal changes *in vivo*.

The next step in the ophthalmic application of OCT is the development of functional extensions of OCT, which allow non-invasive imaging of blood flow, blood oxygenation, and vessel morphology in the retina. In the next section, several functional extensions of OCT that have been developed over these years are presented and compared.

2.4. Function extensions for flow detection

Recently, several implementations of flow contrast imaging for FD OCT have been reported in the literature. The techniques which are phase-based are Doppler optical coherence tomography (DOCT) [46–48] Optical Microangiography (OMAG) [49–52], and phase variance OCT [53–55]. Some of the techniques are intensity-based such as Split-Spectrum Amplitude Decorrelation Algorithm (SSADA) [56] and speckle variance (sv) OCT [57]. For overviews of these techniques, please see review articles [58–60]. In the following sections, the methodology of each of these techniques is described.

2.4.1. Doppler OCT

DOCT is based on the principle that light interacting with moving particles cause Doppler frequency shifts in the interference signals [61–63]. It provides quantitative information such as flow rate of the blood vessels. DOCT requires dense scanning, and the phase difference is calculated by comparing consecutive A-scans acquired at the same location. Also, by measuring the angle between the blood flow and the incident beam, we can also get the flow velocity profiles within vessels. However, DOCT is very sensitive to the sample motion artifacts. Acquiring more A-scans is necessary which results to a significant increase of the imaging time to over these problems. Unfortunately, this leads to another problem which is not practical for *in vivo* imaging

applications especially involving humans. There are several groups who came up with different approaches to reduce the sample movement artifacts and increase the velocity sensitivity. DOCT is a great tool to detect large vessels, but not a good approach to determine capillaries and leakages due to their very slow flow rate. DOCT is quantitative, and very good for total blood flow imaging, especially in cases where the angle to the vessels can be determined. The angle is crucial in DOCT to obtain the true value for the absolute blood velocity.

2.4.2. OMAG

OMAG, on the other hand, can efficiently separate the static and moving scattering elements within tissue by modulating the spectral interference signals at a constant modulation frequency while acquiring a B-scan. The frequency modulation can be achieved by utilizing a moving reference arm at a constant velocity across each B-scan. The moving speed of the reference arm (modulation frequency) sets the velocity threshold, such that the threshold for detecting the fast or slow blood flow velocities can be adjusted. Similar as DOCT, OMAG is also capable of detecting the direction of the blood flow. This can be achieved by driving the reference mirror back and forth at a constant speed. When the mirror moves away from the incident beam, the blood flow can be detected if it is running towards the incident beam. On the contrary, when the mirror moves towards the incident beam, the opposite flow gets detected. The OMAG uses a modified Hilbert Transform and can be processed into two parts [49]: the positive part and the negative part. When the direction for moving reference mirror and blood flow both meet the requirements, and the red blood cells travels in a much faster rate than the threshold, these blood flow (red blood cells) will map into the negative part, which will be generating the perfusion functional image. Any small movements that are below the threshold will map into the positive part, which will be generating the static structural image.

Both DOCT and OMAG are dependent on the motion-induced Doppler frequency, which as a result the measurements are highly dependent to the angle and speed of the flow. They cannot detect the flow when it is too slow, or when the flow is

perpendicular to the incident light. However, these techniques are computationally intensive which are commonly performed in post processing.

2.4.3. pvOCT and svOCT

The pvOCT and svOCT are two recent developments for flow contrast imaging. The mechanisms of these two techniques are similar such that pvOCT identifies the phase difference between consecutive B-scans acquired at the same position of the sample, and svOCT identifies the intensity difference. Unlike DOCT and OMAG, pvOCT and svOCT are independent of blood flow direction. They are capable of detecting both transverse and axial flow. pvOCT requires precise removal of background Doppler phase shifts due to the axial movement of bulk tissue, and the resolution is also dependent on the phase noise in the OCT system and transverse tissue motion. There are mainly two processing steps for pvOCT, which are the phase change calculation, and phase variance. Compared to pvOCT, svOCT only has one processing step which is to calculate the variance within the intensity B-scans. The svOCT allows both a simple acquisition and processing algorithm, while providing similar vasculature network maps as the other techniques.

2.4.4. SSADA

SSADA is another intensity-based technique that has been recently developed [56]. The idea behind SSADA is to split the original full spectrum into multiple spectrums. Each of them has a narrow bandwidth which results in a low resolution (low-res) OCT B-scan after performing the Fourier transform. By intentionally lowering the axial resolution of the OCT images, the bulk motion noise along the axial direction can be minimized, as well as the flow detection along the transverse direction optimized. From the work presented in [56], 8 B-scans were acquired at the same location to form a BM scan. The spectral interferogram for each B-scan was split into 4 spectral bands. Therefore, a total of 32 low-res B-scans were generated. The decorrelation is calculated from 2 adjacent low-res B-scans from BM mode, which results in 7 decorrelations for each spectral band. A total of 28 decorrelation B-scans were then averaged to produce a final decorrelation image that contains blood flow information.

Compared to regular OCT, the flow contrast techniques require longer acquisition time in order to capture the functional information due to the repeated acquisitions. Most groups are performing these calculations in post-processing, so the image quality cannot be assessed and adjusted during data acquisition.

In real clinical use, the time to image the patients is limited, and therefore control of the data quality during acquisition is crucial, and acquiring usable data without real time feedback of the vasculature network can pose a great challenge. To overcome these limitations I was motivated to develop a real time approach to allow instantaneous visualization of blood flow during human retinal acquisition.

2.5. Summary

In this Chapter, the concepts of OCT were described in the context of small animal retinal imaging, and expanded to human retinal imaging. Functional imaging of retinal vessels was described, focusing on speckle variance and related techniques. In the next chapter, a real time blood flow contrast imaging with svOCT using a Graphics processing unit (GPU) is presented. Results are presented in both small animal retina, and later extended to human retinal imaging.

Chapter 3.

Graphics processing unit accelerated speckle variance OCT processing and display in real time

Flow contrast imaging with FDOCT is a rapidly emerging technology for angiography, which is visualization of blood vessels. Predominantly, the flow contrast work has been performed in post processing. A few notable exceptions have been presented in [64,65] where real-time flow contrast was demonstrated during acquisition; however the results were limited to 2D B-scan cross sectional images. For effective volume acquisition of flow contrast data, real-time visualizations of capillary networks via *en-face* projections of vasculature are highly desirable.

In this Chapter, a GPU accelerated processing platform for real-time flow contrast imaging presented. High speed OCT acquisition systems and the GPU accelerated processing platforms are used to acquire and process *en-face* retinal vasculature images in mice and in humans in real time. Firstly, the real-time svOCT processing for visualization of mouse retinal vasculature is integrated with a Spectral Domain (SD)OCT system. Next, the svOCT processing is incorporated with a 1060 nm, 100 kHz Swept Source (SS)OCT for human retinal imaging, demonstrating the potential for clinical applications in ophthalmology. Lastly, the implementation of svOCT GPU in an on-going Open Source project is introduced [66].

3.1. Acquisition and Processing components

Mouse imaging was performed with ethics approval of the University Animal Care Committee at SFU. The mouse retina data was acquired using a custom built SDOCT system with a superluminescent diode (Superlum) centered at 810 nm and FWHM of 100 nm. The spectrometer (Bioptigen) was operated at an adjustable line rate of up to

200 kHz for 1024-point A-scans using a CMOS detector (Basler). The volume acquisition size for this system was 1024x300x900 pixels and was acquired in ~1.35 seconds. The axial resolution was ~4.2 μm in tissue, and the lateral resolution was ~6 μm in the retina using a beam diameter of 0.5 mm at the pupil. For speckle variance calculation, at each B-scan location, three repeated measurements were acquired and performed. The SDOCT system used to acquire the mouse data had an inherently phase stable acquisition.

A custom built 1060nm SS OCT system was used for human imaging in this study. All human imaging was performed at the Eye Care Center at University of British Columbia (UBC)The Vancouver General Hospital (VGH) with consent obtained from all subjects before participation and with ethics review board approval from Simon Fraser University (SFU). The system was operating at a line rate of 100 kHz and using a 500MSPS digitizer (AlazarTech), with 1024 points per A-scan. The details of this system have been previously reported [35]. The axial resolution was ~6 μm in tissue, and the estimated focused spot diameter was ~17 μm in the retina using a beam diameter of 1.3 mm at the pupil. Retinal images in the foveal region were acquired from a healthy volunteer. The total acquisition time for an entire volume (1024x300x900) required ~3.15 seconds.

Figure 3.1 is a demonstration of speckle variance OCT data acquired in a human eye. At each location in the eye (Figure 3.1A), three B-scans are acquired to form a BM scan (Figure 3.1B). Figure 3.1C is the svOCT B-scan generated by performing speckle variance calculation. Figure 3.1D is a comparison between an intensity OCT image and svOCT image. In the svOCT image, the blood vessels are more visible as indicated by the bright white dots. While the capillaries are not visible in the intensity image, they are clearly visible in the sv OCT image. However, the B-scan only contains flow contrast information at a single cross section. In order to visualize the vasculature network, we need to generate the *en-face* projections using the svOCT information.

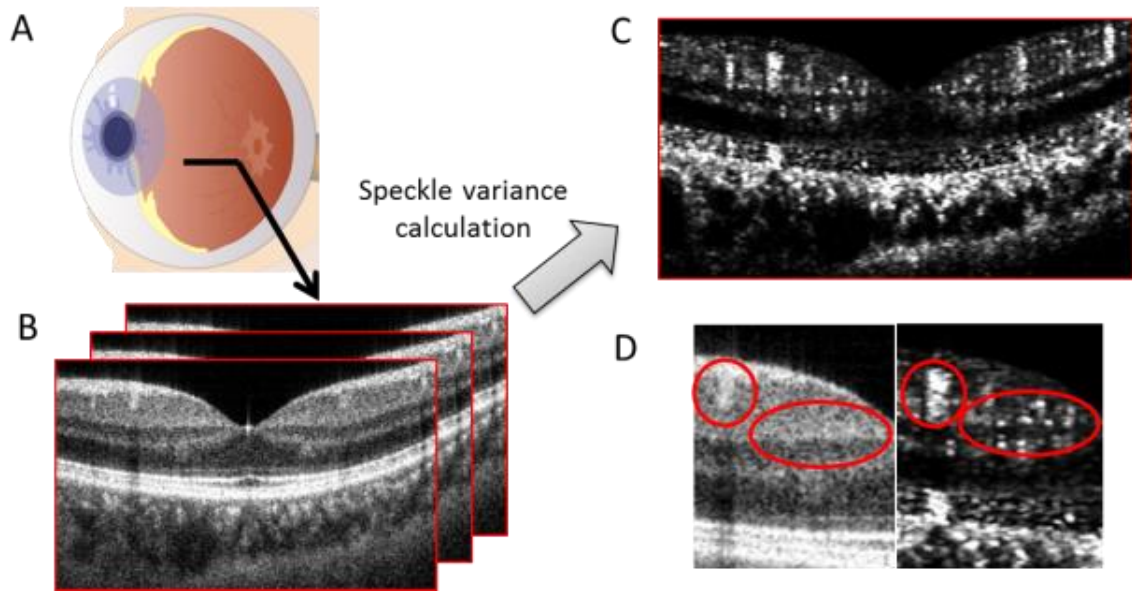


Figure 3.1. Diagram of speckle variance OCT data acquired and processing from (A) a human eye. Speckle variance is calculated with (B) multiple B-scans acquired from the same location of the eye and generate (C) one svOCT B-scan. (D) The intensity and svOCT B-scans are compared to show enhanced flow signals.

3.1.1. Processing

Our workstation for processing consisted of dual Xeon E5-2620 CPUs, 64 GB of RAM, and a NVIDIA GTX Titan GPU. For software development, we used Microsoft Visual C++ 2008 on a 64 bit Windows 7 operating system and CUDA Toolkit version 5.5 for programming the GPU. For profiling and optimization purposes, we use NVIDIA's Visual profiler software.

The GPU-based speckle variance implementation is built upon our previous work presented in [67]. In this work, we described our approach towards implementing the Fourier Domain Optical Coherence Tomography (FDOCT) pipeline, *en-face* image rendering, and volume rendering approaches to attain video rate visualization of high resolution volumes. The two methods of performing the FDOCT pipeline consisted of Spectral Domain (SD)OCT and Swept Source (SS)OCT. In SDOCT, the processing steps included wavelength-to-wavenumber resampling, DC subtraction, dispersion

compensation, FFT, and post-FFT operations. In our SSOCT acquisition system, the Axsun source is capable of acquiring uniformly in wavenumber-space, and the 1060 nm source suffered minimal dispersion through the optical system, therefore we omitted the wavelength-to-wavenumber resampling and dispersion compensation procedures in the processing pipeline [67].

For acquisition of data for speckle variance processing, our overall volume acquisition size was 1024-points per A-scan, 300 A-scans per B-scan, 3 B-scans per BM-scan (where a BM-scan is the set of all B-scans acquired at a single location within the volume), and 300 BM-scans in the entire volume. For each BM-scan, we performed the following speckle variance calculation in order to obtain the overall variance at each pixel location.

$$\mathbf{sv}_{jk} = \frac{1}{N} \sum_{i=1}^N \left(\mathbf{I}_{ijk} - \frac{1}{N} \sum_{i=1}^N \mathbf{I}_{ijk} \right)^2, \quad \text{Eq 3.1}$$

where i , j , and k are the indices of frame, width and axial position of the B-scan, respectively, and N is the number of frames per BM-scan [7]. In our case, the volume acquisition size was 1024 pixels per A-scan, 300 A-scans per B-scan, and $N = 3$ for a total of 900 B-scans (300 BM-scans) per volume.

Figure 3.2 is a profiler image demonstrating a single batch processing iteration in the GPU software. In this figure, we demonstrate the implementation of the Swept-Source based svOCT, where the FDOCT processing pipeline shown in 1) consists of DC subtraction, zero-padding, FFT, and post-FFT operations. In 2), the kernel for *en-face* projection rendering is shown, where we used the parallel reduction algorithm implemented in [67]. In 3), a kernel performing the speckle variance equation presented in Eq3.1 performed on all set of B-scans within each BM-scan, and executed using the batch-processing method described in [67]. Lastly, 4) demonstrates the rendering of three user selected *en-face* images using maximum intensity projection. The idle time presented after the fourth step represents the time required for sending the images from the GPU to the monitor for display, which occupies nearly half of the entire GPU execution timeline for processing and display.

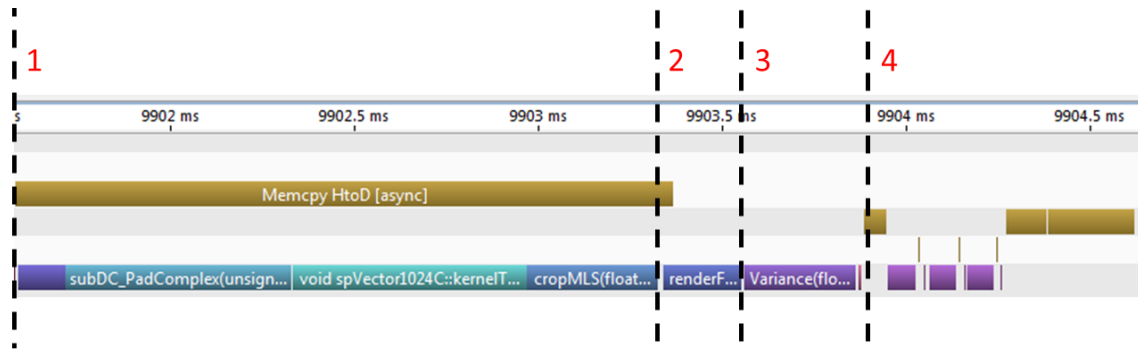


Figure 3.2. CUDA processing pipeline captured using the NVIDIA Visual Profiler.

The *en-face* projections are generated using sum-voxel or maximum intensity projection for all the pixels along the A-scan direction. Figure 3.3 presents the comparison of a single B-scan as well as the *en-face* projection between the intensity OCT and the svOCT. The vasculature network is clearly much more visible in the svOCT *en-face* projection image.

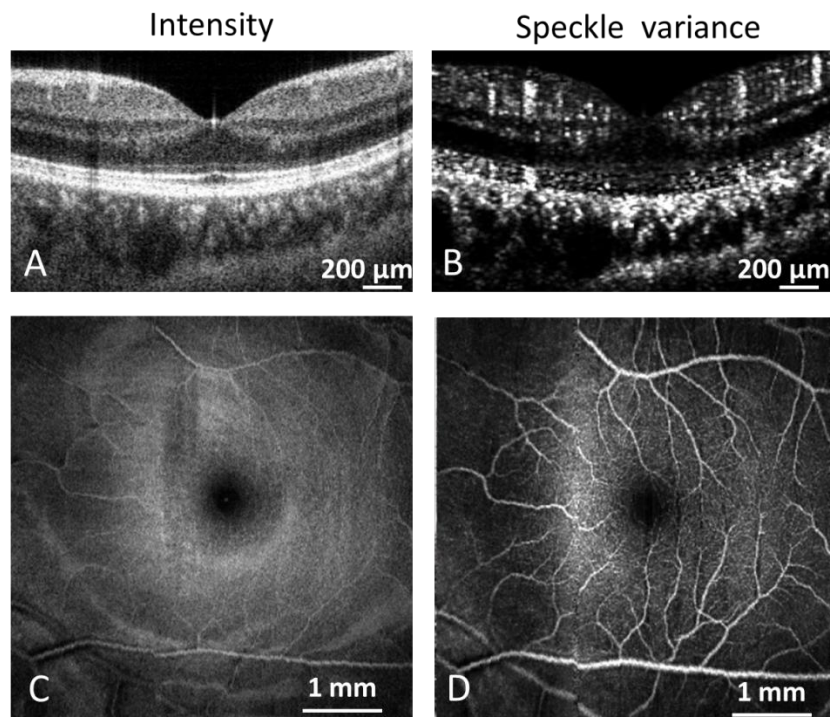


Figure 3.3. Comparison of (A) an intensity B-scan and (B) a svOCT B-scan. Comparison of (C) the intensity *en-face* view and (D) svOCT *en-face* projection.

By selecting different portions of the A-scans, different *en-face* projections can be generated to reveal vascular information within different retinal depths. Figure 3.4 is a demonstration of three *en-face* projections generated with corresponding selected regions from a retinal OCT volume (A) indicated by red (B), green (C), and blue (D), and super-impose. These three regions to generate a colour-mapped image (E).

The representative flow contrast images for three separate volumes acquired on a human volunteer are presented in Figure 3.5. The total acquisition time for an entire volume (1024x300x300x3) requires ~3.15 seconds for the human imaging system.

The volume in the first row is acquired in an area of 1.5x1.5 mm² at the macular region. The volumes in the second and third rows are acquired near the Optical Nerve Head (ONH) region for areas of 2x2 mm² and 1x1 mm², respectively. The svOCT *en-face* images on the right column show well defined capillary networks in the retina and at the bottom of the ONH with depth-distinguishable vasculature via colour-coding.

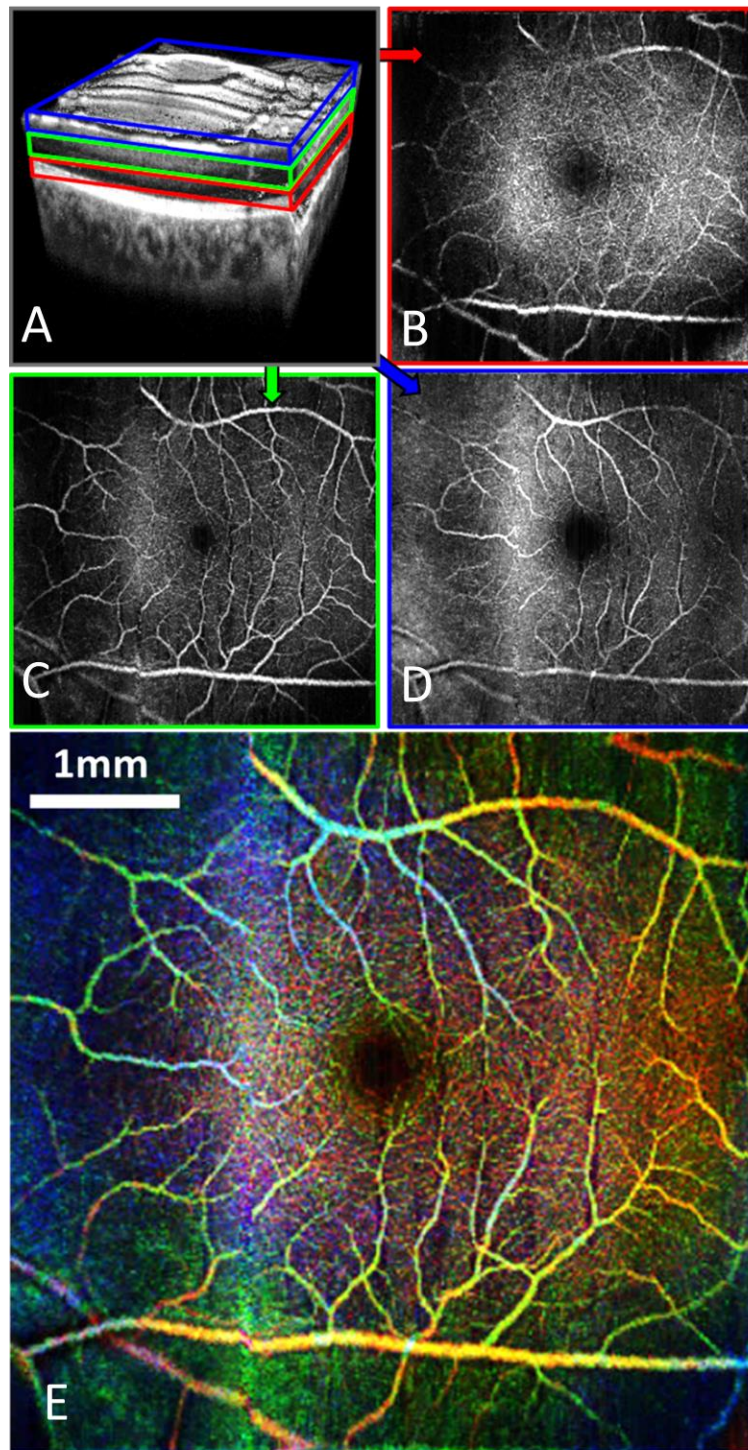


Figure 3.4. A representative volume view (A) with three user-selected depth layers indicated. The corresponding *en-face* views of each selected region in red (B), green (C), blue (D). A super-imposed image of all three regions into a single colour-mapped image (E).

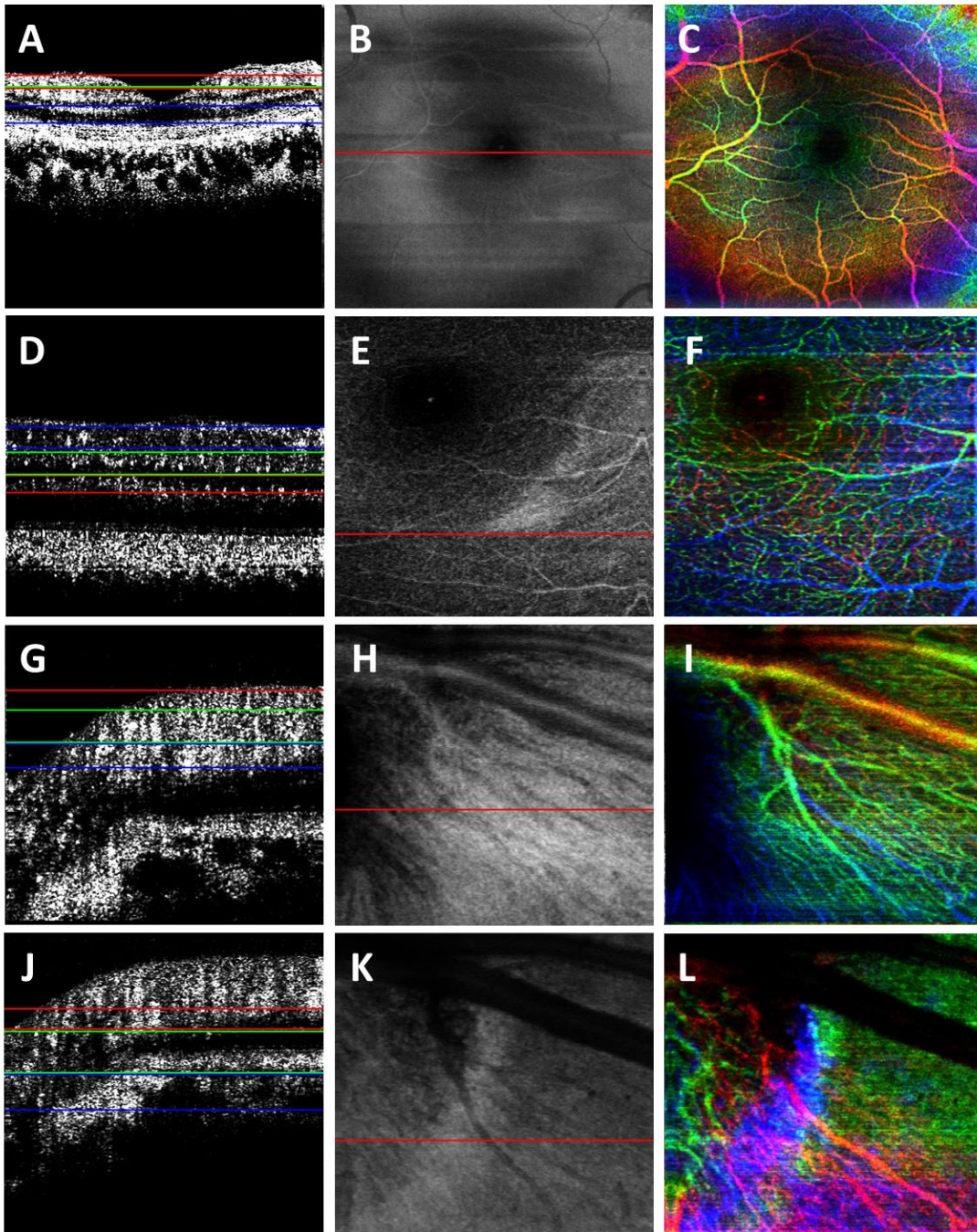


Figure 3.5. The images in A), D) and G) illustrate representative B-scans at the equivalent position of the red lines in the *en-face* images B), E) and H), respectively. The combined colour-coded svOCT *en-face* images corresponding to A), D) and G) are presented in C), F) and I), respectively. Imaging areas from the 1st, 2nd, and 3rd rows are: $1.5 \times 1.5 \text{ mm}^2$, $2 \times 2 \text{ mm}^2$, and $1 \times 1 \text{ mm}^2$, respectively.

3.2. Mouse svOCT Imaging

In addition to human imaging, the svOCT technique was also used for blood flow detection in the mouse retinal imaging. The SD OCT system is currently only used for mouse imaging. The mice are anesthetized during the imaging session, therefore the motion is small and mostly due to breathing. Our current acquisition speed is fast enough for satisfying speckle variance data collection. In general, the standard processing steps 1-4 are sufficient for imaging anesthetized animal models. However, human imaging is much more difficult. Since we do not anesthetize the subject, both eye and body movements dominate, which significantly affect the speckle variance results. Therefore, to minimize motion the artifacts, additional processing are implemented and applied to improve the image results.

The representative images in Figure 3.6 were acquired over an area of $1 \times 1 \text{ mm}^2$ in a mouse. The total acquisition time for an entire volume ($1024 \times 300 \times 300 \times 3$) requires ~ 1.35 seconds for the mouse imaging system. The overall standard speckle variance processing and display time took ~ 270 milliseconds for the same volume size, which is equivalent to rate of $\sim 1 \text{ MHz}$ per A-scan. For each row, the left column displays the cross-sectional scan at the location of the red line selected on the *en-face* intensity image in the middle column. The user dynamically selects the regions of interest, and the corresponding intensity and svOCT *en-face* images are generated using sum-voxel. This approach assumes a flat field of view throughout the volume (i.e., negligible curvature). In Figure 3.6(A), (D), and (G), the regions of interest were selected from the nerve fiber layer (NFL)/ganglion cell layer (GCL), the inner plexiform layer (IPL), and the outer plexiform layer (OPL), respectively. In Figure 3.6 (J)–(L), three user-selected regions of interest on the svOCT B-scan are distinguished using colour-coded lines, and the colour-coded image represents the superimposed svOCT *en-face* projections of all three vascular layers. Comparison of the intensity *en-face* (center column) with the svOCT *en-face* (right column) images reveals, significant contrast improvement for blood vessels with svOCT; for example, capillaries from the NFL/GCL are barely visible in Figure 3.6 (B) but are clearly distinguishable in Figure 3.6 (C).

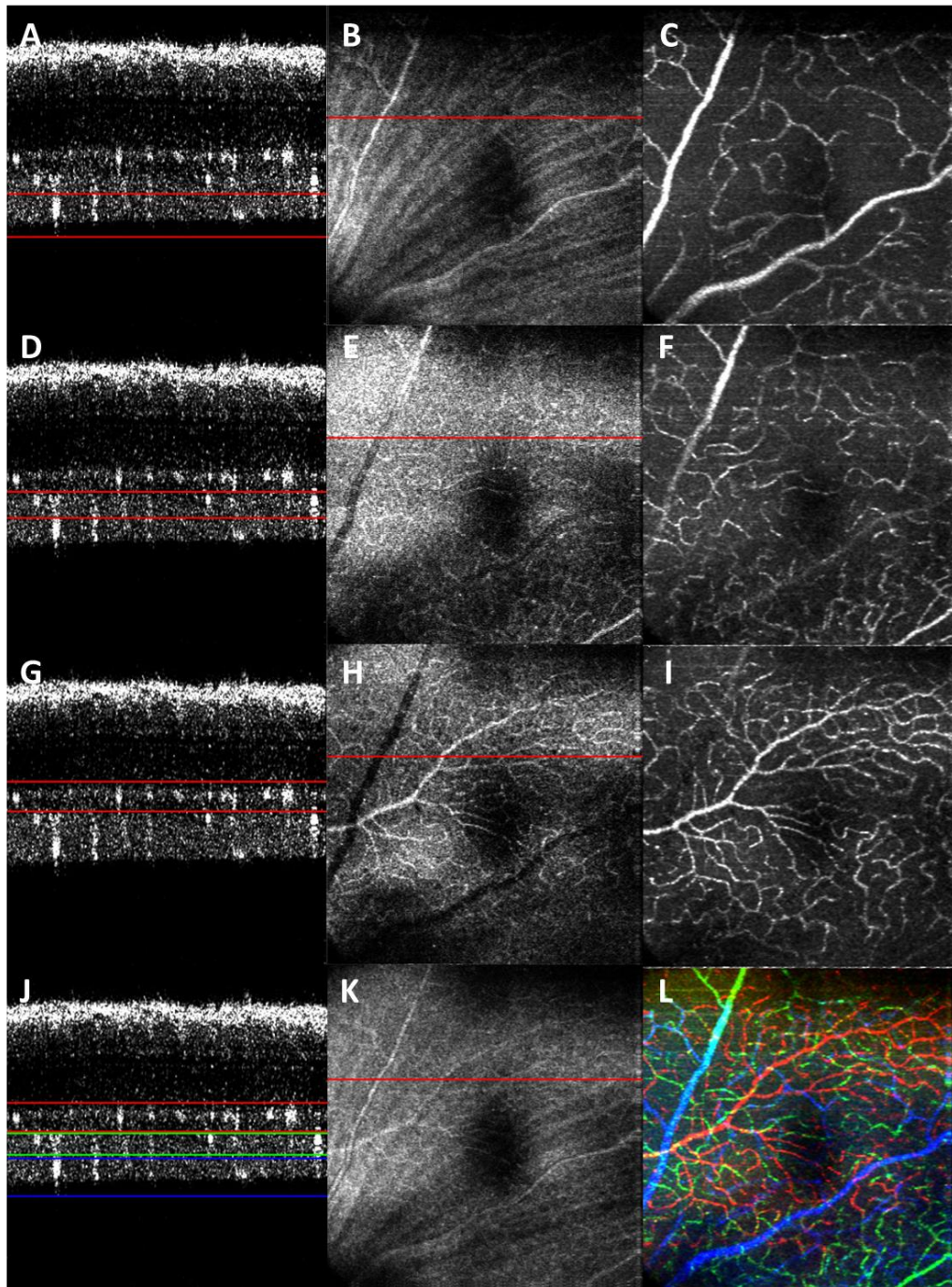


Figure 3.6. The svOCT B-scan images in (A, D, G) illustrate the selected depths of interest for an area of $1 \times 1 \text{ mm}^2$; the intensity *en-face* images are presented in (B, E, H); and the svOCT images are presented in (C, F, I). The B-scan (J) presents a colour-coded combination of (A, D, G), where each colour represents: NFL/GCL—blue, IPL—green, and OPL—red. The combined intensity *en-face* image of all depth regions of interest is presented in (K), and the superimposed colour-coded svOCT *en-face* image is presented in (L).

3.3. Additional processing for human clinical imaging

For svOCT, or any type of functional OCT for flow detection, motion artifacts pose a significant challenge to acquire good data. Usually, volunteers need a number of hours to practice in order to be able to control the breathing and keep focusing on the target while maintaining the posture. Clinical human imaging with patients is much more different and difficult than imaging trained volunteers in a laboratory environment, and training every patient before acquisition is not realistic. Therefore, additional processing steps such as motion registration were implemented to minimize the motion artifacts as much as possible during clinical imaging.

Figure 3.7 shows the various functions we implemented to minimize motion artifacts and improve image quality. Motion registration was performed based on subpixel image registration by calculating the cross-correlation in the fourier space [68]. In order to take advantage of the parallel processing power of the GPU, the motion registration was only performed between the B-scans that form each BM scan. Without motion correction, translational differences between B-scans result in a bright svOCT image and these motion artifacts appear as bright vertical stripes within the *en-face* images in Figure 3.7B. Figure 3.7C shows that the motion registration successfully eliminates a good portion of the motion artifact, thereby revealing more of the underlying vasculature. However, since registration is performed locally within each BM scan only, and not globally, larger motion artifacts that affect multiple BM scans are not correctable. These larger motion artifacts show up as thick stripes, which we remove using a notch filter to get a more pleasant *en-face* view.

In the case of human imaging, the added registration and filtering increased the overall processing and display times to ~645 milliseconds (~420kHz per Ascan) which is still beyond the acquisition speed of most conventional OCT systems.

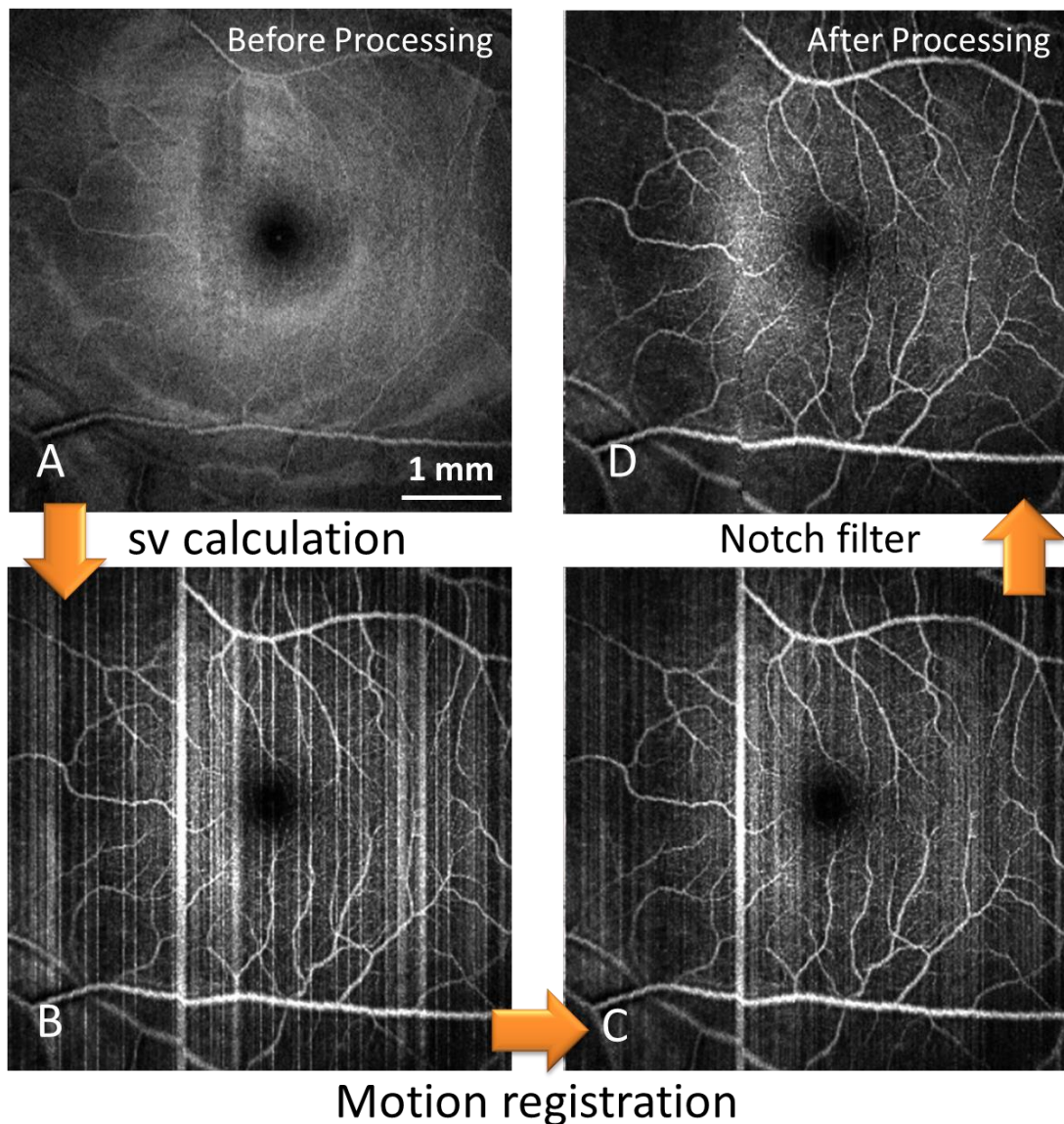


Figure 3.7. Functions implemented to minimize motion artifacts and improve image quality. (A) Intensity *en face* image; (B) svOCT *en face* image; (C) svOCT *en face* after motion registration and (D) svOCT *en face* after notch filter.

The same technique was also applied for blood flow detection in the optic nerve head (ONH) and ocular anterior chamber. The appearance of the structure and vessels inside the ONH looks distinctly as shown in Figure 3.8 and Figure 3.9. The lamina cribrosa from the ONH has a mesh-like structure of pores in the intensity *en-face* views, whereas the pores are no longer visible in the svOCT *en-face* images. Additional

representative retinal flow contrast images acquired at foveal region (A, B) and ONH (C, D) were acquired from human volunteers at ECC are presented in Figure 3.10.

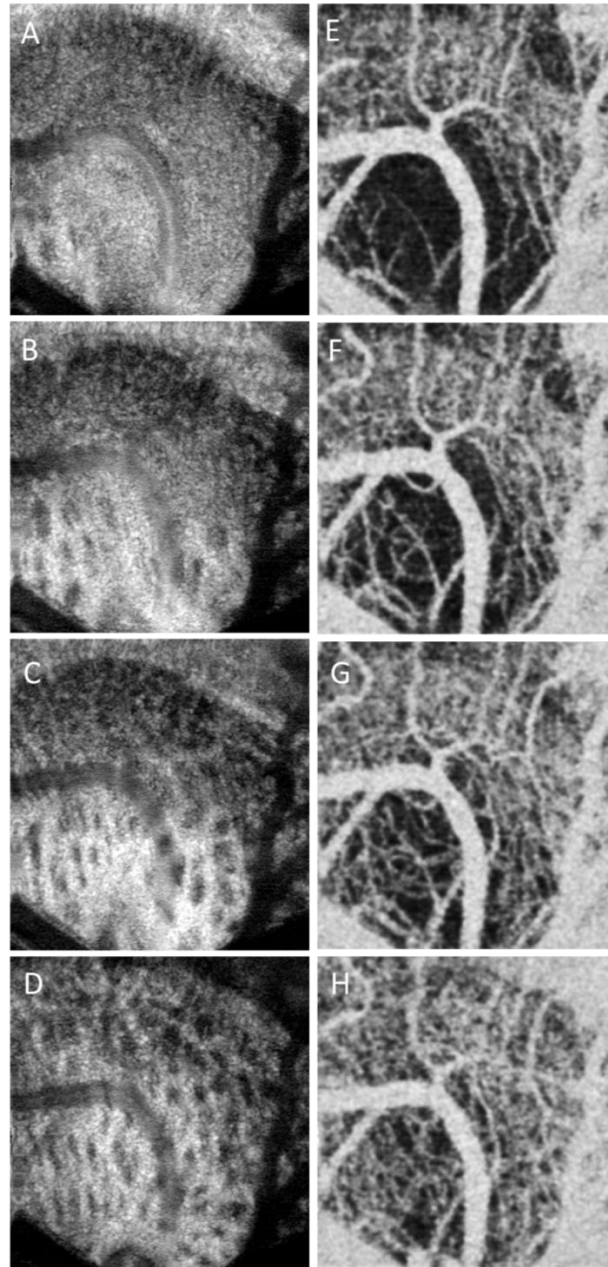


Figure 3.8. The intensity *en-face* views of different depth region inside the ONH (A-D) and the corresponding svOCT *en-face* views (E-H), respectively.

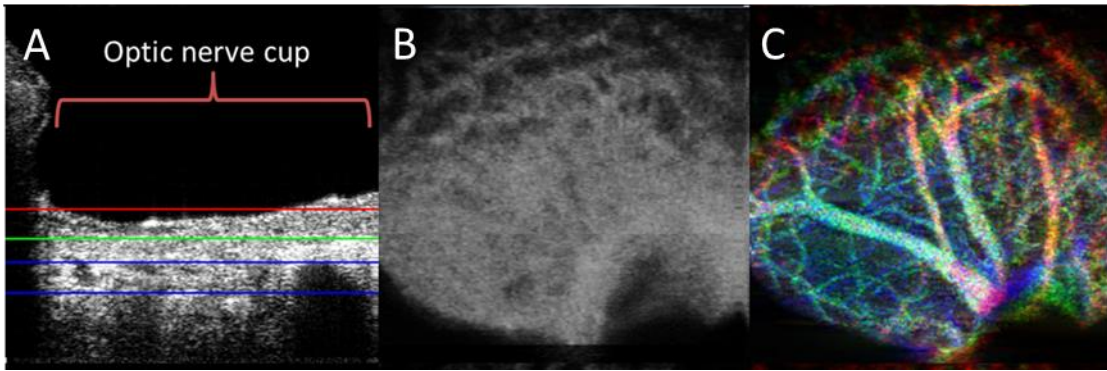


Figure 3.9. A representative B-scan acquired at ONH (A) with three user-selected depth layers indicated. The intensity *en-face* view generated by the entire selected depth layers (B). The superimposed svOCT *en-face* view of all three regions (C).

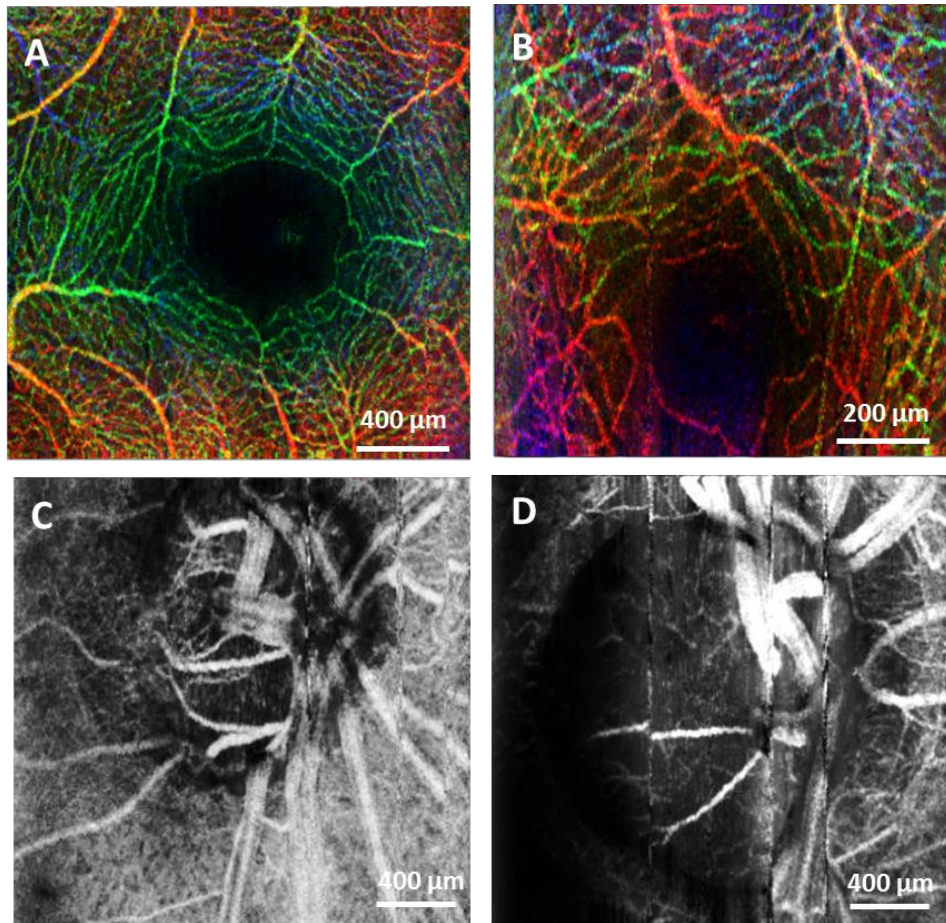


Figure 3.10. Representative colour-mapped sv *en-face* at foveal region with the field of view of (A) 2x2 mm², and (B) 1x1 mm². Flow contrast *en-face* projection at the optic nerve head acquired from a healthy volunteer (C), and a glaucoma patient (D).

Besides the retinal imaging, the svOCT processing was integrated into a 1310nm system which is also located in Eye Care Centre (ECC) for anterior chamber imaging. The representative image is shown as Figure 3.11, where the blood vessels in the iris can be clearly seen in the svOCT *en-face* but not in the intensity *en-face* view.

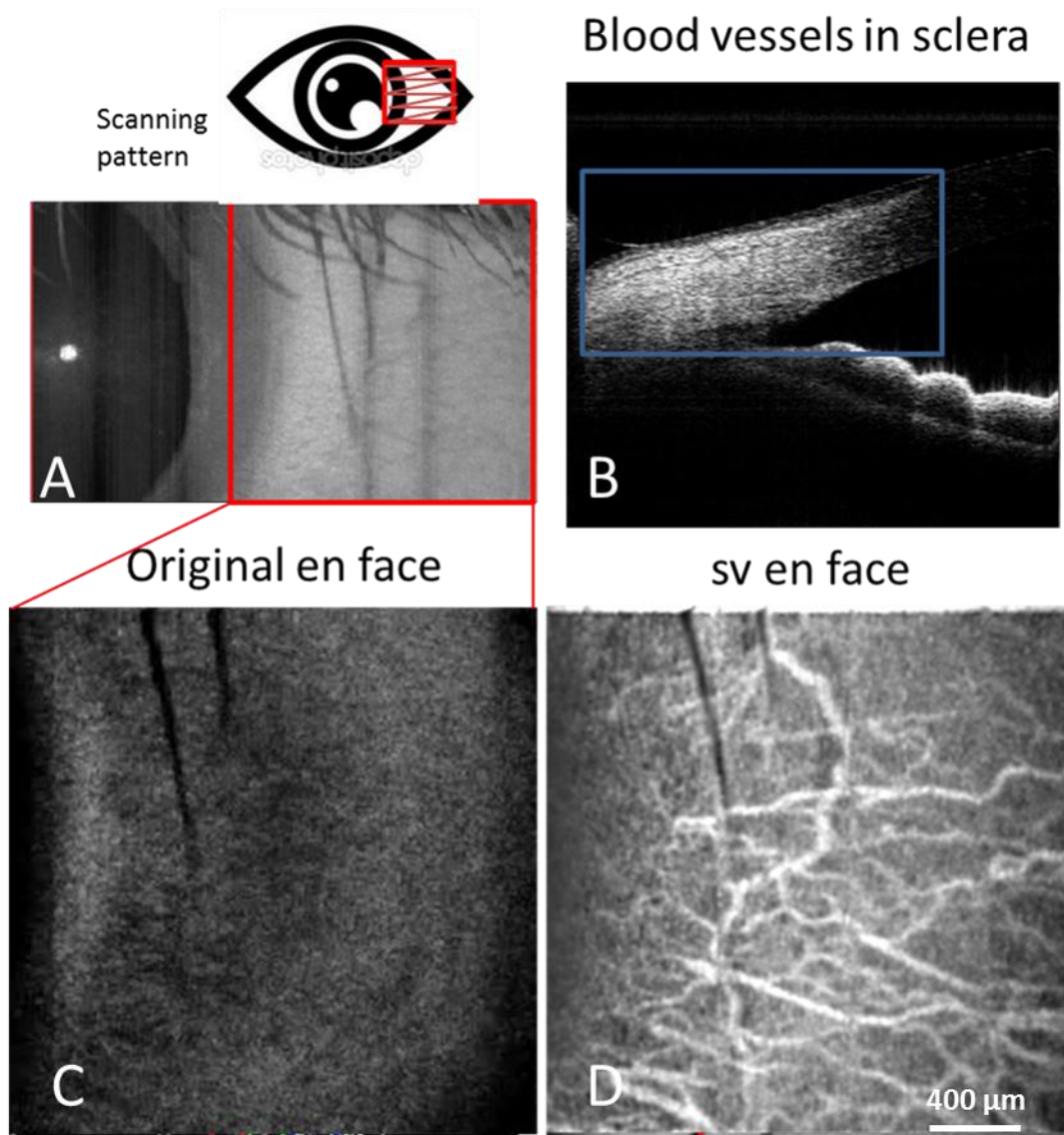


Figure 3.11. A representative *en-face* view (A) and a B-scan (B) acquired at the front of the eye (A). The intensity *en-face* view (C) and the svOCT *en-face* view (D).

3.4. Conclusion

We have demonstrated real-time flow contrast imaging on two separate systems for human retinal imaging and for mouse retinal imaging, and the GPU's high degree of efficiency in performance in both processing and display when given the correct optimizations. This technology has high potential for clinical applications including imaging of retinal angiography. Blood vessels are often seen in OCT intensity images with difficulty, such as in the NFL and IPL; therefore implementing svOCT enhances the contrast for visualizing both large and small vessels. The simplicity of the svOCT processing lends itself to real-time imaging, where flow contrast imaging is important to study various diseases affecting the retinal vasculature, e.g. diabetic retinopathy, ischemia, etc. Another possible application of this code is to use svOCT to facilitate the alignment to the same location on the retina based on visualization of the blood vessels in longitudinal studies. In addition, more computationally intensive algorithms can be used in post-processing for retrieving potentially higher contrast images, such as the pvOCT technique.

For human imaging, our implementation of svOCT was restricted to an area of $\sim 2 \times 2 \text{ mm}^2$ for resolving the capillary network. In order to increase the field of view, more A-scans need to be acquired to maintain the same sampling resolution. A faster FDOCT engine would be required to sustain the same volume acquisition rate, mitigating the introduction of greater motion artifacts. For the current system, a simple extension of tiled acquisition and mosaicking of adjacent volumes would also permit acquisition over larger areas [69]. Other simple techniques could also be used to limit subject motion, such as incorporating a fixation target and a bite bar.

The applications of real-time svOCT are numerous, such as monitoring progressive changes to retinal vessels in diabetic retinopathy in ophthalmology, and visualizing blood vessel networks in cancer research [70]. In the next chapter, a comparison study between results obtained using FA and svOCT will be described.

Chapter 4.

Comparison of svOCT and Fluorescence Angiography

In the previous chapter, we investigated a novel non-invasive and label-free optical imaging technique, speckle variance optical coherence tomography (svOCT), for visualising blood flow within human retinal capillary networks. The svOCT was implemented into a clinical prototype OCT with fast acquisition and high speed processing to provide real-time visualization of the vasculature network within the different retinal layers. To investigate the quality of microvascular detail acquired with this device, we compared images of human capillary networks acquired with svOCT and fluorescein angiography which is the clinical gold standard. We found that the density of capillary microvasculature acquired with the svOCT was visibly greater than FA. We also found that the capacity to generate *en-face* images of distinct capillary networks that are morphologically comparable to previously published histological studies. Finally, the customized svOCT system was demonstrated to non-invasively image the common manifestations of diabetic retinopathy. The results of this study suggest that this GPU accelerated svOCT has potential to non-invasively provide useful quantitative information about human retinal capillary networks, and may have clinical and research applications for the management of retinal microvascular diseases, a major cause of vision loss worldwide.

4.1. Introduction

In clinical ophthalmology, Optical Coherence Tomography (OCT) and fluorescence angiography (FA) are invaluable tools that are used for the diagnosis and management of retinovascular conditions such as diabetic retinopathy and retinal vascular occlusions. Current OCT technology has the capacity to provide high-resolution

histology-like anatomical information of the retina non-invasively. In contrast, FA provides wide-angle information of the retinal circulation and, in particular, is useful for identifying areas of blood-retina-barrier compromise. One of the limitations of FA is the need to inject fluorescein dye which is commonly associated with minor side effects. There is also a small but significant risk of anaphylaxis and death with FA (estimated at 1 in 222,000) [14]. It usually requires a full time nurse and additional specialized equipment for anaphylaxis which has more inherent costs than OCT which is non-invasive imaging. Furthermore, only limited information concerning depth along the z-axis can be acquired with FA.

Circulatory disturbances within regional capillary beds are important and early events in many retinal vascular diseases [71]. The ability to acquire *en-face* images of distinct capillary beds with current FA and OCT technology is however limited. Generating the *en-face* images of the vasculature networks is computationally intensive and usually processed off-line. In real clinical environment, the time to image patients is limited, and therefore control of the data quality during acquisition is crucial, and acquiring usable data without real-time feedback of the vasculature network can pose a great challenge. In order to provide an imaging tool to generate instantaneous visualization of the vasculature network in human retina, we used the real-time speckle variance flow contrast imaging system implemented on a high speed clinical prototype SS-OCT system with hardware accelerated processing which was presented in the previous chapter. In this study, we illustrate that this device has the capacity to non-invasively provide anatomical information of retinal capillary beds that is greater than what is acquired using standard fluorescein angiography. The images of retinal microvasculature were both acquired from healthy volunteers and patients. The results represent an important step towards facilitating retinal vasculature imaging in clinical settings.

4.2. Methods

This study was approved by the human ethics committee at the University of British Columbia / Eye Care Centre (ECC) at Vancouver General Hospital. All human imaging was performed with consent obtained from all subjects. I was in charge with

data acquisition and processing for svOCT, and the FA images were taken and provided by personnel at the ECC.

The details of the clinical prototype svOCT system have been described in Chapter 3. For speckle variance calculation, three repeat acquisitions at each B-scan location were acquired. The scan area was sampled in a 300x300(x3) grid, which required ~3.15 seconds. For subjects that cannot fixate well, the scan area was sampled in a smaller 300x200(x3) grid, which required ~1.8s.

All the svOCT B-scan images were generated by the GPU accelerated program, and the *en-face* images were generated in MATLAB. To correctly represent the vascular information within specific retinal layers, a semi-automated segmentation approach based on Graph cuts segmentation [33] was used in MATLAB as well. This method will be described more in details in Chapter 6.

The following qualitative assessments were performed in this study:

1. To determine if there was a difference in the morphology and density of capillary networks represented in svOCT and FA images (Figure 4.1). Comparisons were made between macular images from healthy human subjects that were imaged with these two imaging modalities.
2. To determine if svOCT has the capacity to isolate and image distinct capillary networks within the human retina (Figure 4.2). The perimacular region of a healthy human subject was imaged and semi-automated segmentation of B-scan images was used to generate *en-face* images of different retinal capillary networks. Images were acquired of histologically documented capillary networks including the nerve fiber layer (NFL) network, ganglion cell layer (GCL)/ inner plexiform layer (IPL) network and outer plexiform layer (OPL) network.
3. To determine if the common and serious complications of diabetic retinopathy could be identified using svOCT. Areas of retinal pathology, identified on FA were imaged using svOCT (Figure 4.3). Comparisons were made between FA and svOCT images.

4.3. Results

In the macula we observed greater capillary density in svOCT images compared to FA (Figure 4.1). We also found that svOCT was able to identify with greater precision the terminal capillaries around the foveal avascular zone.

The morphological characteristics of capillary networks in *en-face* images correlated closely with the results of previous histological studies performed on the human retina (Figure 4.2) [72,73]. We observed that capillaries in the NFL network were longitudinally orientated with a trajectory that was predominantly parallel to the direction of retinal ganglion cell axons in the NFL. In contrast, the capillaries in the GCL/IPL network demonstrated a complex three-dimensional organization. The capillary network in the OPL layer was found to be planar with multiple closed loops. Colour-coded projection of various capillary network images permitted us to explore important spatial vascular relationships within the retina and also allowed us to identify the change in capillary topography relative to retinal depth.

Figure 4.3 illustrates the FA appearance of a patient with proliferative diabetic retinopathy. Insets within the image demonstrate in great detail the morphological appearance of these eccentricities examined with svOCT imaging. Optic disk neovascularization is clearly seen using svOCT as are areas of capillary drop out within and outside the macula.

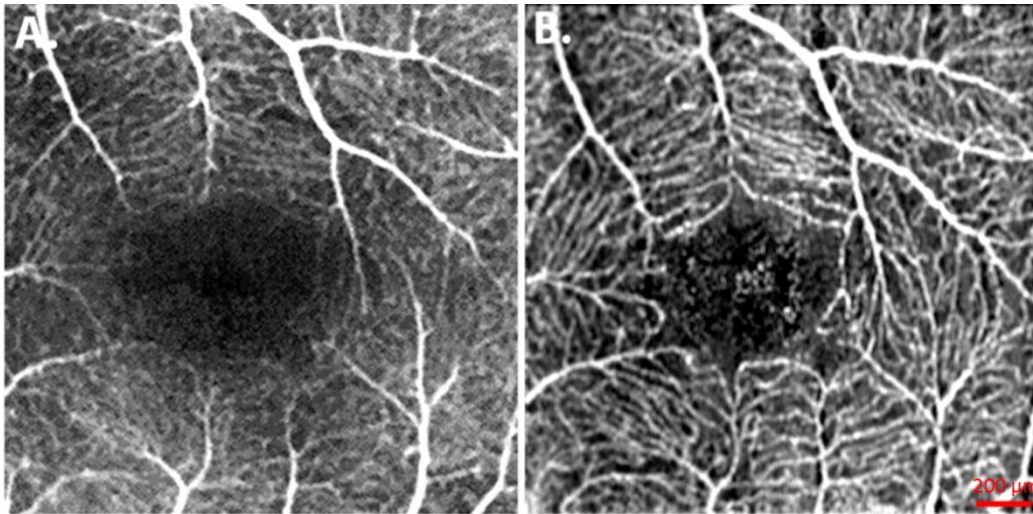


Figure 4.1. Human macula vasculature. Comparison between fluorescein angiography (A) and speckle variance OCT (B) images captured from a healthy subject demonstrates an observable increase in the density of capillary detail in the svOCT image (scale bar = 200 μm). The FA image was acquired with 40° field of view and cropped to correspond to the region acquired with the svOCT

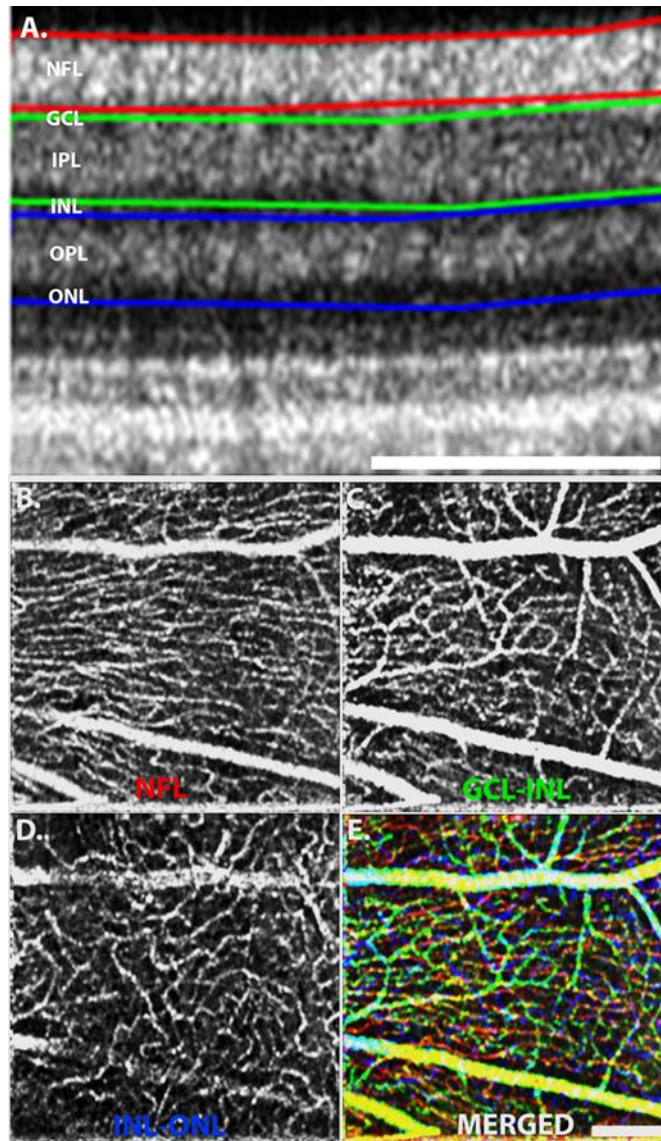


Figure 4.2. Isolation of distinct human capillary networks with speckle variance OCT. (A) Representative B-scan image of the human retina (A) demonstrates various inner retinal layers including NFL, GCL, IPL, INL, OPL and ONL. Semi-automated segmentation of B-scan images (red, green and blue lines) allows generation of *en-face* OCT images of different capillary networks within, and between, these retinal layers. The morphology of capillary networks within the NFL (B) and networks located between GCL and INL (C) and INL and ONL (D) bear close morphological correlations to previous histologic studies of these networks. Superimposing *en-face* images (E) also allows study of spatial relationships between various networks (scale bar = 200 μm).

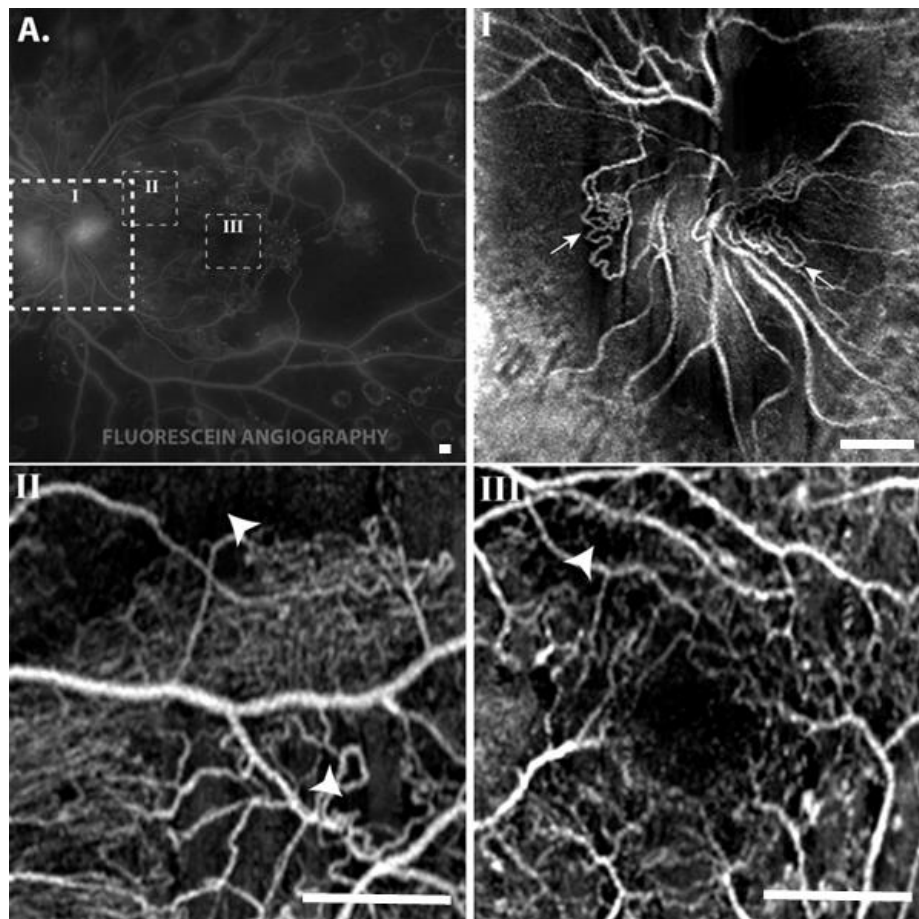


Figure 4.3. Application of speckle variance OCT to investigate diabetic retinopathy. Fluorescein angiography (A) of a diabetic patient demonstrates proliferative disease with marked retinal non-perfusion. *En-face* images of the optic disk (Inset I) acquired with svOCT clearly illustrates neovascularization of the optic disk (arrows). Speckle variance OCT images of the peri-macular (Inset II) and macular (Inset III) eccentricities also demonstrate marked capillary dropout (arrows) within these regions. (scale bar = 500 μm).

Figure 4.4 presents more comparisons from patients with DR. In Figure 4.4 A and B the macular and perimacular region are imaged. The detail of capillary information is visibly greater in the corresponding svOCT images (Figure 4.4D and E). This suggests that svOCT may be particularly useful for monitoring and detecting macular ischemia, an important cause of visual morbidity in diabetic patients. Figure 4.4C illustrates the angiographic appearance of retinal neovascularization with associated fluorescein leakage. The loss of surrounding vascular detail due to extravasation of dye is apparent on FA but it does not influence the quality of the svOCT images. Figure 4.4D illustrates

the angiographic appearance of macula edema and the corresponding svOCT image provides valuable information about underlying capillary structure that is not perceivable on FA due to bad dye leakage. This case particularly illustrates the adjunctive and complementary role of svOCT to fluorescein angiography.

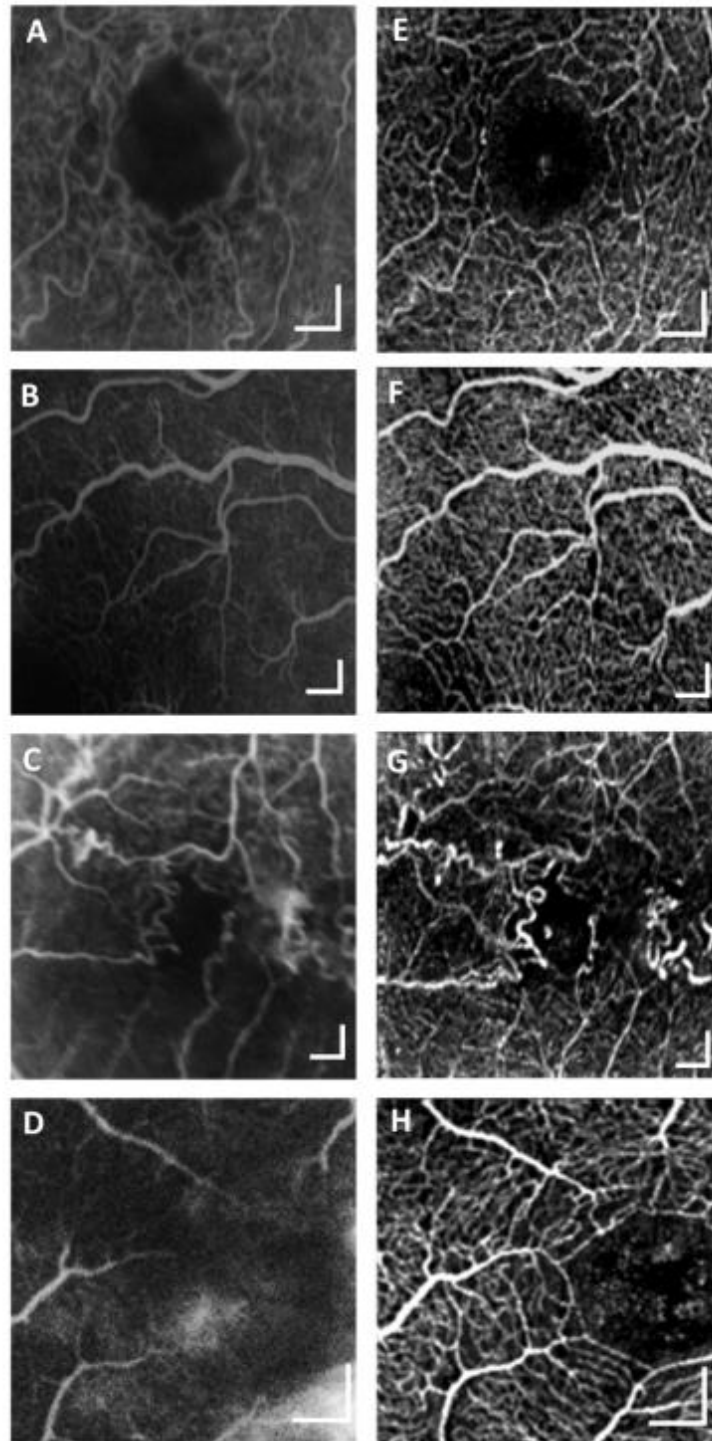


Figure 4.4. Comparison of FA (A-D) and corresponding svOCT (E-F) acquired from DR patients. (scale bar: 200 μ m)

A representative B-scan acquired from a patient with AMD is shown in Figure 4.5A. We used the graph cuts segmentation in post processing to select the region used for generating the *en-face* image. Unlike the FA image, which is a combination of both retina and choroid, the svOCT *en-face* image shown in Figure 4.5C extracts only the retinal vasculature, revealing much more capillaries compared with FA shown in Figure 4.5B.

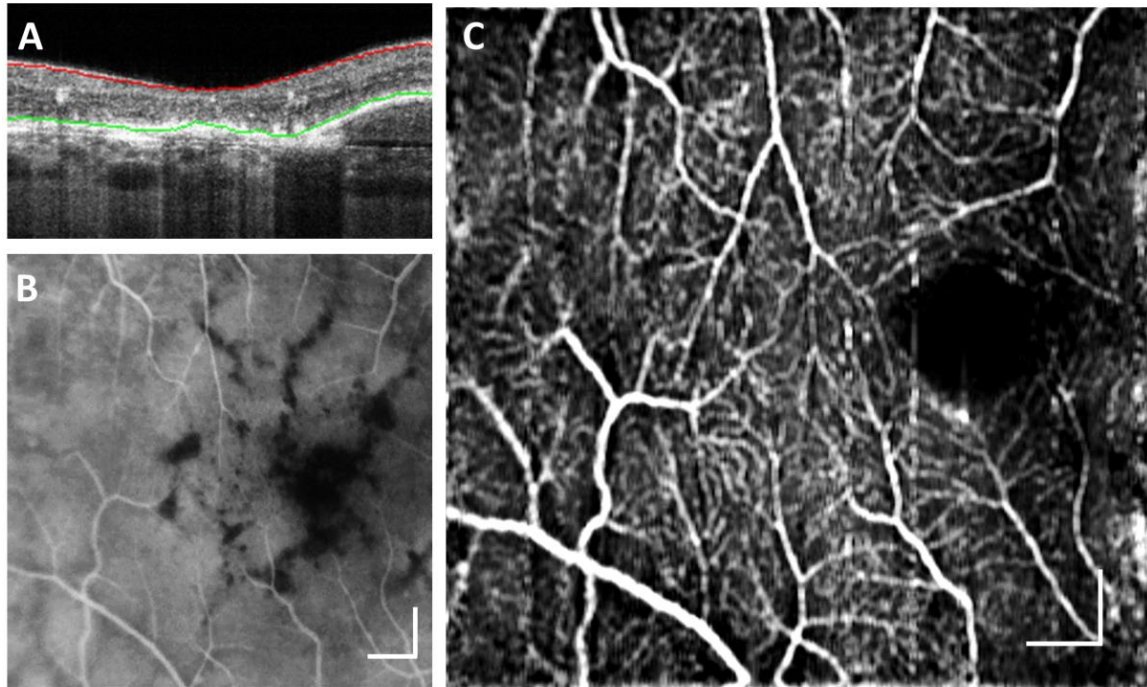


Figure 4.5. (A) Representative segmented Bscan; Comparison of FA (B) and svOCT (C) acquired from AMD patient. (scale bar: 400 μ m)

4.4. Discussion and conclusion

Capillary networks are inherently linked to retinal disease. This study highlights the utility of our prototype svOCT device for non-invasively studying the human retinal vasculature in real-time. The results presented in this chapter suggest that svOCT is complementary to FA, and may be superior in providing retinal capillary detail. Current limitations of svOCT technology include its inability to assess pooling/staining and low flow aneurysms. Previous work has shown that the anatomical information captured on FA is predominantly that of the inner most retinal capillary networks [71]. The *en-face*

images of distinct capillary networks illustrated in this report demonstrate that this device has the capability for providing information about all retinal capillary networks.

Speckle variance OCT also has the potential to non-invasively identify important pathological manifestations of diabetic retinopathy, ischemia and proliferation. In patients with compromised renal function, where the administration of fluorescein dye may be contraindicated, this device may be particularly advantageous. In this study we present images with a field of view ranging from $5 \times 5 \text{ mm}^2$ to $1 \times 1 \text{ mm}^2$. It is possible to acquire images with a wider field of view using a higher acquisition speed laser, hardware motion tracking and image mosaicking. Further quantitative work is required to define the role of svOCT in clinical practice.

The comparison between FA and svOCT presented in this Chapter is still descriptive, and not fully quantitative. In the next chapter, two quantitative clinical studies of human retinal capillary networks using svOCT are investigated and compared with histology. These studies were a result of collaboration with a group from the University of Western Australia.

Chapter 5.

Quantitative in vivo study of human retinal capillary networks using svOCT

The retina has one of the highest rates of aerobic metabolism among human tissues. The eye has an extensive blood supply to sustain the oxygen demands of the retina [74–77]. Retinal vessels are autoregulated to optimize blood supply to satisfy the metabolic needs of the retina. The blood supply to the retina consists of choroidal and retinal blood supply. Throughout the retina, the major blood vessels branch into a number of capillary networks that traverse the neural tissues. The organization of these capillary networks has been recently investigated by our collaborators from the University of Western Australia. Using donor eyes and injecting dye through the central retinal artery, they performed histological analysis of the microvasculature. Their histological analysis through confocal imaging showed variable morphometric characteristics such as capillary diameter and density between different vasculature networks may have important correlations with neuronal function [78,79].

Ongoing efforts are looking into investigating microvasculature in order to better understand diseases burden of vascular retina diseases such as DR and AMD. The retinal vessels are affected due to DR, and whereas AMD is related more to the choroidal vessels. Generally in the clinic, the retinal vessels can only be evaluated by clinical exam and FA which their role in imaging capillaries is unclear given difficulty in achieving consistent focus and obtaining images of both eyes in focus in the same sitting. The svOCT is ultimately a good option to look at the retinal vessels.

In this chapter, we demonstrate two different experiments to verify what we achieved from svOCT correlates with the histology studies that have been documented into a number of manuscripts in collaborative preparation for journal submission with our

collaborators. Each experiment focuses on different region of the retina. The first experiment is use svOCT to study the superior region of the retina. The second experiment is to assess the reliability of svOCT in obtaining radial peripapillary capillaries (RPCs) parameters.

5.1. Experiment #1

5.1.1. Materials and Methods

This study was approved by the human research ethics committees at The University of Western Australia and the Eye Care Center at Vancouver General Hospital / University of British Columbia. All live patient imaging was performed at the Eye Care Centre in Vancouver. All human tissue was handled according to the tenets of the Declaration of Helsinki.

Human Donor Eye

A total of 12 eyes from 10 human donors were used for histological study with confocal scanning laser microscopy. Donor eyes were acquired from the Lions Eye Bank (Lions Eye Institute, Western Australia). All human donor eyes used in this study had no known history of ocular disease. The methodology used for targeted endothelial labelling of retinal capillary networks was reported in [79,80]. Images were captured from the retinal eccentricity that was located 3mm superior to the optic disc. Two Nikon C1 microscopes were used for confocal imaging.

In vivo svOCT imaging of Human Subjects

A total of 14 eyes acquired from 7 human volunteers were involved for svOCT imaging. The demographic details of human subjects are presented in Table 5.1. The retinal region that was imaged by svOCT was ~3mm superior to the optic disc, evaluated based on real-time volumetric OCT images. For speckle variance calculation, three repeated acquisitions at each B-scan location were acquired. The scan area was sampled in a 300x300(x3) grid with a ~1x1 mm field of view in 3.15 seconds. The svOCT images were processed using the GPU-accelerated program. The retinal layers were

automatically segmented using a 3D Graph Cut based segmentation tool implemented in MATLAB [33]. The *en-face* visualizations of the retinal microvasculature were generated by summing the svOCT data along the depth direction within each segmented retinal layer. Scan dimensions were calibrated based on the eye length of each participant, measured using the Zeiss IOL Master 500.

Table 5.1. Demographic Details: Age, Sex, Eye, Date of Imaging of Patients for svOCT imaging.

svOCT Patient ID	Age	Sex	Eye	Date of Imaging
K	36	M	L + R	2014/05/25
L	35	M	L + R	2014/05/27
M	28	M	L + R	2014/05/27
N	29	M	L + R	2014/06/01
O	31	M	L + R	2014/06/01
P	59	M	L + R	2014/06/18
Q	60	F	L + R	2014/06/18

Segmentation of Capillary Networks

Four different capillary networks in the retinal eccentricity located 3 mm superior to the human optic disk were studied. These networks are located in: (1) NFL; (2) GCL; (3) border of IPL and superficial boundary of the INL; and (4) boundary of deep INL and OPL. Both histological sections and *en-face* svOCT images were prepared for these four retinal layers. This permitted direct comparison between these two imaging modalities. Figure 5.1 shows the representative transverse histological specimen and OCT B-scan acquired from the same eccentricity of the eye.

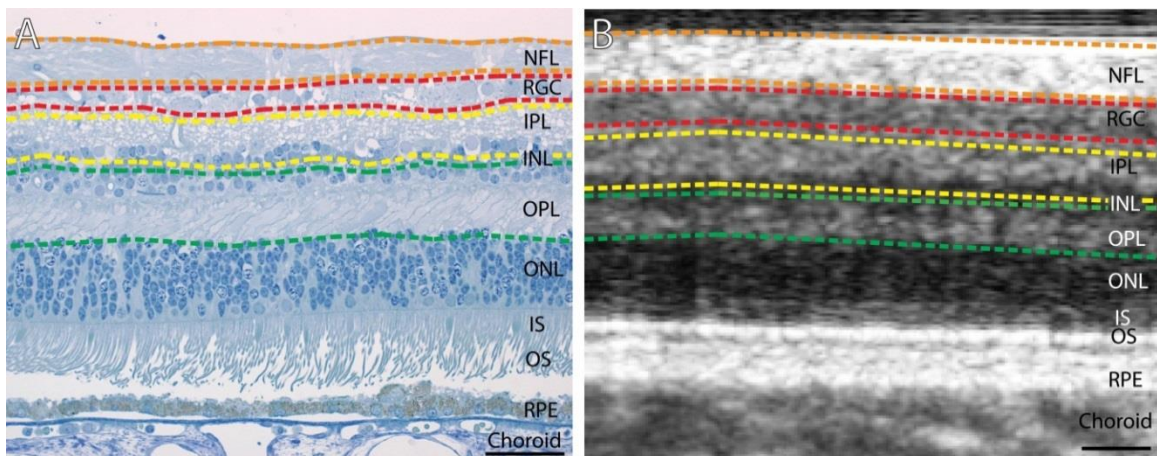


Figure 5.1. Regions of the retina in the capillary study. Transverse retinal section (A) and B-scan image (B) from healthy subjects demonstrate the histological and svOCT features respectively, at the studied region 3mm superior to the optic disc. Layers are colour coded: Layer 1 (orange) = Nerve Fibre Layer (NFL), Layer 2 (red) = Retinal Ganglion Cell layer (RGC), Layer 3 (yellow) = border of Inner Plexiform Layer and superficial Inner Nuclear Layer (IPL/sINL), Layer 4 (green) = border of deep Inner Nuclear Layer and Outer Plexiform Layer (dINL/OPL). ONL, outer nuclear layer; IS, inner-segment of photoreceptors; OS outer-segment of photoreceptors; RPE, retinal pigment epithelium. Scale bar = 50 μ m.

5.1.2. Results

The mean donor age of the control histology group was 45.58 ± 5.30 years, taken from nine left and three right eyes of one female and nine male donors. The average post-mortem time before eyes were perfused was 14.80 ± 1.68 hours. The mean age of the svOCT group was 39.71 ± 3.68 years, taken from 14 eyes from one female and six male patients. There was no statistical significant difference in an age between the two groups ($P > 0.05$).

Capillary Network Topography in svOCT and Confocal Images

Figure 5.2 illustrates the morphological appearance of the four capillary networks in both histological confocal images and svOCT images. As noted in our collaborator's previous work [78], Figure 5.2A is the capillary network within NFL which runs parallel to the RGC axon bundles in a linear path. Figure 5.2B is the capillary network which arises

from the retinal arterioles in the RGC layer. The IPL/sINL capillary network in Figure 5.2C was three-dimensional in structure and had a similar density to the NFL capillary network. The deepest network is located at the level of the dINL/OPL, and is the most easily distinguishable layer in both imaging modalities. This layer was observed to have multiple closed loops and be laminar in structure, shown in Figure 5.2D.

Comparing the results with the histology and svOCT modalities, there are some similarities noted as follows: (1) All four capillary networks in the svOCT images appeared to be morphologically similar when compared to their histological counterparts. (2) All svOCT capillary diameters were very similar when compared to their corresponding histology diameters, except for the RGC network. (3) The RGC layer densities were similar between the modalities.

There are some differences observed between the two modalities that are: (1) Besides the RGC layer, all other capillary networks in the svOCT images had higher density indices than their histology counterparts. (2) Diameters in the RGC layer were larger in the svOCT modality compared to histology. (3) The svOCT images generally had more 'background noise' compared to histology images.

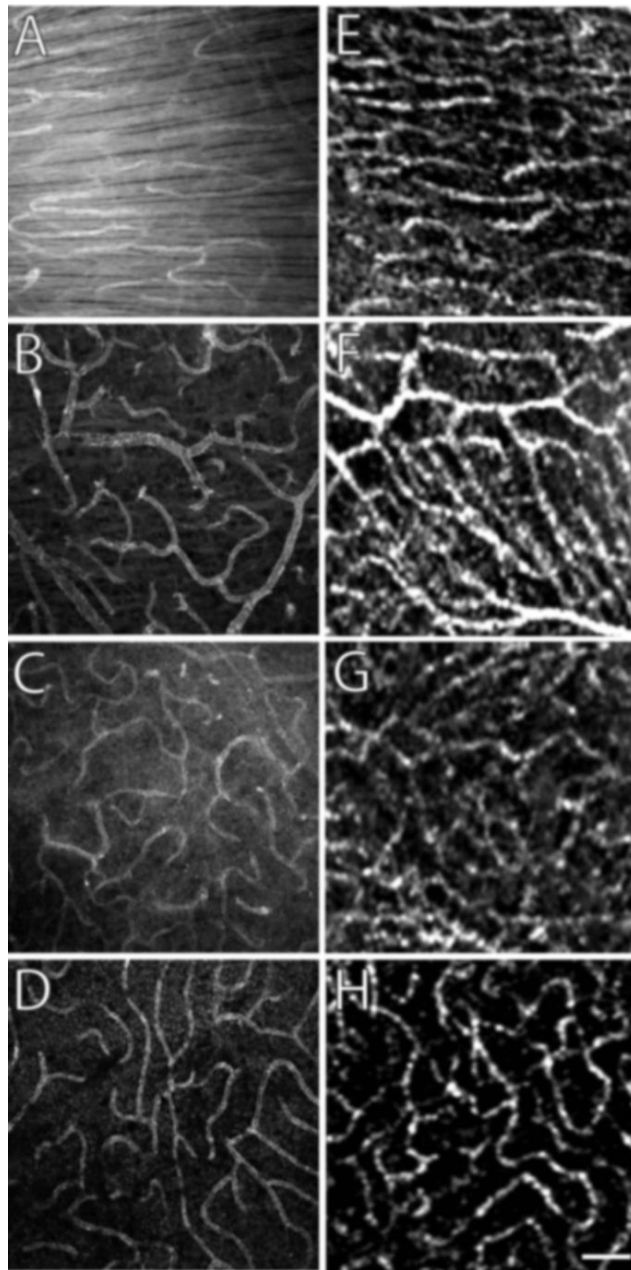


Figure 5.2. Comparison of the capillary network in histology and svOCT eyes at 3mm superior to the optic disc. (A) to (D) = Whole-mount histological confocal images of the normal human retinal vasculature in histology control eyes. (E) to (H) = svOCT images of the capillary networks in living patients. (A) and (E) represent the NFL, (B) and (F) the RGC layer, (C) and (G) the IPL/sINL layer, and (D) and (H) the dINL/OPL layer. Scale bar = 100 μ m.

Quantitative Analysis

The quantitative analysis of capillary diameter and capillary density in Figure 5.3 were performed by our collaborators, and the results are shown in Figure 5.4.

Within the histology images, capillary diameters were significantly different between all networks. Within the svOCT images, capillary diameters were significantly different between all networks except the NFL and IPL/sINL network. The quantitative comparisons between histology and svOCT data revealed no significant difference in capillary diameter in the NFL network, IPL/sINL network, but a significant difference at the RGC network.

The capillary density was performed by calculating the number of vessel intersections and vessels per 100 μm . Within histology images, the capillary density was significantly different between all networks except between NFL and IPL/sINL network and RGC and dINL/OPL network. Within the svOCT images, these capillary density indices were also significantly different between all networks except between NFL and IPL/sINL networks. The comparisons between svOCT and histology images demonstrated no differences in the RGC network for these indices. For the remaining capillary networks there were significant differences between svOCT and histology images for all of these indices.

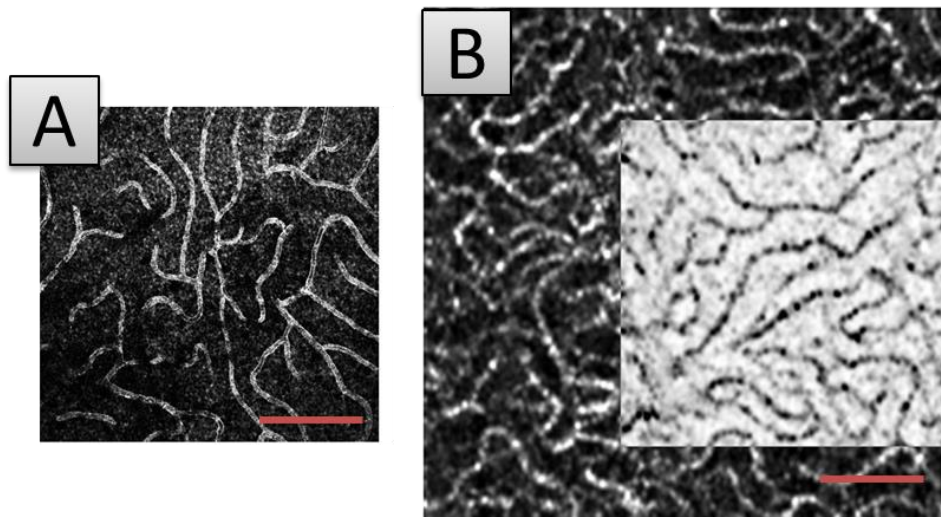


Figure 5.3. Quantification of capillary diameter and density in histology and svOCT eyes. (A) Captured histological retinal layer (dINL/OPL) with confocal microscopy in an unaltered state. (B) The svOCT image shown has been captured with the svOCT machine. A region of $636.5\mu\text{m}^2$ area is marked out and inverted to allow the same area quantified as the histology control images. Scale bar = $200\mu\text{m}$.

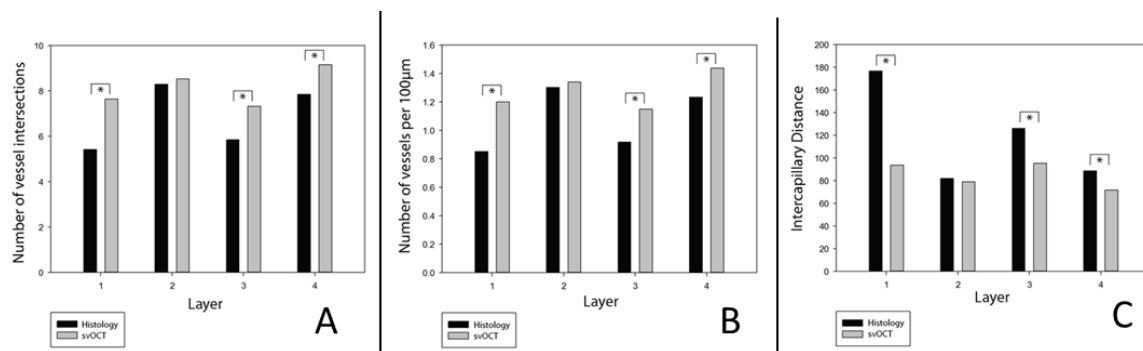


Figure 5.4. Graphs showing individual retinal layers against three different density indices – (A) the number of vessel intersections, (B) the number of vessels per $100\mu\text{m}$, and (C) the intercapillary distance. Comparison between the individual layers in the histological control eyes versus the svOCT eyes, revealed only the RGC layer was similar in all density indices ($P > 0.050$). All other comparisons differed significantly ($P < 0.050$), and are indicated by the asterisk (*). (Figure generated by collaborators)

5.2. Experiment #2:

5.2.1. Materials and Methods

This study was approved by the human research ethics committees at The University of Western Australia and the Eye Care Centre at Vancouver General Hospital. All live patient imaging was performed at the Eye Care Centre in Vancouver.

Confocal images from human donor eyes

The retinal microvasculature of 9 retinas from 9 donors aged between 15 and 75 were labeled using perfusion labeling technique as described in [79,80]. Confocal image stacks were obtained from the superior (S), supero-temporal (ST), temporal (T), infero-temporal (IT), inferior (I) and nasal (N) regions, with the field of view centered on the 500 μm mark from the optic disc edge. The field of view measures 636.5 μm^2 . Optical slices encompassing the NFL were included for projection of RPCs contained in this layer as a 2D image.

svOCT images from live subjects

A total of 16 retinas from nine healthy volunteers, aged between 28 and 60 were imaged, and six regions within 1mm from the optic disc edge in the supero-nasal (SN), supero-temporal (ST), temporal (T), infero-temporal (IT), inferior-nasal (IN) and nasal(N) sector were imaged, and the *en-face* view of the NFL was extracted as shown in Figure 5.5. The linear dimension of the scan area ranged between 942 μm and 1050 μm due to differences in the eye length of the individuals as measured using the Zeiss IOL Master 500. The boundaries for the different retinal layers were determined manually on the OCT B-scans and the segmentation was performed on the corresponding volumetric scans to generate the enface view for the NFL.

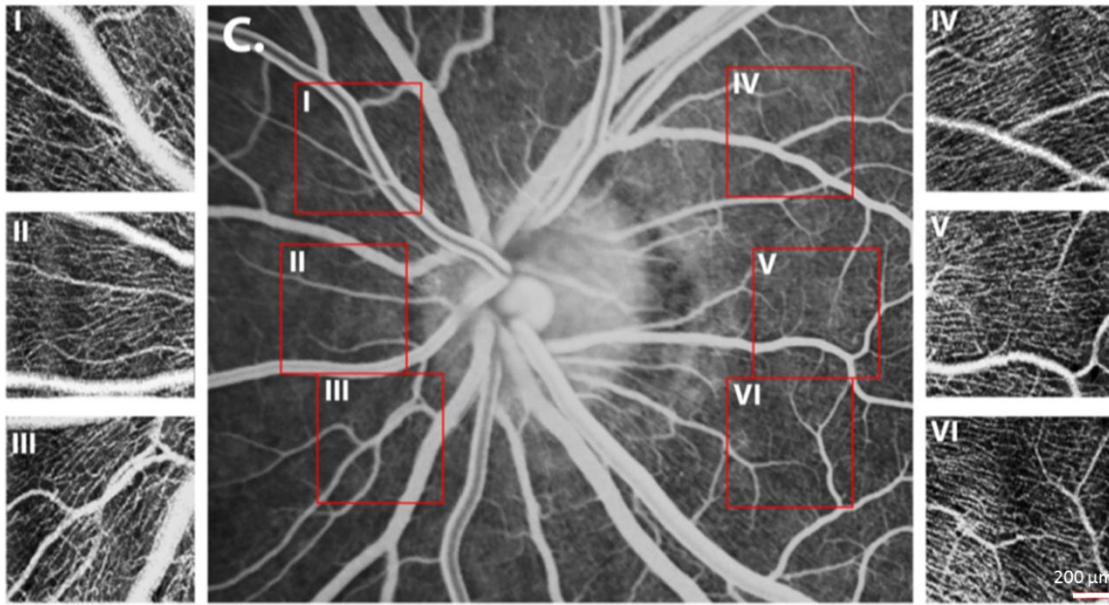


Figure 5.5. A representative FA image a healthy volunteer showing the six corresponding study regions acquired using svOCT.

5.2.2. Results

The average age was 42.7 ± 4.73 years for the 9 live subjects and 40.9 ± 7.62 years for the 9 donors. There was no statistical significant difference in age between the two groups. The svOCT images from the retinal NFL closely resemble the distribution pattern of RPCs observed using fluorescent angiography as shown in Figure 5.6.

The quantitative analysis of vessel density was performed by our collaborators. The density measurement was comparable using the two techniques and was consistently, though not significantly higher, when measured using svOCT images. The nasal region is the only exception where higher vessel density has been recorded using svOCT technique with statistical significance. Both techniques showed the greatest density of RPCs to be located in ST and IT regions. In svOCT images, the RPCs density is significantly higher in the ST than that of the inferior and superior quadrants; however, a significant statistical difference was not found in the confocal histology images.

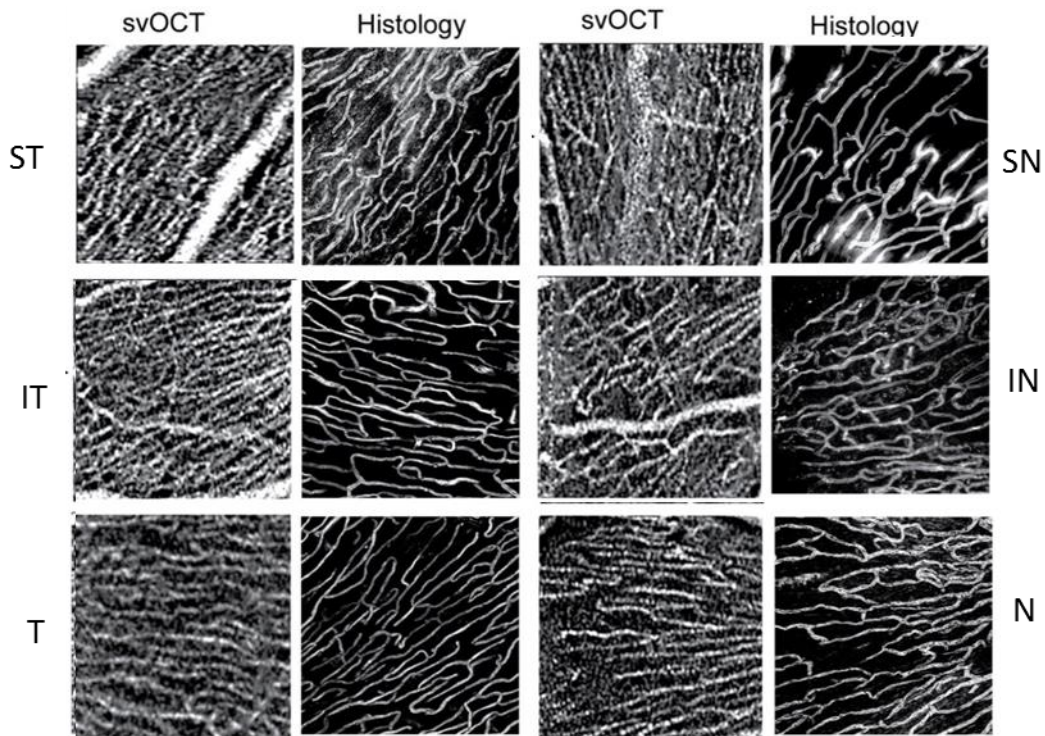


Figure 5.6. svOCT and histology images for each location.

For the intercapillary distance measurement, both techniques demonstrated the smallest intercapillary distance at the ST and IT regions. There is no significant difference in most of other regions compared except the temporal region showed comparatively smaller intercapillary distance using the svOCT technique.

RPCs diameter measurements were consistently and significantly larger in the svOCT images when compared with confocal images. Comparison between the regions using svOCT found superior regions to have significantly smaller RPCs diameter measurements. Comparison between regions using confocal histological technique found temporal RPCs to be significantly smaller than all the other regions, and that the nasal RPCs to be significantly larger than all other regions.

5.3. Discussion

From these studies, the svOCT imaging appears to be a reliable technique and useful for density measurement in live human retinal imaging whereas histology is only

useful for *ex vivo*. Although the svOCT technique is reliable to provide flow information, it is not reliable for dimension measurement due to limitation of resolution. Also, the differences in diameter measurements could be attributed by several variables such as live tissue (svOCT) versus fixed tissue (histology) and the greater age range of the donor group. Another limitation of svOCT is the shadow artifact created below relatively large vessels especially in the NFL, and the vascular information for the layers beneath NFL such as GCL and IPL can be less accurate. From these two experiments, we can see that the svOCT is suitable for investigating changes in retinal vasculature in retinal diseases such as DR.

Chapter 6.

GPU implementation with Segmentation in real time

The work presented in the previous chapter utilized a graph-cut based image segmentation that was applied in post-processing with MATLAB. In this Chapter, an implementation of a GPU accelerated Graph Cut algorithm is presented that can be used for retinal layer segmentation to enhance the visualization of vasculature networks from distinct retinal capillary beds during acquisition, also generate the thickness map of the entire retina.

6.1. Introduction

Real-time OCT imaging provides instant visualization of the retinal structure in both cross-sectional and volumetric views. With svOCT, we also demonstrated the real-time visualization of vasculature networks. However, only qualitative images were shown in real-time; detailed quantitative analyses were usually performed offline. Retinal layer segmentation is one of the most important and also the most time consuming processing step for many forms of data analysis such as retinal layer thickness measurements. Similarly, for the case of svOCT imaging, the segmentation allows the visualization of vasculature networks from each targeted retinal layer.

In the previous chapters of this thesis, we performed real-time retina depth selection using straight lines. Figure 6.1 shows an example of B-scans of a healthy retina and diseased retina with two red lines to select retinal layers of interest. The overall retinal curvature in Figure 6.1A is relatively flat, and the information within the red lines is a good representation of a combination of NFL, GCL and IPL. In our real-time GPU program, for volumes of healthy retinas that don't contain large motion artifacts, this naïve layer selection is sufficient to select the specific retinal layers of interest.

However, as shown in Figure 6.1B, a more sophisticated segmentation approach is needed to extract the retinal shape for diseased retinas.

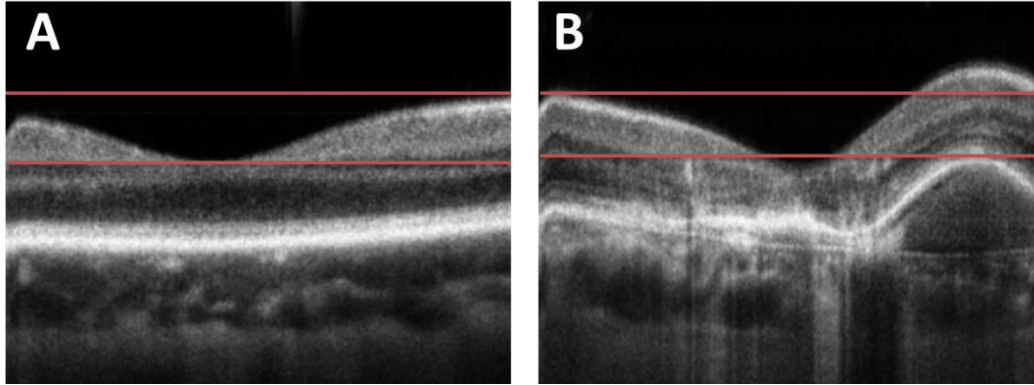


Figure 6.1. An example of B-scans of a healthy retina (A) and diseased retina (B) with two red lines to select retinal layers of interest.

There have been various methods of retinal layer segmentation reported in the literature. The method used in all the clinical studies presented in this thesis was from Lee et al [33], which is based on a 3D Graph Cut based segmentation [81]. This algorithm was implemented in MATLAB, and required ~40 minutes to segment 3 retinal layer boundaries in a ~500MB OCT volume if using a high performance computer. The low throughput of the MATLAB program makes it difficult for use in clinical studies, where hundreds of volumes have to be segmented. This motivated us to implement segmentation onto our GPU accelerated program to achieve svOCT *en-face* images from different retinal capillary beds in only a few seconds. This work is a continuation of preliminary work based on the bachelor thesis from a former member in the lab [82].

6.2. Methods

The NVIDIA Performance Primitive (NPP) library was used in the GPU-based segmentation implementation. This library provides many image processing functions, such as morphological operations. We utilized a pre-developed technique called the Graph Cut (GC) solver for 2D images which is based on the Goldberg-Tarjan Push-Relabel (GT PR) algorithm [[83,84]. The advantage of using this algorithm is that only one pixel (node) is considered at a time and only directly connected pixel values are

used for processing during execution. Therefore, it is well suited for parallelization in a GPU-based implementation.

The GC processing steps to achieve the layer segmentation include the following: (1) Use a bilateral filter on an averaged intensity B-scan image to remove the speckle noise prior to segmentation; (2) Use NPP GC to output a binary label result of the image; (3) Use NPP image erosion and dilation to remove extra noise in the binary output; (4) Use a Connected Component Labeling (CCL) approach to extract the two largest connected components from the binary image; and (5) Locate the indices to identify the ILM and BM layers. A demonstration of these processing steps is presented in Figure 6.2. In the first step, a bilateral filter was chosen to remove the speckle noise because it had a short execution time on the GPU. If resources permit, other edge-preserving speckle noise filtering algorithms, such as Boundary-Value (BV) smoothing, [85] may further improve the segmentation results.

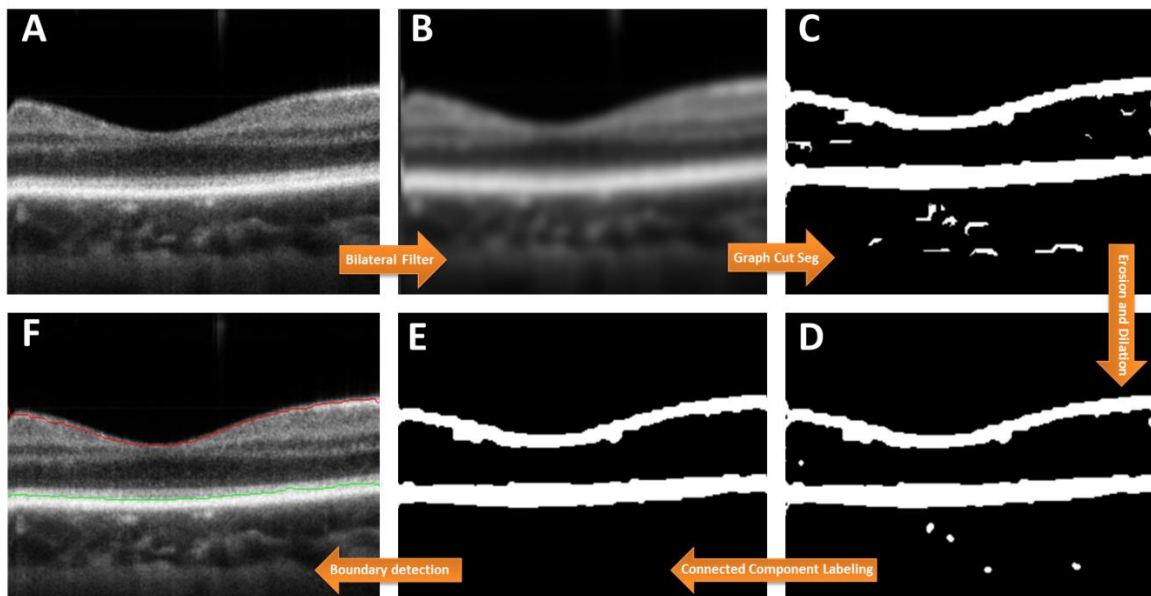


Figure 6.2. Flow chart for the GPU based GC of a representative B-scan of a healthy retina (A), and then after Bilateral Filtering (B), Graph Cut segmentation (C), erosion and dilation (D), Connected Component Labeling (E) and layer boundary detection (F). ILM (red) / BM (green)

Our svOCT imaging system took 3.15s to acquire a volume that contained a total of 300x3 B-scans (3 B-scans acquired at each lateral location and a total of 300 different locations). The segmentation process took ~80ms per B-scan with a B-scan size of 300 by 256 (lateral by axial). For a volume of 300 frames, the segmentation process required ~24s to segment all the B-scans, which is insufficient for achieving real-time visualization with an acquisition time of less than 3 seconds per volume. Therefore, in order to improve the processing time to match the acquisition time, a sparse B-scan GC segmentation approach was implemented. The axial size of the B-scan was already cropped to the minimum required to contain the retina. One option would be to downsample the number of A-scans per B-scan, and the other option is to downsample the number of B-scans in a volume. The latter option that was implemented, relying on minimal lateral changes in the retina laterally, and leveraging the batch processing already implemented in the GPU processing. For every batch of 30 B-scans (10 B-scan positions), images were averaged, bilateral filtered, and segmented. The averaging step was effective for eliminating speckle noise, and was more effective in preserving the overall shape of the retina than bilateral filtering alone. After performing GC segmentation to delineate the ILM and BM positions on each batch, linear interpolation was used to estimate the indices of the ILM and BM for the rest of the B-scan frames in the volume. This method works very well when there is no significant motion artifacts involved. The thickness of the entire retina was calculated by subtracting the indices of ILM and BM, and the colour coded thickness map was displayed in real-time. The overall processing rate for segmenting the whole volume was up to ~125 kHz per A-scan which is still beyond the acquisition rate (100 kHz) of the prototype clinical system.

The GPU GC segmentation was not only used to generate the *en-face* vascular images from the entire retina, but also for different retinal layers. However, due to the low intensity difference between certain retinal layers such as the GCL and IPL, our automated GC segmentation could not delineate them well. In the previous chapter, we proposed a semi-automated approach to generate the *en-face* images from different retinal layers, based on the characteristic that the general curvature of the BM, IPL and OPL is relatively uniform in healthy retinas. The semi-automated intra-retinal layer segmentation process consisted of the following three steps:

1. Use 2D GC segmentation (GPU) to identify the ILM and BM
2. Manually apply an offset from the BM's segmented result to estimate the boundary of IPL and OPL layer based on the real time B-scan images.
3. Generate *en-face* images with the segmented regions.

The steps outlined above provide a significant improvement in the visibility of layers during acquisition for real-time assessment. Automated intra-retinal segmentation could be performed in post-processing, where real-time performance is not critical.

6.3. Results

Our workstation for performing GC segmentation consisted of dual Xeon E5-2620 CPUs, 64 GB of RAM, and a Quadro K6000 GPU. For software development, we used Microsoft Visual C++ 2012 on a 64 bit Windows 7 operating system and CUDA Toolkit version 5.5 for programming the GPU. Figure 6.3 is a profiler image demonstrating a single batch processing iteration in the GPU software. In this figure, we demonstrate the implementation of the Swept-Source based svOCT, where the entire processing consists of (A) OCT processing pipeline; (B) GC segmentation; and (C) svOCT processing, generating *en-face* images, and display. The overall processing for a single batch takes an average of ~80 ms. The acquisition time for a single batch is ~90 ms, which is longer than the entire processing.

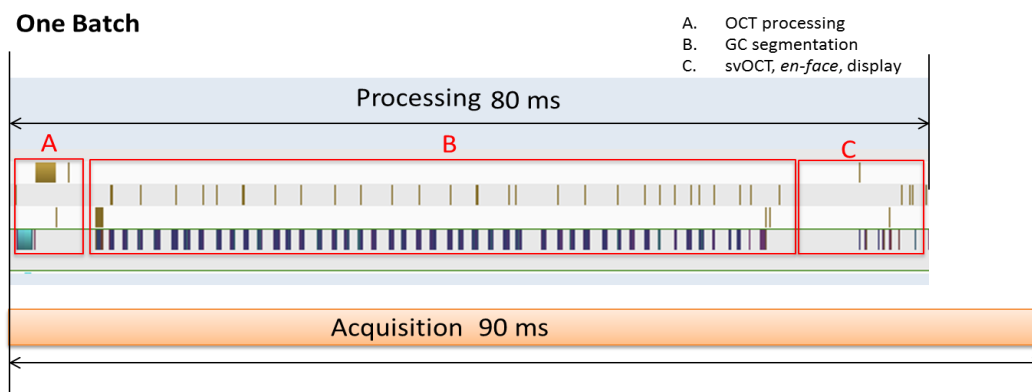


Figure 6.3. CUDA processing pipeline captured using the NVIDIA Visual Profiler

Preliminary results for svOCT visualization are presented in Figure 6.4-Figure 6.6. Figure 6.4 compares the *en-face* images generated from the naïve segmentation with the GPU GC segmentation. In Figure 6.4a, b, and c, three different depth selections are indicated using straight red lines. The *en-face* images were generated by summing all the pixels within the selected depth region along the A-scans as shown in Figure 6.4A, B, and C, respectively. In the B-scans, the retina had a tilted orientation in comparison to the selected region, which made it challenging to capture *en-face* images of the local vasculature networks from specific retinal layers. For example, in Figure 6.4A, the retinal vessels are washed out because of the brightness from the choroid. In Figure 6.4B, the region on the top right is relatively dark compared with the region in the bottom, as fewer samples were selected on the left side of the B-scan, as shown in Figure 6.4b, due to the tilt of the retina. Also, body/eye motion during acquisition can ultimately shift the position of the retinal layers along the slow scan, which can lead to artifacts, as indicated by the arrows. In Figure 6.4d, GC segmentation results of ILM and BM are displayed as red and green lines, respectively. The *en-face* image was generated by summing all the pixels along the A-scan within the segmented region of the entire volume, which is shown in Figure 6.4D. Compared to the *en-face* images from the naïve segmentation (Figure 6.4A-C), the image generated from the GC segmentation looks clearer and the vessels are much more defined and visible.

Figure 6.5 shows the *en-face* images before and after GC segmentation. This data was acquired from a DR patient with a large field of view ($4 \times 4 \text{ mm}^2$). After segmentation, the contrast between vessels and the background increases and also, more details can be seen, as indicated by arrows.

Figure 6.6 compares the superimposed images of two *en-face* images with two different retinal layers. Figure 6.6A was a representative B-scan with two selected regions by the straight lines a, b and c. Two *en-face* images shown in Figure 6.6B and C were generated from the region a-b, and b-c respectively; the superimposed image of these two is shown as Figure 6.6D. In Figure 6.6E, the red line (a) was the segmented ILM layer, and the green lines (b and c) were delineated by applying offsets to the BM layer that was segmented by the GC algorithm. As a result, Figure 6.6F showed the capillary network from the superficial layer where as Figure 6.6G from the OPL layer.

The superimposed image in Figure 6.6H reveals more information comparing to Figure 6.6D, as the colours represent layer-specific vasculature networks.

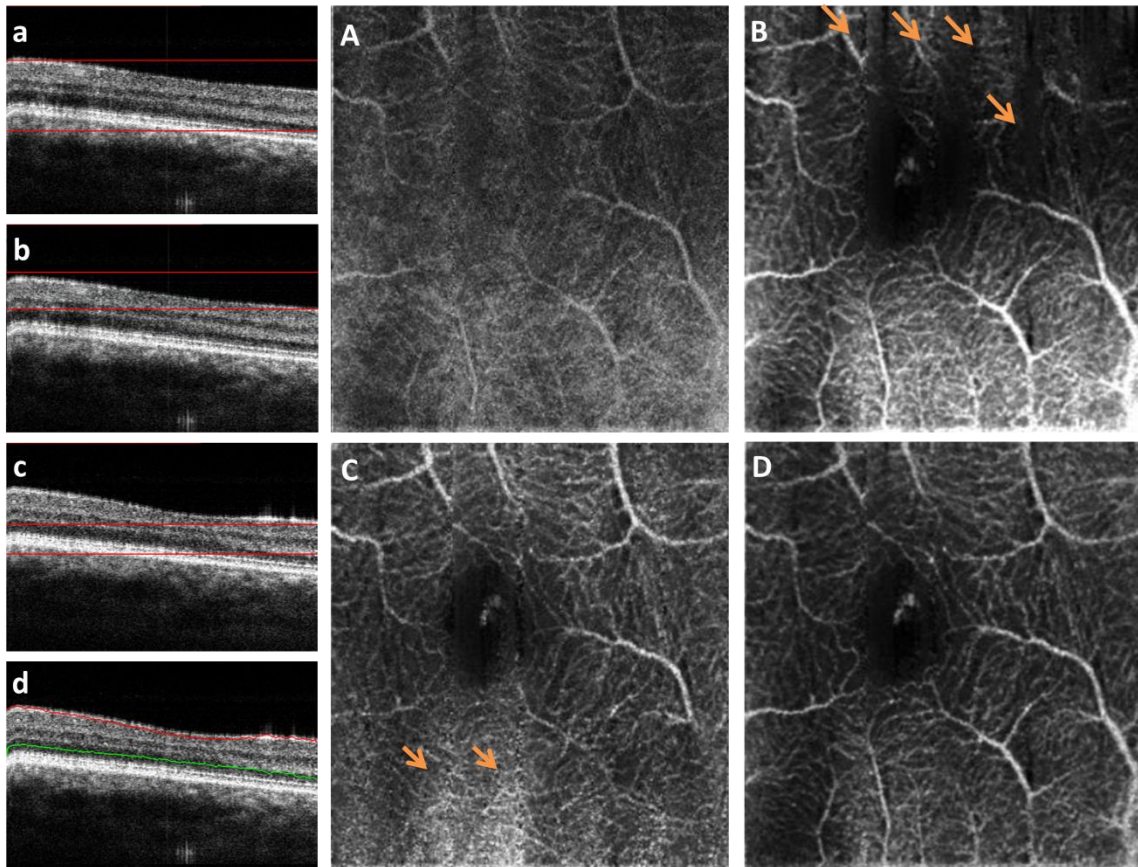


Figure 6.4. Representative B-scans with different region selection by straight lines (a-c) and GC segmented ILM (red) and BM (green) (d), and the corresponding *en-face* images (A-D). The arrows indicate the motion artifacts that decrease the image quality.

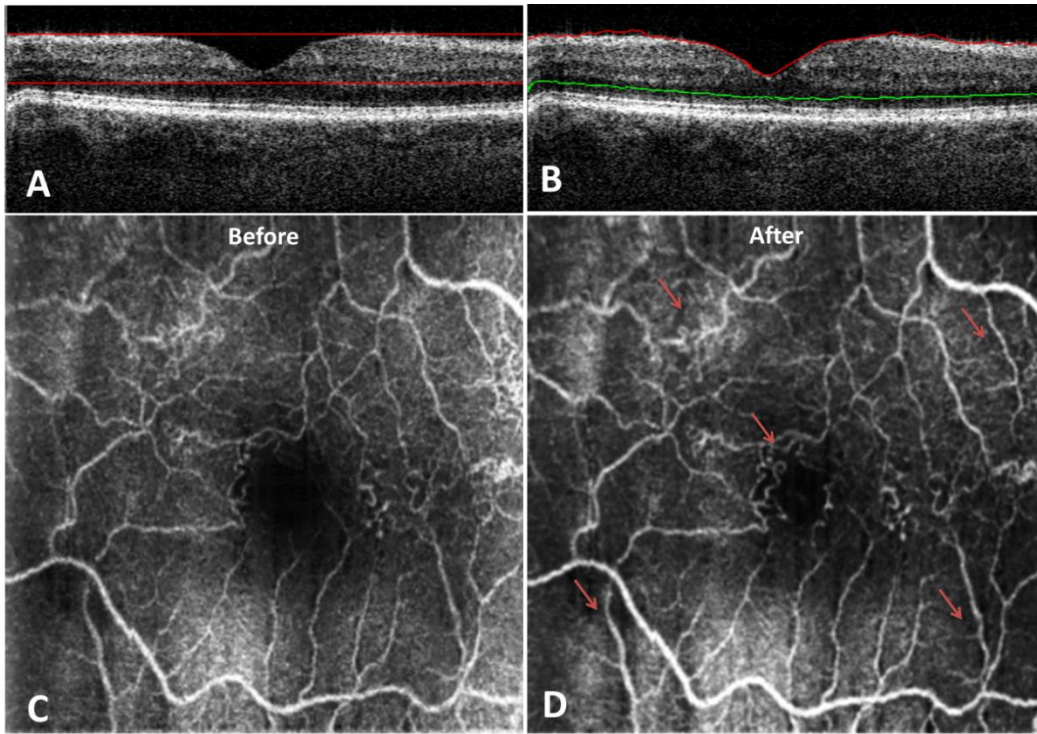


Figure 6.5. Representative B-scans and *en-face* images of a DR patient before and after GC segmentation.

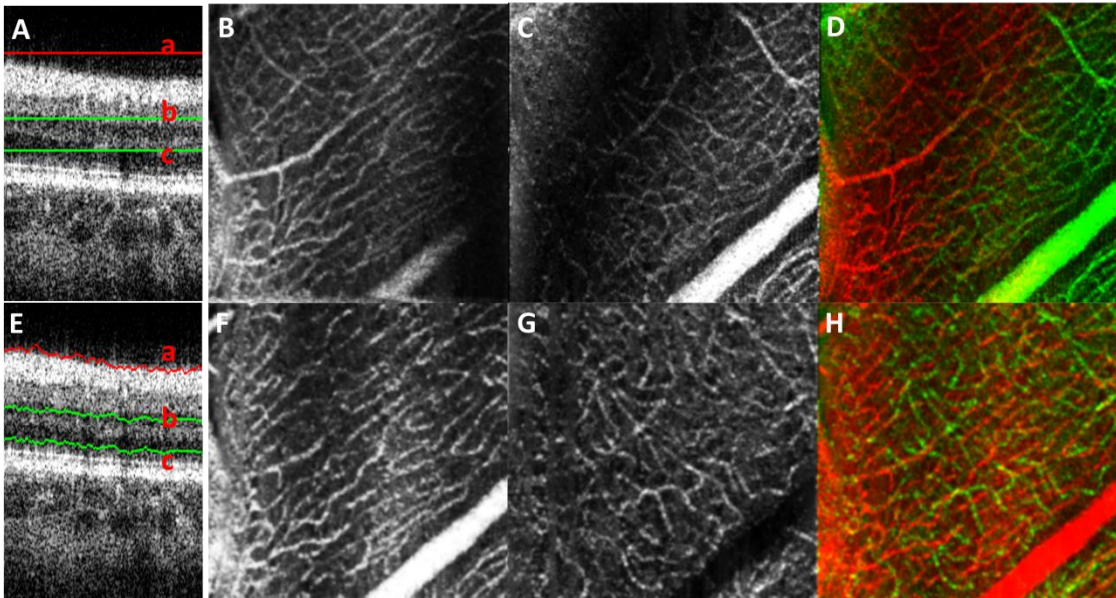


Figure 6.6. *En-face* images generated from different selected region by the naïve approach (A-D) and GC segmentation (E-H).

Currently, the GC segmentation approach was implemented in a way that was specifically applied on the fovea region. We also tried applying the segmentation on the retina with diseases such as DR and AMD to test the performance of the GC segmentation. The volumes with good image quality were selected, such that the brightness of the B-scans was reasonable and the RPE layer was not degenerated (as in geographic atrophy). If the RPE layer was missing more light would penetrate into the choroid, which would result in a very bright boundary at the choroid region in the B-scan, and affected the ability of the GC segmentation to detect the BM layer. Four representative B-scans with GC segmentation results are shown in Figure 6.7. We can see with the deformation of the pathological changes, the GC segmentation was sufficient to delineate the top ILM layer as well as BM layer.

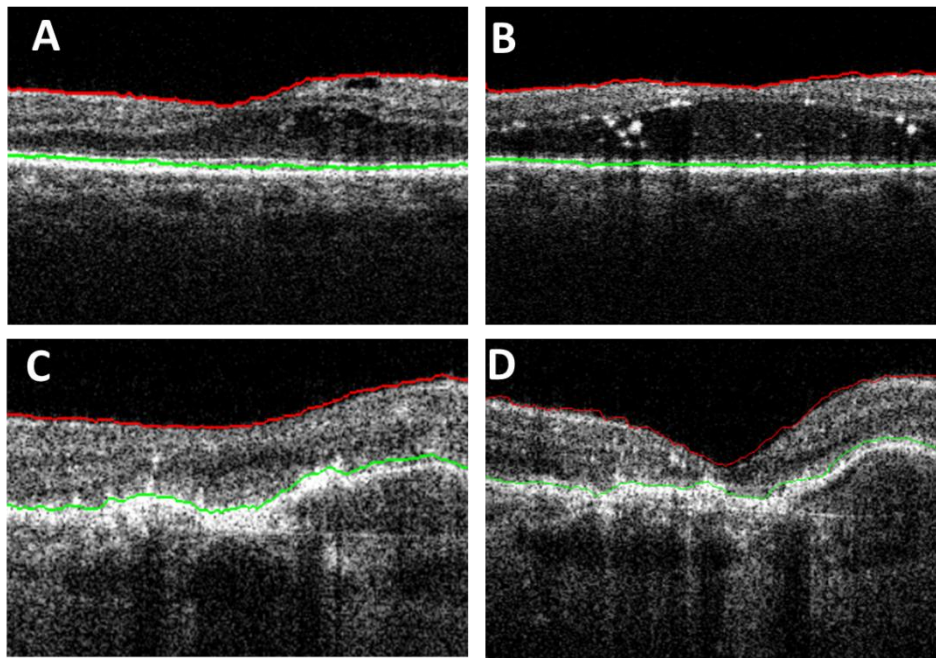


Figure 6.7. Segmentation results on retinas with pathological changes.

With the segmentation results of ILM and BM layers, we could also calculate the difference between these two layers to generate the thickness map of the entire retina, and display in real-time during acquisition. Figure 6.8 demonstrates an example between a healthy and a diseased retina. Figure 6.8A is a representative B-scan acquired from a healthy subject, and the thickness map generated has an expected rotationally symmetric thickness distribution from the fovea dip to the surrounding macular tissue. The thickness of the entire retina at the fovea dip is $\sim 70 \mu\text{m}$, and the retina gets thicker

closer to the edge of the image as shown in Figure 6.8C. Figure 6.8B is an representative B-scan acquired from a DR patient. The overall retinal thickness was thinner in Figure 6.8D compared with Figure 6.8C due to the retinal degeneration. The circled area indicates the retinal layer thickness thickening possibly due to the deposits (bright circular structures) and vessel growth that leads to retinal thickening in that area as shown in Figure 6.8D. Another comparison between three separate volumes acquired from three different eyes is presented in Figure 6.9. Figure 6.9C was acquired from a patient who has macular disease, and the thickness of the entire retina is much thicker due to the accumulation of fluid within the retina.

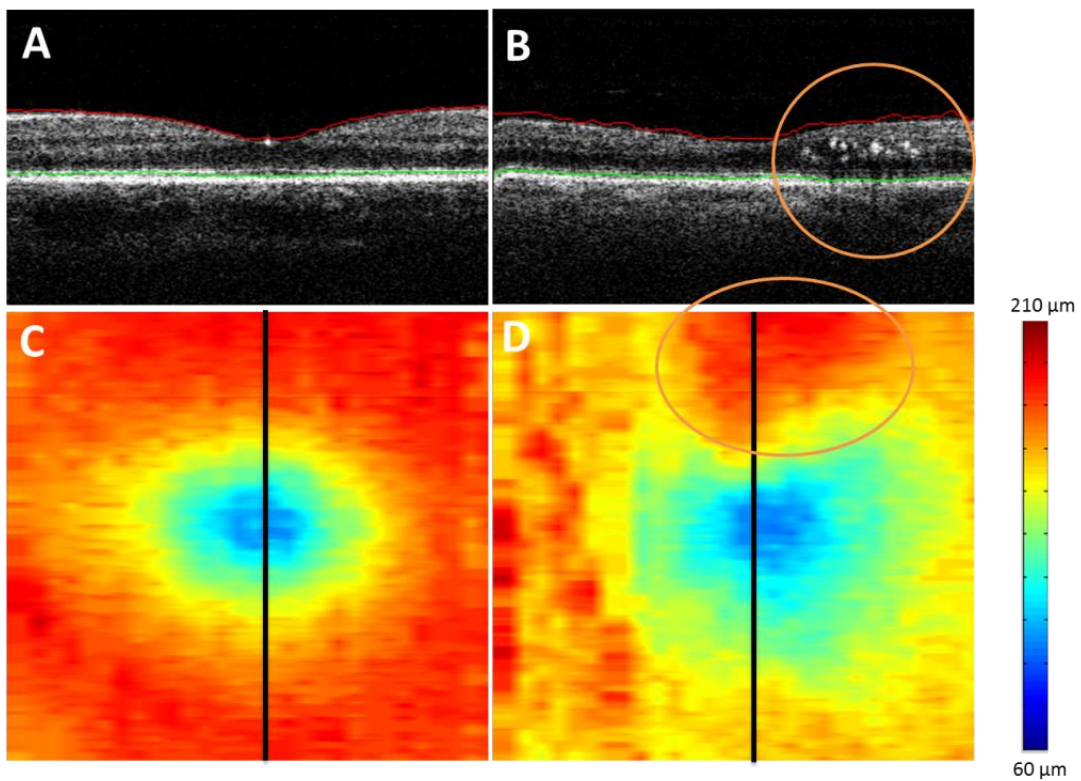


Figure 6.8. Representative B-scans A (healthy) and B (diseased) taken from locations indicated by the black vertical lines in the thickness maps C and D, respectively. The overall retinal thickness is thinning in D compared with C due to the retinal degeneration. The circled area indicates the retinal layer thickness thickening possibly due to the newly deposits and vessels growth. Field of view ($2 \times 2 \text{ mm}^2$)

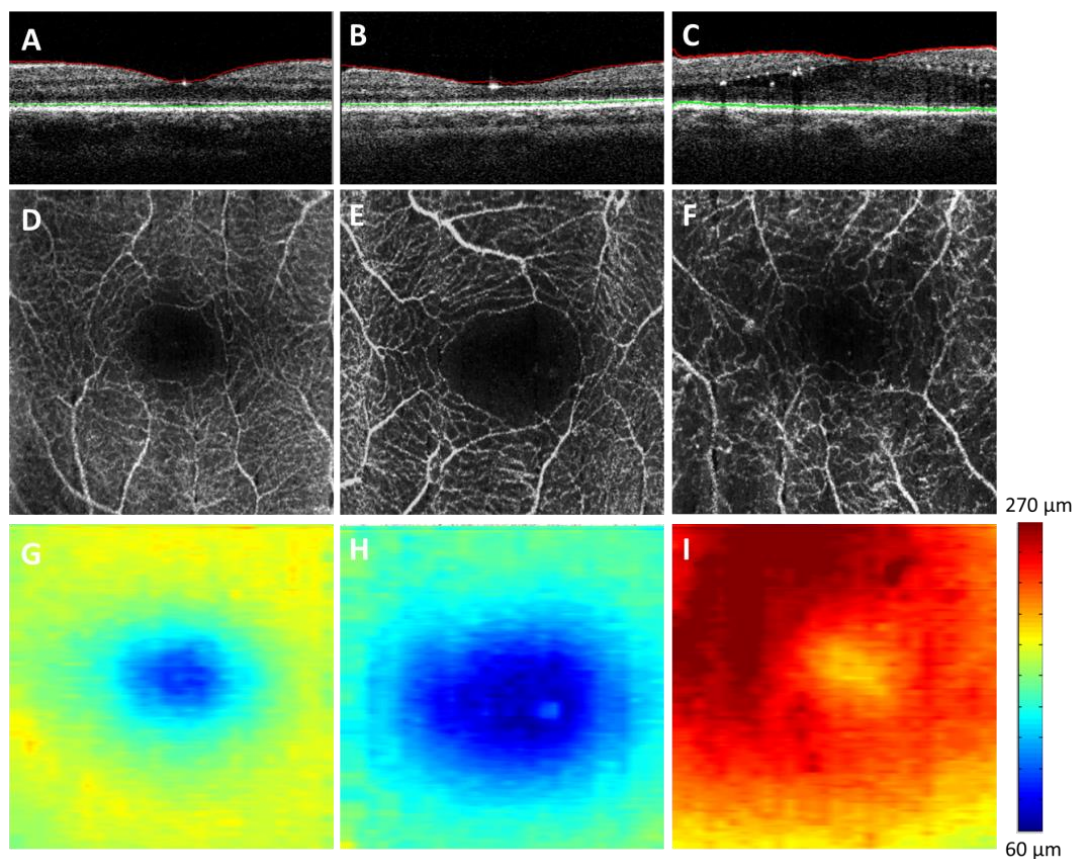


Figure 6.9. Comparisons of (A-C) B-scans, (D-F) svOCT *en-face* images, and (G-I) thickness maps among three different subjects. Field of view ($2 \times 2 \text{ mm}^2$)

6.4. Summary

In this chapter, a preliminary 2D GC segmentation approach was implemented in real-time to enhance the visualization of blood vessels within the entire retina as well as from different vascular beds, and also to display the thickness map for the entire retina. The overall processing and segmentation pipeline can be completed in a time as short as 2.2 seconds, which matches the acquisition rate of 3.15 seconds per volume for the 1060 nm system at the ECC. This is sufficient to reach the goal of real-time visualization and assist clinicians in the real-time acquisition and evaluation of the svOCT images. However, the GC segmentation presented in this chapter had limitations. For example, it only worked on volumes that do not contain frequent large motions artifacts, and it only worked well on healthy retinal layers. The 2D GC segmentation using the NPP library

could only successfully segment the ILM and BM at the current stage. A 3D GC segmentation would improve the segmentation results as the low-contrast layers would have more reinforcing information from adjacent B-scans.

In conclusion, this chapter has demonstrated that the GPU-based GC segmentation is a more effective solution over the naïve user-selected segmentation to visualize specific vascular beds as it better handled patient motion artifacts and curvature of the retina (for example, from cysts or other deformations).

Chapter 7.

Discussion/Future Works

7.1. Conclusion

In conclusion, this thesis has presented a GPU accelerated svOCT system to visualize retinal blood flow in real-time. The results have been also validated in a comparison study with FA. The svOCT was demonstrated to be a useful and important imaging tool to study the retinal capillary networks. Using svOCT, there are a number of ongoing studies that are being performed in collaboration with physicians and vision researchers. Lastly, a GPU accelerated Graph Cut segmentation was implemented and integrated with the svOCT GPU program to enhance the visualization of capillary networks in real-time, allow the segmentation process to be performed in real-time, and make the svOCT imaging system more adaptable in clinical usage.

The svOCT system and its processing power provide us with a lot of potential to study the retina and to investigate retinal diseases. However, there are still many challenges that need to be resolved. One of the challenges is motion artifacts. The acquisition time for the svOCT volume is limited by both the number of transverse scans acquired and the A-scan acquisition speed. Acquiring a larger number of samples is desirable in svOCT to improve the resolution; however, increasing the number of samples increases the acquisition time, which increases the chances of motion artifacts. Motion artifacts significantly degrade the quality of the svOCT image, and also increase the imaging time required for the patient, as repeated volumes need to be acquired until suitable data are obtained. All of the volunteers that participated in the studies described in Chapter 5 were selected based on their fixation ability. Depending on the number of

regions of interest required, it could take more than an hour per eye to acquire a complete dataset, with time allowed in between for the subject to rest.

Our current imaging acquisition utilized a scanning pattern of 3 B-scans at each lateral location, which is the minimum number required to produce enough statistics to properly calculate the variance of the intensity changes. Acquiring fewer than three B-scans per BM scan introduces more background noise in the svOCT image, whereas increasing the number of B-scans per BM scan will result in an improvement to the contrast (signal noise ratio). As mentioned above, increasing the number of B-scans requires more acquisition time. Adding an extra frame (a total of 4) to each BM scan increases the acquisition time by a factor of 1/3, making the data acquisition substantially more sensitive to patient motion, but only incrementally improving the results of the svOCT processing. Therefore, with the tradeoff between better contrast and more motion artifacts, 3 B-scans per BM scan is the best compromise for our current system.

In order to improve the image quality, the next step is to implement techniques to minimize the motion artifacts. Two ongoing projects in our lab are: (1) Integrating a fixation target and eye tracking device onto the sample arm; and (2) Double-buffer the light source to speed up the A-scan rate by a factor of two. These improvements will greatly aid us in acquiring svOCT data from elderly patients that have difficulties to stay still. Future work could also introduce real time motion tracking, as is becoming increasingly common in commercial OCT systems [86,87].

7.2. Future work

The flow contrast imaging using speckle variance OCT demonstrated in this thesis holds great potential in scientific and clinical application. Some possible directions to advance the svOCT technology are listed below.

7.2.1. Double buffered system

The current SSOCT human retinal imaging system at ECC has an A-scan rate of 100 kHz. The volumetric imaging rate is dependent on the number of A-scans within the

volume. For our current volume size, which consists of 300x300x3 A-scans, it takes ~3.15 seconds to acquire a volume. The volumetric acquisition time can be reduced by decreasing the volume size; however, this ultimately decreases the spatial resolution. Thus, it is preferable to increase the A-scan rate. Since our current laser source operates at a duty cycle of approximately 50%, the A-scan rate can be increased by implementing a double-buffered configuration [88–90]. The general idea is to split the light source into two channels, delay one channel using a long spool of optical fiber and then recombine the two channels to produce a single channel that has double the A-scan rate. This configuration would double the speed of our current SSOCT imaging system and enable fast scanning. In our current imaging system, the time interval is ~3ms between each B-scan. Braaf, Boy, et al. reported that a time interval ≥ 2.50 ms is optimal for visualizing the *en-face* flow images of the retina in the macular area for a $\sim 2 \times 2$ mm² area [87]. Also, the *en-face* flow image is reasonably good with a time interval of ~1.25 ms. Therefore, with double buffering, we can still achieve well defined blood flow information using half of the original acquisition time with the same sample size (1024x300x300x3). With the benefit of fast acquisition speed, we can increase the number of A-scans in each B-scan as well as the number of BM scans in each volume to improve the svOCT image resolution. Also, by increasing the number of B-scans acquired for each BM scan we can increase the signal-noise-ratio of the svOCT images.

7.2.2. Customized GC segmentation utilizing multiple GPUs

In Chapter 6 a GPU implementation of retinal layer segmentation for svOCT was presented that utilized a pre-developed Graph Cut (GC) solver for 2D images provided by the NPP library. The results are very promising but this work is only preliminary. The NPP library GC solver method is not optimized. Based on the performance report generated by the GPU profiler, as shown in Figure 7.1, there is a lot of idle time as highlighted by the arrows. The total idle time is approximately half of the overall processing time for the GC solver. This function is packaged and source code is not available, so the reasons causing these idle times remain unknown. An area of future work is to optimize the GC procedure on GPU.

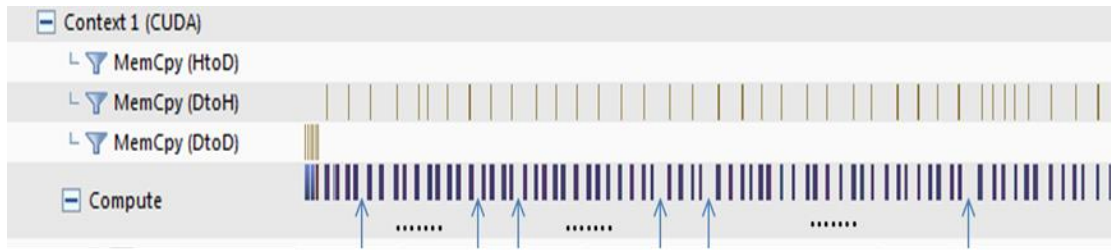


Figure 7.1. A timeline of GC solver from NPP.

Another issue with the pre-developed GC solver was that it is only efficient to detect ILM and BM layers. The NPP GC solver used a region-based segmentation algorithm that only identified the strongest edges within each region. While this approach was sufficient to segment the ILM and BM layer, which have the highest intensity, it was inadequate in localizing layers with lower contrast, such as the IPL and OPL. Also, the GC solver performs adequately to segment the entire retina in healthy subjects; however, the performance has a higher chance of failure for retinas with diseases such as macular holes or edema. Therefore, a better segmentation approach is needed to identify more layers, and to improve the segmentation result for retinas that have various morphological changes due to disease.

The implementation of a customized GC algorithm is needed in order to (1) increase the segmentation rate by reducing the idle times; and (2) improve the segmentation performance on diseased retinas. The current segmentation implementation consumes a lot of GPU power; therefore, utilizing multiple GPUs to segment the volume in parallel is the next goal to achieve real-time visualization. This is an open research question left for future work, with significant potential applications as high speed and real-time OCT becomes more wide spread.

7.2.3. Quantitative analysis of svOCT and Fluorescence Angiography

The clinical work presented in this thesis represents important stepping stones to study the retinal capillary networks in the human eye. The retinal capillary networks are critically linked to neuronal health and disease, and the ability of svOCT to perform *in vivo* examination of these retinal capillary networks is valuable for studying mechanisms that govern retinal homeostasis and retinal vascular diseases. The capability of svOCT

with respect to qualitatively visualizing various capillary networks has been compared with FA in my thesis. A follow up study that can be investigated in the future is to quantitatively analyze the vascular network information such as capillary density in the fovea avascular zone of the retina using both svOCT and FA, and evaluate the performance of each technique in many patients with a large variance in age and health conditions. This comparative study will be vital for determining whether svOCT is a suitable technique for clinical diagnostics of vascular related pathologies on a regular basis.

References

- 1 Vision | Define Vision at Dictionary.com.
<http://dictionary.reference.com/browse/vision> (accessed 10 Aug2014).
- 2 CNIB - Fast Facts about Vision Loss. <http://www.cnib.ca/en/about/media/vision-loss/Pages/default.aspx> (accessed 10 Aug2014).
- 3 Polyak SL. *The retina*. Chicago: : University of Chicago 1941.
- 4 Simple Anatomy of the Retina by Helga Kolb – Webvision.
<http://webvision.med.utah.edu/book/part-i-foundations/simple-anatomy-of-the-retina/> (accessed 10 Aug2014).
- 5 The retinal ganglion cell layer. By J. M. Van Buren, A.B., M.D., M.Sc., Ph.D. 9¾ x 6¾ in. Pp. 143 + ix. Illustrated. 1963. Springfield, Ill.: Charles C. Thomas. \$10.75.
Br J Surg 1964;**51**:399–399. doi:10.1002/bjs.1800510553
- 6 Webvision. <http://webvision.med.utah.edu/> (accessed 20 Aug2014).
- 7 Curcio CA, Sloan KR, Kalina RE, *et al*. Human photoreceptor topography. *J Comp Neurol* 1990;**292**:497–523. doi:10.1002/cne.902920402
- 8 Zhang HR. Scanning electron-microscopic study of corrosion casts on retinal and choroidal angioarchitecture in man and animals. *Prog Retin Eye Res* 1994;**13**:243–70. doi:10.1016/1350-9462(94)90012-4
- 9 Yu PK, Balaratnasingam C, Cringle SJ, *et al*. Microstructure and network organization of the microvasculature in the human macula. *Investig Ophthalmol Vis Sci* 2010;**51**:6735–43. doi:10.1167/iovs.10-5415
- 10 Huang D, Swanson E, Lin C, *et al*. *Optical Coherence Tomography*. Berlin, Heidelberg: : Springer Berlin Heidelberg 2008. doi:10.1007/978-3-540-77550-8
- 11 Drexler W, Morgner U, Kärtner FX, *et al*. In vivo ultrahigh-resolution optical coherence tomography. *Opt Lett* 1999;**24**:1221. doi:10.1364/OL.24.001221
- 12 Drexler W, Fujimoto JG. State-of-the-art retinal optical coherence tomography. *Prog Retin Eye Res* 2008;**27**:45–88. doi:10.1016/j.preteyeres.2007.07.005

- 13 Fujimoto JG. Optical coherence tomography for ultrahigh resolution in vivo imaging. *Nat Biotechnol* 2003;**21**:1361–7. doi:10.1038/nbt892
- 14 Yannuzzi LA, Rohrer KT, Tindel LJ, *et al.* Fluorescein angiography complication survey. *Ophthalmology* 1986;**93**:611–7.<http://www.ncbi.nlm.nih.gov/pubmed/3523356> (accessed 20 Aug2014).
- 15 Bai Y, Zhu Y, Chen Q, *et al.* Validation of glaucoma-like features in the rat episcleral vein cauterization model. *Chin Med J (Engl)* 2014;**127**:359–64.<http://www.ncbi.nlm.nih.gov/pubmed/24438629> (accessed 20 Aug2014).
- 16 Gao, J., Sandhu, N., Samad, I., Xu, J., Sarunic, M. V., Cao, S., Cui, J., To, E., Matsubara JA. Pro-inflammatory Events in a Rhodopsin Transgenic Rat Model of Retinal Degeneration. *Submitted*
- 17 Frost S, Kanagasingam Y, Sohrabi H, *et al.* Retinal vascular biomarkers for early detection and monitoring of Alzheimer’s disease. *Transl Psychiatry* 2013;**3**:e233. doi:10.1038/tp.2012.150
- 18 Xu J, Wong K, Jian Y, *et al.* Real-time acquisition and display of flow contrast using speckle variance optical coherence tomography in a graphics processing unit. *J Biomed Opt* 2014;**19**:026001. doi:10.1117/1.JBO.19.2.026001
- 19 Xu, J., Han, Sherry., Balaratnasingam, C., Mammo, Z., Wong, K., Lee, S., Cua, M., Young, M., Kirker, A., Albiani, D., Forooghian, F., Mackenzie, P., Merkur, A., Yu, D. Y., Sarunic M V. Retinal angiography with real-time speckle variance optical coherence tomography. *Submitted*
- 20 Chan, G., Balaratnasingam, C., Xu, J., Mammo, Z., Han, Sherry., Mackenzie, P., Merkur, A., Kirker, A., Albiani, D., Sarunic, M. V., Yu DY. Validating the utility of speckle variance optical coherence tomography for quantitatively analysing human perifoveal capillary networks. *Submitted*
- 21 Tan. P., Balaratnasingam, C., Xu, J., Mammo, Z., Han, Sherry., Mackenzie, P., Merkur, A., Kirker, A., Albiani, D., Sarunic, M. V., Yu DY. Quantitative Comparison of Retinal Capillary Images Derived By Speckle Variance Optical Coherence Tomography with Histology. *Submitted*
- 22 Yu, P., Balaratnasingam, C., Xu, J., Morgan, W. H., Mammo, Z., Han, Sherry., Mackenzie, P., Merkur, A., Kirker, A., Albiani, D., Sarunic, M. V., Yu DY. Label-free density measurements of radial peripapillary capillaries in the human retina. *Submitted*
- 23 Mammo, Z., Balaratnasingam, C., Xu, J. *et al.* Evaluating the Utility of Speckle-Variance Optical Coherence Tomography (svOCT) for Assessing the Human Foveal Avascular Zone. *Prep*

- 24 Fercher AF, Hitzenberger CK, Kamp G, *et al.* Measurement of intraocular distances by backscattering spectral interferometry. *Opt Commun* 1995;**117**:43–8. doi:10.1016/0030-4018(95)00119-S
- 25 Choma M, Sarunic M, Yang C, *et al.* Sensitivity advantage of swept source and Fourier domain optical coherence tomography. *Opt Express* 2003;**11**:2183–9.
- 26 Leitgeb R, Hitzenberger C, Fercher A. Performance of fourier domain vs time domain optical coherence tomography. *Opt Express* 2003;**11**:889. doi:10.1364/OE.11.000889
- 27 De Boer JF, Cense B, Park BH, *et al.* Improved signal-to-noise ratio in spectral-domain compared with time-domain optical coherence tomography. *Opt Lett* 2003;**28**:2067–9.
- 28 Snodderly DM, Weinhaus RS, Choi JC. Neural-vascular relationships in central retina of macaque monkeys (*Macaca fascicularis*). *J Neurosci* 1992;**12**:1169–93. <http://www.ncbi.nlm.nih.gov/pubmed/1556592> (accessed 10 Aug2014).
- 29 Chan A, Duker JS, Schuman JS, *et al.* Stage 0 macular holes: observations by optical coherence tomography. *Ophthalmology* 2004;**111**:2027–32. doi:10.1016/j.ophtha.2004.05.034
- 30 Altaweel M, Ip M. Macular hole: improved understanding of pathogenesis, staging, and management based on optical coherence tomography. Published Online First: 2 July 2009. <http://informahealthcare.com/doi/abs/10.1076/soph.18.2.58.15858> (accessed 20 Aug2014).
- 31 Hee MR, Baumal CR, Puliafito CA, *et al.* Optical Coherence Tomography of Age-related Macular Degeneration and Choroidal Neovascularization. *Ophthalmology* 1996;**103**:1260–70. doi:10.1016/S0161-6420(96)30512-5
- 32 Thomas D, Duguid G. Optical coherence tomography--a review of the principles and contemporary uses in retinal investigation. *Eye (Lond)* 2004;**18**:561–70. doi:10.1038/sj.eye.6700729
- 33 Lee S, Fallah N, Forooghian F, *et al.* Comparative Analysis of Repeatability of Manual and Automated Choroidal Thickness Measurements in Non-Neovascular Age-Related Macular Degeneration. *Invest Ophthalmol Vis Sci* Published Online First: March 2013. doi:10.1167/iovs.12-11521
- 34 Young M. Volumetric in-vivo Medical Imaging of the Optic Nerve Head to Investigate Susceptibility by Mei Young Thesis Submitted in Partial Fulfillment of The Requirements for The Degree in the School of Engineering Science. 2009.

- 35 Young M. High-speed Volumetric in vivo Medical Imaging for Morphometric Analysis of The Human Optic Nerve Head by Thesis Submitted In Partical Fulfillment Of The Requirements For The Degree of Master of Applied Science In the School of Engineering Science Faculty. 2011.
- 36 Morrison JC, Cepurna WO, Johnson EC. Modeling glaucomatous optic nerve damage. *Int Ophthalmol Clin* 1999;**39**:29–41. http://www.ncbi.nlm.nih.gov/entrez/query.fcgi?cmd=Retrieve&db=PubMed&dopt=Citation&list_uids=10709572
- 37 Wojtkowski M, Srinivasan VJ, Ko TH, *et al.* Ultrahigh-resolution, high-speed, Fourier domain optical coherence tomography and methods for dispersion compensation. *Opt Express* 2004;**12**:2404. doi:10.1364/OPEX.12.002404
- 38 Bai Y, Dergham P, Nedev H, *et al.* Chronic and acute models of retinal neurodegeneration TrkA activity are neuroprotective whereas p75NTR activity is neurotoxic through a paracrine mechanism. *J Biol Chem* 2010;**285**:39392–400. doi:10.1074/jbc.M110.147801
- 39 Bai Y, Xu J, Brahimi F, *et al.* An agonistic TrkB mAb causes sustained TrkB activation, delays RGC death, and protects the retinal structure in optic nerve axotomy and in glaucoma. *Invest Ophthalmol Vis Sci* 2010;**51**:4722–31. doi:10.1167/iovs.09-5032
- 40 Lee DC, Xu J, Sarunic M V, *et al.* Fourier domain optical coherence tomography as a noninvasive means for in vivo detection of retinal degeneration in *Xenopus laevis* tadpoles. *Invest Ophthalmol Vis Sci* 2010;**51**:1066–70. <http://www.iovs.org/cgi/content/abstract/51/2/1066>
- 41 Xu J, Molday LL, Molday RS, *et al.* In Vivo Imaging of the Mouse Model of X-Linked Juvenile Retinoschisis with Fourier Domain Optical Coherence Tomography. *Invest Ophthalmol Vis Sci* 2009;**50**:2989–93. doi:10.1167/iovs.08-2542
- 42 Sarunic M V., Yazdanpanah A, Gibson E, *et al.* Longitudinal study of retinal degeneration in a rat using spectral domain optical coherence tomography. *Opt Express* 2010;**18**:23435. doi:10.1364/OE.18.023435
- 43 Quigley HA. Optic Nerve Damage in Human Glaucoma. *Arch Ophthalmol* 1982;**100**:135. doi:10.1001/archoph.1982.01030030137016
- 44 Nakazawa T, Nakazawa C, Matsubara A, *et al.* Tumor necrosis factor-alpha mediates oligodendrocyte death and delayed retinal ganglion cell loss in a mouse model of glaucoma. *J Neurosci* 2006;**26**:12633–41. doi:10.1523/JNEUROSCI.2801-06.2006

- 45 Chen S, Wang L, Zhang X. Neuroprotection in glaucoma: present and future. *Chin Med J (Engl)* 2013;**126**:1567–77.<http://www.ncbi.nlm.nih.gov/pubmed/23595396> (accessed 20 Aug2014).
- 46 Tao YK, Kennedy KM, Izatt JA. Velocity-resolved 3D retinal microvessel imaging using single-pass flow imaging spectral domain optical coherence tomography. *Opt Express* 2009;**17**:4177–88.http://www.pubmedcentral.nih.gov/articlerender.fcgi?artid=2723161&tool=pmc_entrez&rendertype=abstract (accessed 20 Aug2014).
- 47 Leitgeb RA, Schmetterer L, Hitzenberger CK, *et al.* Real-time measurement of in vitro flow by Fourier-domain color Doppler optical coherence tomography. *Opt Lett* 2004;**29**:171. doi:10.1364/OL.29.000171
- 48 White B, Pierce M, Nassif N, *et al.* In vivo dynamic human retinal blood flow imaging using ultra-high-speed spectral domain optical coherence tomography. *Opt Express* 2003;**11**:3490. doi:10.1364/OE.11.003490
- 49 Wang RK, Jacques SL, Ma Z, *et al.* Three dimensional optical angiography. *Opt Express* 2007;**15**:4083–97.<http://www.ncbi.nlm.nih.gov/pubmed/21273541>
- 50 Wang RK, An L. Multifunctional imaging of human retina and choroid with 1050-nm spectral domain optical coherence tomography at 92-kHz line scan rate. *J Biomed Opt* 2011;**16**:050503. doi:10.1117/1.3582159
- 51 An L, Shen TT, Wang RK. Using ultrahigh sensitive optical microangiography to achieve comprehensive depth resolved microvasculature mapping for human retina. *J Biomed Opt* 2011;**16**:106013. doi:10.1117/1.3642638
- 52 An L, Subhush HM, Wilson DJ, *et al.* High-resolution wide-field imaging of retinal and choroidal blood perfusion with optical microangiography. *J Biomed Opt*; **15**:026011. doi:10.1117/1.3369811
- 53 Fingler J, Schwartz D, Yang CH, *et al.* Mobility and transverse flow visualization using phase variance contrast with spectral domain optical coherence tomography. *Opt Express* 2007;**15**:12636–53.
- 54 Fingler J, Readhead C, Schwartz DM, *et al.* Phase-contrast OCT imaging of transverse flows in the mouse retina and choroid. *Invest Ophthalmol Vis Sci* 2008;**49**:5055–9. doi:10.1167/iovs.07-1627
- 55 Fingler J, Zawadzki RJ, Werner JS, *et al.* Volumetric microvascular imaging of human retina using optical coherence tomography with a novel motion contrast technique. *Opt Express* 2009;**17**:22190.<http://www.opticsexpress.org/abstract.cfm?URI=oe-17-24-22190> (accessed 30 Aug2012).

- 56 Jia Y, Tan O, Tokayer J, *et al.* Split-spectrum amplitude-decorrelation angiography with optical coherence tomography. *Opt Express* 2012;**20**:4710–25. doi:10.1364/OE.20.004710
- 57 Mariampillai A, Leung MKK, Jarvi M, *et al.* Optimized speckle variance OCT imaging of microvasculature. *Opt Lett* 2010;**35**:1257–9.
- 58 Mahmud MS, Cadotte DW, Vuong B, *et al.* Review of speckle and phase variance optical coherence tomography to visualize microvascular networks. *J Biomed Opt* 2013;**18**:50901. doi:10.1117/1.JBO.18.5.050901
- 59 Poole KM, Tucker-Schwartz JM, Sit WW, *et al.* Quantitative optical imaging of vascular response in vivo in a model of peripheral arterial disease. *Am J Physiol Heart Circ Physiol* 2013;**305**:H1168–80. doi:10.1152/ajpheart.00362.2013
- 60 Melissa C . Skala , Yuankai K . Tao AM. D and JA. I. Functional optical coherence tomography in preclinical models. In: *Handbook of Biomedical Optics*. 2011. 281–302.
- 61 Izatt JA, Kulkarni MD, Yazdanfar S, *et al.* In vivo bidirectional color Doppler flow imaging of picoliter blood volumes using optical coherence tomography. *Opt Lett* 1997;**22**:1439. doi:10.1364/OL.22.001439
- 62 Yazdanfar S. In Vivo Imaging of Human Retinal Flow Dynamics by Color Doppler Optical Coherence Tomography. *Arch Ophthalmol* 2003;**121**:235. doi:10.1001/archophth.121.2.235
- 63 Izatt JA, Kulkarni MD, Kobayashi K, *et al.* OPTICAL COHERENCE TOMOGRAPHY FOR BIODIAGNOSTICS. *Opt Photonics News* 1997;**8**:41. doi:10.1364/OPN.8.5.000041
- 64 Lee KKC, Mariampillai A, Yu JXZ, *et al.* Real-time speckle variance swept-source optical coherence tomography using a graphics processing unit. *Biomed Opt Express* 2012;**3**:1557–64. doi:10.1364/BOE.3.001557
- 65 Sylwestrzak, M., Szlag, D., Szkulmowski, M., Gorczynska, I., Bukowska, D., Wojtkowski, M., and Targowski P. Four-dimensional structural and Doppler optical coherence tomography imaging on graphics processing units and Doppler optical coher-. *J Biomed Opt* doi:10.1117/1.JBO.17.10.100502
- 66 Xu J, Wong K, Jian Y, *et al.* GPU Open Source Code with svOCT Implementation. 2013.<http://borg.ensc.sfu.ca/research/svoct-gpu-code.html>
- 67 Jian Y, Wong K, Sarunic M V. Graphics processing unit accelerated optical coherence tomography processing at megahertz axial scan rate and high resolution video rate volumetric rendering. *J Biomed Opt* 2013;**18**:26002. doi:10.1117/1.JBO.18.2.026002

- 68 Guizar-Sicairos M, Thurman ST, Fienup JR. Efficient subpixel image registration algorithms. *Opt Lett* 2008;**33**:156. doi:10.1364/OL.33.000156
- 69 Hendargo HC, Estrada R, Chiu SJ, *et al.* Automated non-rigid registration and mosaicing for robust imaging of distinct retinal capillary beds using speckle variance optical coherence tomography. *Biomed Opt Express* 2013;**4**:803–21. doi:10.1364/BOE.4.000803
- 70 Conroy L, DaCosta RS, Vitkin IA. Quantifying tissue microvasculature with speckle variance optical coherence tomography. *Opt Lett* 2012;**37**:3180–2.
- 71 Mendis KR, Balaratnasingam C, Yu P, *et al.* Correlation of histologic and clinical images to determine the diagnostic value of fluorescein angiography for studying retinal capillary detail. *Invest Ophthalmol Vis Sci* 2010;**51**:5864–9. doi:10.1167/iovs.10-5333
- 72 Tan PEZ, Yu PK, Balaratnasingam C, *et al.* Quantitative Confocal Imaging of the Retinal Microvasculature in the Human Retina. *Invest. Ophthalmol. Vis. Sci.* 2012;**53**:5728–36. doi:10.1167/iovs.12-10017
- 73 Chan G, Balaratnasingam C, Yu PK, *et al.* Quantitative Morphometry of Perifoveal Capillary Networks in the Human Retina. *Invest. Ophthalmol. Vis. Sci.* 2012;**53**:5502–14. doi:10.1167/iovs.12-10265
- 74 Yu D-Y, Cringle SJ. Oxygen distribution in the mouse retina. *Invest Ophthalmol Vis Sci* 2006;**47**:1109–12. doi:10.1167/iovs.05-1118
- 75 Cringle SJ, Yu PK, Su E-N, *et al.* Oxygen distribution and consumption in the developing rat retina. *Invest Ophthalmol Vis Sci* 2006;**47**:4072–6. doi:10.1167/iovs.05-1638
- 76 Yu DY, Cringle SJ. Retinal degeneration and local oxygen metabolism. *Exp. Eye Res.* 2005;**80**:745–51. doi:10.1016/j.exer.2005.01.018
- 77 Ames A, Li YY, Heher EC, *et al.* Energy metabolism of rabbit retina as related to function: high cost of Na⁺ transport. *J Neurosci* 1992;**12**:840–53.
- 78 Tan PEZ, Yu PK, Balaratnasingam C, *et al.* Quantitative confocal imaging of the retinal microvasculature in the human retina. *Invest Ophthalmol Vis Sci* 2012;**53**:5728–36. doi:10.1167/iovs.12-10017
- 79 Yu PKK, Balaratnasingam C, Morgan WHH, *et al.* The structural relationship between the microvasculature, neurons, and glia in the human retina. *Invest Ophthalmol Vis Sci* 2010;**51**:447–58. doi:10.1167/iovs.09-3978

- 80 Yu PK, Tan PEZ, Morgan WH, *et al.* Age-Related Changes in Venous Endothelial Phenotype at Human Retinal Artery-Vein Crossing Points. *Invest. Ophthalmol. Vis. Sci.* 2012;**53**:1108–16. doi:10.1167/iovs.11-8865
- 81 Li K, Wu X, Chen DZ, *et al.* Optimal surface segmentation in volumetric images--a graph-theoretic approach. *IEEE Trans Pattern Anal Mach Intell* 2006;**28**:119–34. doi:10.1109/TPAMI.2006.19
- 82 Wong VPK. *GPU Acceleration of Volume Segmentation for Retinal Thickness*. 2013.
- 83 Goldberg A V. An Efficient Implementation of a Scaling Minimum-Cost Flow Algorithm. *J Algorithms* 1997;**22**:1–29. doi:10.1006/jagm.1995.0805
- 84 Goldberg A V., Tarjan RE. A new approach to the maximum-flow problem. *J. ACM.* 1988;**35**:921–40. doi:10.1145/48014.61051
- 85 Younes L. *Mathematical Image Analysis*.
- 86 Vienola K V, Braaf B, Sheehy CK, *et al.* Real-time eye motion compensation for OCT imaging with tracking SLO. *Biomed Opt Express* 2012;**3**:2950–63. doi:10.1364/BOE.3.002950
- 87 Braaf B, Vienola K V, Sheehy CK, *et al.* Real-time eye motion correction in phase-resolved OCT angiography with tracking SLO. *Biomed Opt Express* 2013;**4**:51–65. doi:10.1364/BOE.4.000051
- 88 Huber R, Adler DC, Fujimoto JG. Buffered Fourier domain mode locking: Unidirectional swept laser sources for optical coherence tomography imaging at 370,000 lines/s. *Opt Lett* 2006;**31**:2975–7. doi:10.1364/OL.31.002975
- 89 Dhalla A-H, Shia K, Izatt JA. Efficient sweep buffering in swept source optical coherence tomography using a fast optical switch. *Biomed. Opt. Express.* 2012;**3**:3054. doi:10.1364/BOE.3.003054
- 90 Potsaid B, Baumann B, Huang D, *et al.* Ultrahigh speed 1050nm swept source / Fourier domain OCT retinal and anterior segment imaging at 100,000 to 400,000 axial scans per second. *Opt Express* 2010;**18**:20029. doi:10.1364/OE.18.020029